Multi-functional flat optics for imaging and sensing

by

Fan Yang

B.S., Peking University (2019)

Submitted to the Materials Science and Engineering
in partial fulfillment of the requirements for the degree of

Doctor of Philosophy in Materials Science and Engineering

at the

MASSACHUSETTS INSTITUTE OF TECHNOLOGY

September 2023

Author .....
Materials Science and Engineering
August 18, 2023

Certified by .....
Juejun Hu
Professor
Thesis Supervisor

Accepted by .....
Robert J. Macfarlane
Chairman, Department Committee on Graduate Studies

Multi-functional flat optics for imaging and sensing

by

Fan Yang

Submitted to the Materials Science and Engineering
on August 18, 2023, in partial fulfillment of the
requirements for the degree of
Doctor of Philosophy in Materials Science and Engineering

Abstract

Flat optics refer to optical devices composed of ultra-thin and light-weight planar optical components, which manipulate light in ways that are not possible using conventional bulky optics. Multiple applications including imaging, beam steering, sensing, and projection can be performed through a single layer flat lens, which facilitates the integration between optical and electronic components. Through the arbitrary manipulation of wavefront, flat optics feature improved optical performance and customized functionality.

In this thesis, we focus on the design and optimization of single or multi-layer metasurfaces to construct flat optical components for imaging and sensing applications. We propose a variety of device configurations, analytical analysis, material choices, and prove the effectiveness of the concepts through experimental demonstrations.

We have developed the design concept of wide field-of-view metalens for imaging applications. We proposed the analytical solution to obtain the optimum phase profile of the single layer wide field-of-view metalens, which show diffraction-limited imaging performance with near-180° field-of-view. We further built up the algorithm to design metalens with combined wide field-of-view and achromatic features, which show 1 - 1.2 μm wavelength broad bandwidth imaging performance with minimal transverse focal shift.

We have demonstrated a variety of depth sensing techniques using metasurfaces. They include passive depth sensing mechanism using stereo camera, and active depth sensing mechanism through structured light projection and beam steering. Near-180° 3-D depth sensing have been realized utilizing the wide field-of-view design concept.

We have further combined multiple optical properties into a single flat optical element through polarization-multiplexing. Based on the proposed concept, we demonstrated another passive 3-D depth sensing mechanism through utilization of metalens with double-helix point-spread-function. The metalens showed meter scale depth sensing range with sub-millimeter accuracy. We have further proposed the design concept of wide field-of-view metalens with extended depth-of-focus. Opposite to metalens for depth sensing, it reveals object information in the entire 3 - 10 mm

extended depth range in the near-180° field-of-view through image deconvolution. We have also proposed a zoom lens with tunable magnification through polarization-multiplexing. An unprecedented 10x zoom ratio between the wide-angle and telephoto mode has been experimentally validated.

Lastly, we have realized the reconfiguration in the mid-infrared band using phase change materials. We demonstrated zoom lens in the 5.2 μm wavelength leveraging the large refractive index difference of the phase change material $Ge_2Se_2Sb_4Te_1$ between the amorphous and crystalline states. A similar 10x zoom ratio between the two modes has been validated. We have further showed the design concept of a varifocal lens. The focal length can be tuned continuously between 4 - 10 mm range by controlling the temperature profile of the metasurface.

Thesis Supervisor: Juejun Hu
Title: Professor

Acknowledgments

I am deeply grateful to the MIT for providing an exceptional academic environment that has enriched my learning and research experience in countless ways. From the cutting-edge facilities and resources to the world-class faculty and staff, MIT has set the highest standards of excellence in education and scholarship. I have been fortunate to be part of a community that fosters intellectual curiosity, rigorous inquiry, and interdisciplinary collaboration.

I owe a debt of gratitude to my thesis advisor, Professor Juejun (JJ) Hu, for his unwavering guidance, expertise, and inspiration throughout my graduate studies. As the leader of the photonic materials (PMAT) group, he has been at the forefront of research in the field, and I have been fortunate to be part of his team. His insights, feedback, and encouragement have been invaluable in shaping the direction and quality of my thesis work. I am also grateful for his mentorship and the opportunities he has provided me to grow as a researcher. His dedication to excellence, creativity, and collaboration has been a constant source of motivation for me, and I am proud to have him as my advisor.

I would like to extend my heartfelt thanks to Dr. Tian Gu, who has been an indispensable mentor throughout my research projects. His deep knowledge, technical skills, and passion for scientific discovery have been instrumental in advancing our team's goals and achievements. His patient guidance, constructive feedback, and generous support have been invaluable in shaping my research ideas and experiments. I have learned a great deal from his dedication to precision, efficiency, and innovation, and I am honored to have worked with him. His commitment to excellence and integrity has set a high standard for me, and I will carry his lessons and inspiration with me in my future endeavors. I am deeply grateful for his mentorship and friendship.

I would like to express my gratitude to my thesis committee members, Professor Rafael Jaramillo and Professor Lionel C. Kimerling, for their invaluable guidance, insights, and feedback throughout the development of my thesis projects. Their extensive expertise, diverse perspectives, and critical thinking have greatly enhanced

the rigor and relevance of my research, and I am indebted to them for their time and effort. I appreciate the thoughtful discussions we had during the committee meetings, which challenged me to think deeply and broadly about my research questions and methods. I am also grateful for the constructive feedback and suggestions they provided me, which helped me to refine my ideas. Their mentorship has been instrumental in shaping my intellectual growth and professional identity.

I would like to extend my sincere thanks to my groupmate, Dr. Mikhail Shalaginov, for his invaluable guidance, collaboration, and mentorship during my early stage of the graduate career. His expertise in optical design and measurement has been essential in shaping my research projects and enhancing my technical skills. He has generously shared his knowledge, resources, and time to help me understand the intricacies of the field and the challenges of the experiments. His patient guidance and feedback have been instrumental in improving the quality and impact of my research, and I am grateful for his support. His dedication to innovation, teamwork, and excellence has been an inspiration to me, and I am honored to have worked with him. I hope to continue to learn from him and collaborate with him in the future.

I would like to express my deep appreciation to my groupmate, Dr. Hung-I Lin, for his invaluable contribution to the fabrication of the metasurface samples that were critical to all of my research projects. His technical skills, attention to detail, and commitment to quality have been essential in ensuring the success and reproducibility of our experiments. He has devoted countless hours to designing, optimizing, and executing the fabrication processes, and has shared his knowledge and expertise with me generously. His collaborative spirit, patience, and dedication have made a significant impact on the progress and outcomes of my research, and I am grateful for his help. His commitment to excellence and teamwork has set a high standard for me, and I am honored to have worked with him.

I would like to express my heartfelt appreciation to my previous groupmates, Dr. Shaoliang Yu, Dr. Ying Pan, Dr. Yifei Zhang, Dr. Qingyang Du, and Dr. Sensong An for their invaluable help, guidance, and friendship during the early stage of my graduate career. They have been wonderful mentors, collaborators, and friends, who

have supported me both professionally and personally. Their expertise, knowledge, and feedback have greatly contributed to the development and success of my research projects. They have generously shared their time, resources, and ideas with me, and have helped me overcome challenges and difficulties. In addition, they have provided me with a supportive and welcoming community, where I could learn, grow, and thrive as a graduate student. I am deeply grateful for their mentorship, guidance, and friendship, and I cherish the memories and experiences we shared together. I wish them all the best in their future endeavors.

I would like to express my sincere appreciation to my groupmates, Dr. Akira Ueno, Dr. Louis Martin, Luigi Ranno, and Khoi P. Dao, for their invaluable contribution to the progress and quality of my research projects. They have been great collaborators, advisors, and friends, who have supported me with their expertise, ideas, and feedback. Their diverse backgrounds, skills, and perspectives have enriched my research and helped me to tackle complex problems from different angles. They have also provided me with a stimulating and friendly work environment, where I could learn, share, and grow as a researcher. I am grateful for the fruitful discussions, and brainstorming sessions we had together, which have helped me to improve my research and communication skills. Their commitment to excellence, creativity, and collegiality has inspired me to strive for the best and to enjoy the process. I am honored to be a part of this team.

I would like to extend my gratitude to all my other groupmates, Tushar S. Karnik, Cosmin C. Popescu, Brian Mills, Maarten Peters, Dr. Diana Mojahed, and Dr. Brian Sia, for their support, encouragement, and camaraderie during my time in the group. Their diverse backgrounds, interests, and experiences have brought different perspectives and expertise to the group, and have made our meetings and social events lively and enjoyable. Their positive attitudes, sense of humor, and team spirit have made the group a fun and welcoming place to be. I am grateful for the friendships and memories we have created together, and I wish them all the best in their future endeavors.

I would like to express my appreciation to Sarah Ciriello for her administrative

support in our group, including help with placing orders, scheduling meetings, and organizing events. Her efficiency, professionalism, and friendliness have greatly facilitated the smooth operation of our lab and have made our work easier and more enjoyable.

I would like to thank the collaborators from other institutions who have contributed to my research projects. Their expertise, resources, and collaborations have been crucial to the success of my research, and I am grateful for their support and guidance. Their willingness to share their knowledge and experience has expanded my research horizons and enriched my scientific understanding. I am honored to have had the opportunity to work with such talented and generous collaborators, and I look forward to continuing to collaborate with them in the future.

I would like to express my heartfelt thanks to my dear friends for their unwavering support and companionship throughout my graduate studies. Their encouragement and understanding have helped me to navigate the challenges and uncertainties of research and personal life. They have celebrated my successes, encouraged me during setbacks, and cheered me up when I felt down. Their kindness, humor, and positivity have made my life richer, happier, and more meaningful. I am grateful for their friendship and for the memories we have created together. I could not have made it this far without their help and encouragement, and I look forward to staying in touch with them and to creating new adventures together.

I would like to express my deep gratitude to my parents for their unconditional love and support throughout my graduate studies. They have been my unwavering pillars of strength, their constant encouragement and guidance have given me the courage, confidence, and perseverance to pursue my dreams and overcome challenges. They support me remotely even when I was far away from home. I am blessed to have such wonderful parents, and I am grateful for everything they have done for me. I hope to make them proud and to repay their kindness in my own way.

Contents

List of Figures

List of Tables

Chapter 1

Introduction

1.1 Multi-functional planar metasurfaces: opportunities and challenges

Multi-functional planar metasurfaces are a type of artificial nanostructured optical element that can manipulate light and other electromagnetic waves with unprecedented control and precision. These metasurfaces are composed of an array of subwavelength-sized structures, often made of metals or dielectrics, that are designed to exhibit unusual optical properties not found in naturally occurring materials. By carefully tailoring the geometry, size, and spacing of these structures, the wavefront of light can be modified at will, and therefore a variety of functions can be performed leveraging different design concepts.

The key advantage of metasurfaces is their ability to perform multiple optical functions in a single planar layer. Conventional refractive optical elements such as lenses rely on the bulk material properties to manipulate the wavefront of light through propagation, which inevitably adds up system size, weight, and cost. On the other side, metasurfaces feature sub-wavelength abrupt wavefront modulation through the tailoring of single layer nanostructures, which therefore dramatically reduces the complexity of the optical devices. Further more, conventional optics require the stacking of optical elements along the optical axis, where each of them serves different optical

purpose. The serial configuration not only takes up device space, but also suffers from misalignment and integration issues due to the existence of curved surfaces. Metasurfaces circumvent these issues through the multiplex of functions into single or a few planar layers, which makes them fabrication and integration compatible with the photonic and electronic devices.

Metasurfaces have gain increasing traction in recent years, and have been widely applied in a variety of techniques spanning over imaging[3–6], display[7–10], sensing[11–14], telecommunication[15–18], energy harvesting[19–22], optical computing[23–26], etc. While the rapid growth of metasurface technology, it is confronted with a few challenges listed in the following that need to be dealt with to become comparable and eventually outperform its counterparts in a few critical research areas.

- Seidel aberrations. Similar to refractive lenses, metalenses also suffer from angle-dependent monochromatic Seidel aberrations including coma, astigmatism, and field curvature. Special configurations are required to correct these aberrations for wide field-of-view (WFOV) imaging.

- Meta-atom dispersion and chromatic aberrations. Chromatic aberration of the conventional refractive lens comes from the dispersion of the material, where the refractive index changes as wavelength, and therefore modifies the phase accumulated through propagation. The major chromatic aberration origination of the metasurface, on the other side, comes from the phase wrap and fixed Fresnel zone position. Achromatic metalens design typically involves dispersion engineering of the meta-atoms to satisfy required phase profile at different wavelengths.

- Scaling effect. Accurate simulation of metasurface performance involves full-wave simulation of the entire metasurface area composed of millions of sub-wavelength nanostructures, which can be time consuming or even impossible at current stage when scaled to millimeter size. Therefore, special algorithms need to be developed to optimize the phase profile of the metasurface for different applications.

Besides these challenges, metasurfaces also foresee novel functions that are difficult to be realized through conventional optical elements, which are listed in the following.

- Point-spread-function (PSF) engineering. Through the optimization of the shape and distribution of meta-atoms, arbitrary wavefront control can be realized to modulate the PSF of the system, and integrate the 3-D information of the object into the 2-D image.

- Reconfiguration. The optical property of the metasurface can be actively tuned through a variety of mechanisms, and therefore exhibits more than one optical properties in different conditions.

The thesis aims to solve the existing challenges while propose design concepts and demonstrate realization of novel functions of the flat optics technology for imaging and sensing applications.

1.2 Metalens for wide field-of-view imaging

Field-of-view (FOV) is an essential metric for gauging the performance of optical systems. In an imaging instrument, having a WFOV allows capturing the surrounding scene in a single frame without image stitching or mechanical scanning. Therefore, WFOV imaging optics are extensively applied in photography, microscopy, biomedical diagnosis, navigation and control, 3-D sensing, security surveillance and beyond. Optical reciprocity stipulates that WFOV systems can also be used for light or image projection, a much sought-after feature enabling wide-angle beam steering and immersive displays for augmented/virtual reality (AR/VR) devices, automotive sensors, gaming simulators, and movie theaters.

Traditional WFOV optics used in these applications are based on refractive lenses. As the angle of incidence (AOI) of light with respect to optical axis increases, the angle-dependent monochromatic Seidel aberrations are exacerbated on top of on-axis spherical aberration. To suppress these aberrations, the conventional solution involves

distributing the light bending power over multiple refractive surfaces in stacked compound lenses, which however comes at the expense of system size, weight, cost, and complexity.

Optical metasurfaces present an alternative approach to implement WFOV optical systems with significant Size, Weight, Power and Cost (SWaP-C) advantages. They have been proven to effectively suppress the AOI-dependent Seidel aberrations, thereby facilitating WFOV operation. A variety of WFOV metalens design concepts have been proposed. One scheme involves stacking multiple metasurfaces, and diffraction-limited FOVs up to 56° have been attained using this method [27–32]. Combining a single-layer metasurface or diffractive lens with a physical or virtual optical aperture provides an architecturally simpler approach [33–44]. In particular, a single-element fisheye metalens was demonstrated with $> 170°$ diffraction-limited FOV [1]. This unprecedented performance was accomplished through iterative numerical optimization of the metasurface optical phase profile, a computationally intensive process precluding extensive exploration of the full design parameter space while also yielding little insight into the fundamental design trade-offs.

In this thesis, we derive an analytical solution to the optimum phase profile of a WFOV flat lens assuming the single-layer geometry, yielding results in excellent agreement with numerically optimized designs but without requiring computationally intensive optimization. The analytical solution is generically applicable to different operation wavelength ranges, lens/substrate materials, and meta-atom or diffractive element designs. We further derive an expression relating design parameters with focusing performance and investigate the design trade-offs in realizing WFOV flat lenses.

As a proof of concept, we experimentally demonstrate the WFOV flat lens architecture that achieves 140° FOV in the long-wave infrered (LWIR) band with 10.6 μm wavelength. The large metasurface was fabricated through the photolithography and deep reactive ion etching (DRIE) on a monolithic float zone Si wafer. We further characterize the focusing quality of the WFOV metasurfaces and demonstrate thermal imaging at ambient temperature through the utilization of a LWIR focal plane

array. The design concept is generically applicable to other wavelengths, materials, and configuration parameters.

We further expand the operational bandwidth of the WFOV metalens through the optimization of metalens comprising free-form meta-atoms using direct search (DS) algorithm. By combining the DS algorithm with a deep neural network trained for free-form meta-atom generation, we demonstrate that the diverse dispersion behaviors of the free-form meta-atoms lead to superior performance of the metalenses compared to their diffractive counterparts. We further implement the technique to design an achromatic fisheye metalens with 200 nm spectral bandwidth in the near-IR and a WFOV close to 180°.

Finally, we show that the front aperture of the WFOV metalens structure can be replaced with a second metasurface, and various functionalities can be combined with the WFOV feature. Following this concept, we replace the front aperture with a metasurface containing a cubic phase to capture the image with extended depth-of-focus (EDOF). The EDOF WFOV metalens doublet shows near-180° FOV imaging in the depth range of 3 - 10 mm.

1.3 Passive and active techniques for 3-D depth sensing

Conventional optical imaging systems map 3-D scene to a flat image plane at the cost of losing depth information. The missing knowledge of object distances, however, is crucial to a variety of applications spanning autonomous driving, object recognition, gesture control, virtual/augmented reality, etc. Multiple passive and active depth sensing mechanisms have been utilized to retrieve 3-D information.

Beam steering and pattern/image projection rank among the most promising implementations of active depth sensing. Beam steering is an essential function in scanning light detection and ranging (LiDAR) systems[45–52], whereas pattern projection optics are widely deployed in 3-D depth sensing modules based on structured

light[12, 53–57] and can be applied to novel near-eye projection displays as well[7, 58–64]. Compared to conventional refractive and diffractive optics, metasurfaces promise simpler optical architectures with reduced element count[1, 65, 66], enhanced performance (e.g., efficiency, resolution, etc.) especially at large angles[67–71], and low cost at scale taking advantage of wafer-level manufacturing and integration[72–74]. Furthermore, since these applications use discrete-wavelength or narrow-band sources such as vertical cavity surface emitting lasers (VCSELs) or light emitting diodes (LEDs), they largely avoid the complications associated with chromatic aberrations inherent of metasurfaces, thereby allowing early implementations of this technology.

In this thesis, we derive an analytical framework to rationally guide the design of metasurface projection optics. We show that, for projection optics comprising a single-layer metasurface, the optimum design adopts a quadratic phase profile in the limit of small beam divergence. The singlet design, however, suffers from increasing distortion especially at large FOVs, which compromises meridional angular resolution [70] and further poses a challenge for applications such as projection display. We then mathematically prove that projection optics based on metasurface doublets furnish the capability of on-demand distortion compensation. Following this derivation, we further propose an optimum metasurface doublet configuration to correct projected image distortion, and quantify the trade-off between distortion and aberration of the projected beams.

Active depth sensing techniques require active illumination and modulation components, which add to system complexity, cost and power consumption. To solve these issues, various passive depth sensing techniques have been proposed, which measure the object distance without emitting any active light source. One way to achieve passive depth sensing is through the use of stereo camera, which involves using two cameras to capture images of the same scene from different viewpoints. By comparing the differences in the images captured by each camera, the system can calculate the depth information of the scene.

In this thesis, we demonstrate WFOV 3-D depth sensing through the integration of two identical WFOV metalenses to construct the stereoscopic camera prototype,

which achieves depth mapping with an unprecedented FOV of 170°.

1.4 Multi-functional reconfigurable metasurfaces

The metasurface design concepts discussed so far have fixed optical property. On the other side, reconfigurable optics with dynamically tunable optical properties to meet diverse application demands at will, has been a long-sought goal for optical engineers. Conventional reconfigurable optics rely on mechanical moving parts to tune the optical distance between multiple lens components or between the lens and image plane, this however increases system size, weight, complexity, and cost. Metasurfaces provide an alternative solution with higher resolution, cost effective fabrication and integration, and increased degree-of-freedom (DoF) compared to their refractive counterparts.

Reconfigurable metasurfaces through mechanical deformation or displacement have been widely explored[75–81], which however suffer similar drawbacks faced by the mechanical reconfigurable refractive lenses.

A variety of non-mechanical reconfigurable metasurfaces have been demonstrated recently. The tunability can be achieved through electro-optics[49, 82–84], thermal optics[85–88], and all-optical effects[89–91]. However, due to the weak coupling between electrical, thermal, and optical properties, the tunable index range is usually below 1.0, which restricts the phase coverage of meta-atoms in different states, and limits the tuning range of the active device. Also, most of the approaches are volatile, which requires continuous power supply, and significantly adds up the power consumption of the device.

In this thesis, we propose two different reconfiguration mechanism that are both able to provide independent phase profile control of the individual meta-atoms in two states. The first approach is through the utilization of polarization-multiplexing, where the shape of the meta-atom is engineered so that it has different phase delay response in the two orthogonal polarization states.

We first apply the design concept to another passive depth sensing mechanism named point-spread-function (PSF) engineering. The stereo camera passive depth

sensing technique mentioned in the last section is limited by the well-known trade-off between system size and depth resolution. To solve this issue, an alternative route of depth-from-defocus (DFD) has been proposed, which applies computational imaging techniques to infer the depth from defocus blur of a classical lens[92–99]. However, defocus cue is often ambiguous and requires complementary information such as pictorial depth cues to determine the depth. They also have low depth estimation accuracy since a defocused point-spread-function (PSF) of a classical lens varies slowly along the optical axis. In addition, the DFD method further suffers from limited depth range and degraded lateral resolution. To solve these issues, PSF engineering has been explored to enhance depth discrimination capability. This approach employs custom tailored phase masks to define PSF of the system, and depth information can be encoded into the captured image directly. PSFs designed for depth estimation include astigmatic PSF[100], biplane PSF[101], tetrapod-like PSF[102–104], etc. Among them, double-helix (DH) PSF[105–110] generates two rotating foci, where the rotation angle determines the object depth. This method streamlines image data post-processing given its shape simplicity. To produce the phase mask for DH PSF generation, the classical approach involves a spatial light modulator (SLM) placed in the Fourier plane of a 4f system, which however creates alignment challenges and significantly increases footprint of the entire system. Metasurfaces provide a compact and cost-effective alternative to the 4f system. A monocular DH metasurface was experimentally realized by Jin *et al*[111]. The image captured by the DH metasurface is the convolution of the scene with the DH PSF, and thus the depth information can only be estimated with prior knowledge of the original object. Colburn *et al* coupled a DH metasurface with an extended depth-of-focus (EDOF) metasurface in a binocular setting to resolve this ambiguity[112]. Multiplexing presents a way to combine the two metasurfaces into one aperture to realize monocular depth estimation (MDE)[113]. Along this line, MDE was recently demonstrated with a decoupled pair of conjugate single-helix PSFs[114]

In this thesis, we demonstrate a polarization-multiplexed DH metasurface design for MDE using a single metasurface. Two DH PSFs with opposite rotating directions

are each encoded with a linear polarization. Importantly, the focal point rotation angles of the two PSFs always add up to 90°, a feature that allows computationally efficient and unambiguous reconstruction of both the depth and image. As one specific example, we experimentally implemented the design at 635 nm wavelength within the depth range of 45-212 mm and rotation angles of up to 80°.

Apart from PSF engineering, reconfigurable metasurfaces also show their application in zoom lens design. Zoom lenses with adjustable effective focal length (EFL) and magnification ratio are widely employed in applications spanning photography, cinematography, computer vision, biomedical imaging, microscopy, image projection, and beyond. Traditionally, optical zoom is realized by switching between multiple lens groups, each with a fixed zoom (e.g., in most phone cameras); or using stacked lenses where one or more of the lens elements move along the optical axis [115–117]. Both approaches, however, come at the cost of size, weight, complexity, cost and sometimes image quality. Lenses made of liquids or elastomers have also been introduced to achieve zoom via shape deformation [118–122], although concerns over reliability, controllability, optical quality, and scalability still loom. While a number of 'zoom metalens' designs have been proposed [123–127], they are in fact varifocal lenses[128–144] whose focal plane constantly shifts as the lens configuration changes. A true zoom metalens must be parfocal; in other words, the position of its focal plane must remain stationary when its EFL is changed. A parfocal zoom metalens design was first theoretically conceptualized by Zheng *et al.* [145, 146]. However, the design only affords a small zoom ratio. Moreover, no parfocal zoom metalens has been experimentally demonstrated to our knowledge.

In this thesis, we propose a non-mechanical parfocal polarization-multiplexing zoom metalens design in the visible using waveguide-type meta-atoms. The design can switch between 40° (the 'wide-angle' mode) and 4° (the 'telephoto' mode) field-of-view (FOV) with 10x optical zoom. It offers minimal distortion, and aberration-free optical quality.

Apart from polarization-multiplexing, we also propose another reconfiguration mechanism by using phase change materials (PCMs). They are a type of material

that can undergo reversible phase transitions between a crystalline phase and an amorphous phase upon exposure to external stimuli such as heat, light, or electric field. The optical properties of PCMs, in particular their refractive index and absorption, can be significantly modified during the phase transition, making them attractive for various applications in optics and photonics. By incorporating PCMs into metasurfaces, their optical properties can be dynamically controlled and tuned, enabling a wide range of applications such as beam steering, wavefront shaping, holography, and sensing.

Following the similar design concept of the polarization-multiplexing zoom lens, we further demonstrate a zoom metalens in the mid-infrared in the form of a reconfigurable Huygens' surface made of PCMs.

Finally, we prove that the reconfigurable metasurfaces are not restricted to only two optical states through the design of a continuously tunable varifocal metalens using PCMs without complex structure for individual meta-atom tuning. Single layer concentric ring-shaped doped silicon heaters are deposited beneath the metalens, electrodes are connected to each heater to control the desired temperature gradient, which partially crystallize PCM to obtain the target wavefront control. We further build up a customized computationally efficient optimization algorithm to control the voltage of electrodes, and characterize the metalens focusing performance across the entire designed focal length range. As a proof of concept, we designed a millimeter scale reconfigurable metalens that works in the near infrared with continuous tunable focal length in the range of $4 - 10\ mm$.

Chapter 2

Metasurfaces concept

2.1 Configuration and working principle of metasurfaces

Metasurfaces are composed of 2-D sub-wavelength nanostuctures on a thin substrate. The phase, amplitude, and polarization of light can be manipulated through the engineering of geometry, size, and arrangement of these structures. They have emerged as a promising technology for a wide range of applications, including imaging, sensing, communication, and energy harvesting, due to their unique ability to control light at the nanoscale.

The thesis focuses on dielectric metasurfaces, which utilize the unique properties of high refractive index materials to achieve unprecedented control over the phase, amplitude, and polarization of light. When light impinges on the nanostructures, it generates electric and magnetic dipole moments inside the resonator, and the scattering properties can be tuned by manipulating size, shape, and refractive index of the resonators. They offer lower losses and higher transmission efficiency compared to the metallic metasurfaces.

Metasurfaces for imaging applications typically have size from a few hundred micrometers to even centimeters. Therefore, even though metasurfaces provide large degree-of-freedom through the arbitrary manipulation of the resonators, the full-wave

simulation and characterization of the entire metasurface are difficult to implement with the state-of-the-art computational system. To reduce the computational load, the design principle of metasurfaces is typically divided into two sequential steps. The first one involves dividing the entire metasurfaces into square grid - unit cell with a fixed period of Λ. The nanostructure within each unit cell is called meta-atom, the transmittance and phase delay of the cell can be simulated assuming periodic condition at the boundaries. The transmittance and phase response of the entire metasurface can be regarded as the stitching of the individual meta-atoms. Therefore, by generating a library which maps the optical response of the meta-atoms to their shapes, the wavefront of the metasurface can be modulated locally at sub-wavelength scale. The design principle of meta-atoms is discussed in detail in Chapter 2.2. The second step involves the optimization of the metasurface phase profile. Depending on the specific application, the phase profile can be expressed in the forms listed below:

- Analytical expression. In this case, the phase profile can be whether well-known expressions like hyperbolic, quadratic, cubit phase, etc., or be derived through analytical analysis.

- Polynomial terms. In most cases, it is difficult or impossible to express the phase profile as a simple equation. However, it can be approximated as the sum of polynomial terms. A few numerical approaches can be performed to optimize the corresponding polynomial coefficients.

- Discrete phase profile. The previous situations assume the phase profile of the metasurface to be 'continuous', and can be expressed in the form of equations. On the other side, to further leverage the full DoF metasurface can provide, discrete phase profile can be utilized, where the phase difference between neighboring meta-atoms can be as large as π. In this case, phase of each meta-atom can be optimized individually.

We address the optimization of the metasurface phase profile in Chapters 2.3 - 2.4. The final metasurface design therefore involves mapping of the meta-atom library to the optimized phase profile.

Finally, it should be noted that the proposed design concept assumes periodic boundary condition between meta-atoms, which only applies when the coupling effect between neighboring periods is weak. The local phase of the meta-atom would thus deviate from the assumption with large meta-atom filling factor or diffraction angle where strong coupling effect exists. Special design approaches can be performed to take these effects into account, which we will discuss briefly in Chapter 7.

2.2 Meta-atom structure and design concept

Fig. 2-1a shows an example meta-atom structure with cylindrical amorphous silicon (a-Si) meta-atom sitting on the fused silica substrate. Finite-difference time-domain (FDTD) or rigorous coupled-wave analysis (RCWA) algorithms can be utilized to simulate the amplitude/transmittance and phase delay response of the meta-atom using periodic boundary conditions. Assuming the incident wavelength of 780 nm, meta-atom period of 300 nm, and meta-atom thickness of 485 nm, the simulated transmittance and phase delay response using RCWA algorithm as a function of diameter are shown in Figs. 2-1b-c.

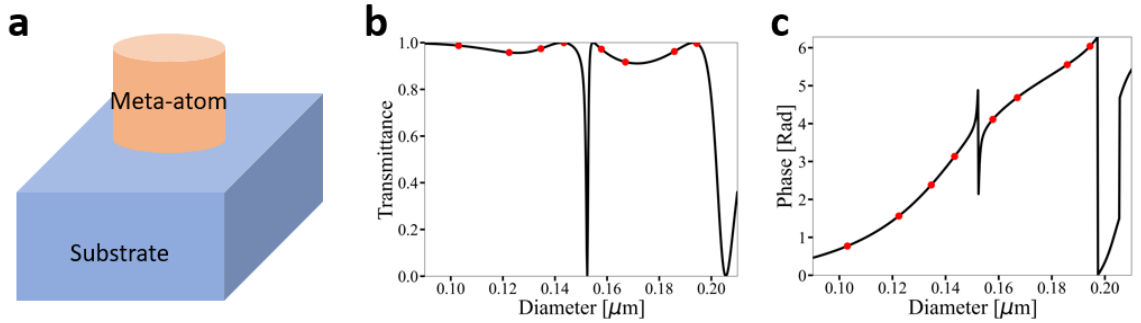

Figure 2-1: Meta-atom structure and optical response. (a) Schematic illustration of cylindrical meta-atom structure. (b) Transmittance and (c) phase delay response of the meta-atom as a function of diameter

Generally, the phase of the meta-atom increases with diameter, as single meta-atom can be considered as waveguide, and the effective refractive index increases with diameter. However, the plots also feature a few resonant positions where transmittance drops well below unity with large phase delay variation in a narrow range

depending on the specific wavelength, meta-atom dimensions and index. These resonance positions should be circumvented in the meta-atom selection process as they have low transmittance and also are sensitive to fabrication error. To fulfill the arbitrary wavefront control requirement, the period and thickness of the meta-atom should be optimized to follow the general criteria of near-unity transmittance and entire 0 - 2π phase coverage.

The final step of the meta-atom design involves the generation of the meta-atom library, where a group of eight meta-atoms with different diameters and high transmittance is selected that covers the 2π phase range with $\frac{\pi}{4}$ spacing. The following figure-of-merit (FOM) can be utilized to select the meta-atoms from the design pool[65]:

$$FOM = T \cdot \left(\frac{sin(2|\phi_{meta} - \phi_{target}|)}{2|\phi_{meta} - \phi_{target}|} \right)^2 \tag{2.1}$$

where T and ϕ_{atom} are the transmittance and phase delay of the meta-atom, ϕ_{target} is the target phase profile. The eight selected meta-atoms following the criteria are denoted with the red dots shown in Figs. 2-1b-c.

Cylindrical meta-atoms are the most frequently used structure due to their fabrication tolerance and polarization independence. However, other complex structures have also been proposed to fulfill special requirements such as broad bandwidth operation, high efficiency of large incident angle, etc., and we will address these issues in the following chapters.

2.3 Metasurface phase profile optimization through ray tracing technique

Ray tracing is the straight forward way to optimize the phase profile of the metasurface. In this case, the phase profile is approximated to be the sum of the polynomial terms assuming the azimuthal symmetry:

$$\phi(r) \approx \sum_{i=1}^{N} A_i \cdot r^{2i} \tag{2.2}$$

Here, $\phi(r)$ is the phase profile of the metasurface, r is the radial distance to the center of the metasurface, A_i are the polynomial coefficients, N is the maximum polynomial term. The optimization process is thus simplifies to the optimization of the N polynomial coefficients.

The optical response of the metasurface can be simulated using ray tracing technique through commercial softwares. In ray tracing, light is represented as a collection of rays, which are imaginary lines that indicate the path of light. These rays are traced as they propagate through the metasurface, obeying the laws of reflection and refraction pending on its local phase gradient obtained through the polynomial expression. The polynomial terms are then optimized through the defined FOM that depends on specific applications.

Since the ray tracing technique dramatically reduces the DoF of the metasurface system to around 10 polynomial terms, the optimization process can be very fast and typically completes in less than 1 minute. However, it features the following problems and thus can only be applied under certain conditions.

- Continuous phase profile. The approximation of the phase profile to the polynomial terms requires the phase different between neighboring meta-atoms to be small and the phase gradient is also continuous. Therefore, it can not be applied to scenarios which require large DoF as we will see later.

- Azimuthal symmetry. The expression of the polynomial terms along the radial coordinate also requires azimuthal symmetry, therefore, it can not be applied to PSF egineering, hologram, etc.

- Local maximum. The optimization may be trapped in the local maximum. Therefore, physical insight should be applied to set up the initial conditions.

- Inaccuracy of ray tracing technique. Ray tracing treats light as a collection of rays, neglecting the wave nature of light. These wave effects become more sig-

nificant in situations involving small-scale features or interactions with complex optical structures.

2.4 Metasurface phase profile optimization through direct search algorithm

To solve the potential issues raised by the ray tracing technique, we use direct search (DS) algorithm to optimize the metasurface when it has discrete phase profile.

DS algorithm optimizes phase and amplitude profiles on metasurface by controlling distribution of meta-atoms to obtain target functionalities. The flow chart of the DS algorithm is shown in Fig. 2-2. It optimizes a pre-defined FOM that characterizes performance of the optical system.

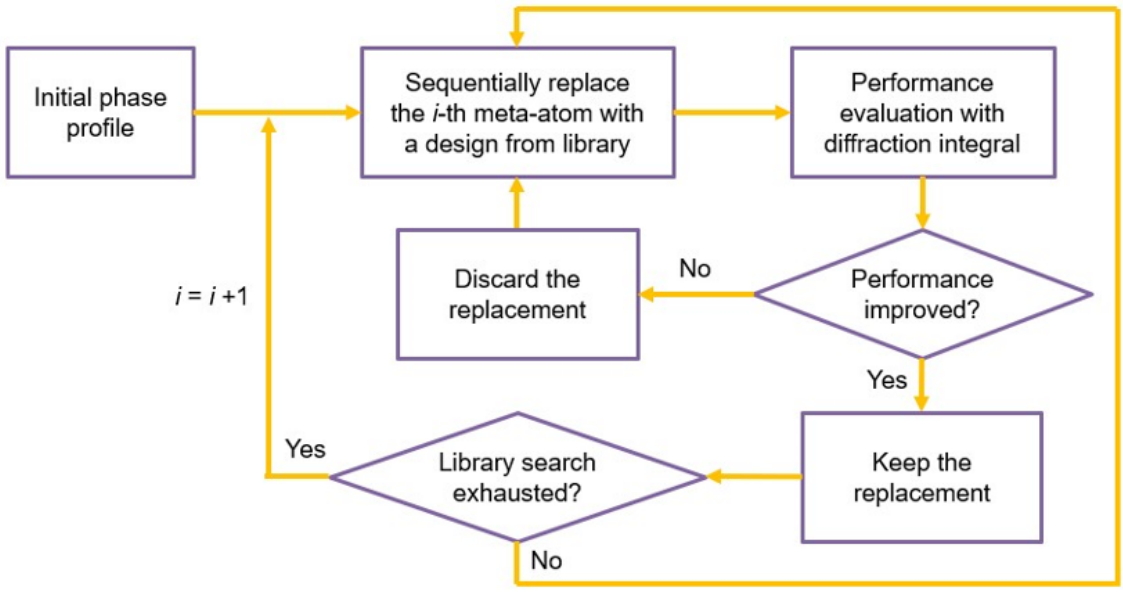

Figure 2-2: Flow chart of DS algorithm.

The FOM is usually defined as:

$$FOM = \sum_i I_i - \kappa \cdot S^2\{I_i\} \tag{2.3}$$

where I is the intensity of the focal spot at certain positions, i corresponds to different conditions, it can be wavelength, incident angle, object distance, etc., which is application dependent. $S^2\{I_i\}$ is the variance of the sampled intensities, and a negative sign is assigned to limit the variance of the metalens performance across different conditions. κ is an empirical coefficient which is set to seek a balance between the average performance across different conditions and the variance among them.

The DS optimization starts with generating a random initial phase mask of metalens. The algorithm then traverses all meta-atom positions, replacing the meta-atom with a different meta-atom structures from the library each time and computing the FOM using the Kirchhoff diffraction integral, which we will discuss in the next section. The meta-atom design with the largest FOM is selected before moving on to the next meta-atom position on the metasurface. The process proceeds till the entire metasurface is traversed.

Compared to the optimization of polynomial terms, DS algorithm offers orders of magnitude larger DoF, and involves individual meta-atom tuning. The computational load, however, is usually larger since it has to iterate the entire metasurface a few times. Parallel and cloud computation can be utilized to reduce the computation time, and millimeter scale metasurface optimization can be performed in less than one hour.

DS algorithm is also not a global optimum solver, and therefore the outcome depends on the initial guess of the phase profile. However, it is empirically found that in most cases the dependence on the initial condition is weak, and they all converge to the similar optimized FOM after a few iterations. The algorithm has been utilized in a few applications in the thesis, and will be discussed in detail in the following chapters.

2.5 Metasurface imaging performance characterization

The accurate simulation of the metasurface imaging performance requires the full-wave simulation. However, this is difficult to implement on millimeter scale metasurfaces using current technology due to the excessive computation load. Ray tracing provides an alternative approach to estimate the performance of the optical system, however, it faces the problems as discussed in the last section. Also, it can not be applied to metasurfaces with discrete phase profiles.

Kirchhoff diffraction integral can be utilized to evaluate the performance of the metasurface, which reduces computational load compared to the full-wave simulation, and also is more accurate than ray-tracing techniques since it takes into account the diffraction effect. The configuration is depicted in Fig. 2-3. The diffraction integral is expressed as:

$$\widetilde{U}(P) = \frac{-i}{\lambda} \cdot \Lambda^2 \sum_N \frac{1}{2}(cos\theta_0 + cos\theta)\ \widetilde{U_0}(Q) \cdot \frac{1}{r} \cdot e^{ikr} \tag{2.4}$$

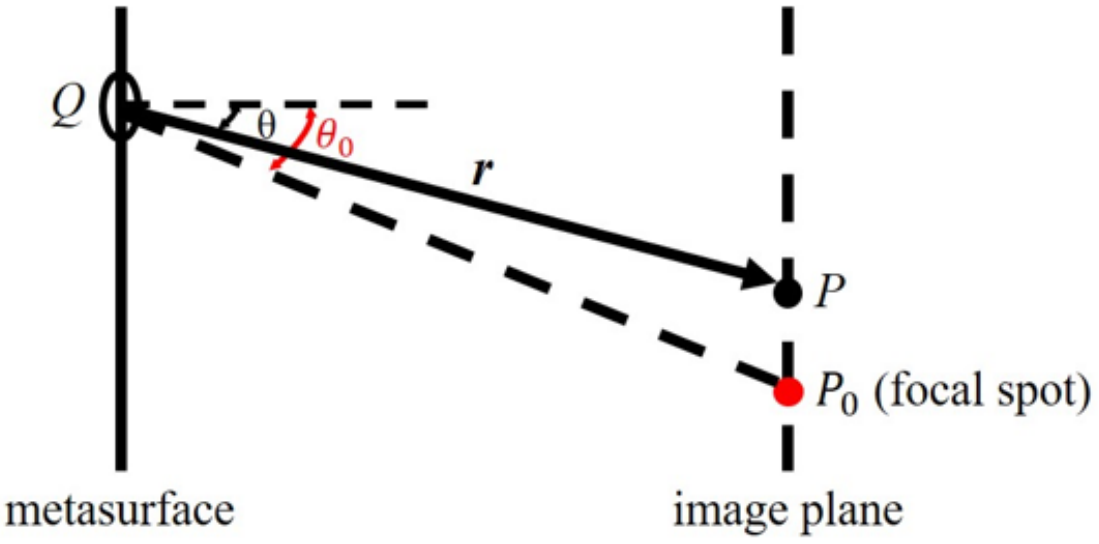

Figure 2-3: Illustration of Kirchhoff diffraction integral method.

Here λ is the wavelength, Λ is the pitch of meta-atoms, $\widetilde{U_0}(Q)$ is the complex amplitude incident on the metasurface, and $\widetilde{U}(P)$ is the complex amplitude on the image plane. Since most of the incident waves converge near the focal spot, the first angular term θ_0 in the integration, which is the direction of outlet wave, is taken as the angle between surface normal and focal spot direction as an approximation.

A few parameters can be used to characterize the metasurface focusing quality, they include full-width-at-half-maximum (FWHM) and Strehl ratio of the focal spot, its point-spread-function (PSF) and modulation transfer function (MTF), and also the bulk and focusing efficiency of the metalens. In the following we discuss these parameters in detail.

FWHM is a measure of the width of the central region of the focal spot where the intensity is at least half of the maximum intensity. It is defined as the distance between two points on the intensity distribution curve where the intensity is half of the maximum. It is used to characterize the size of the focal spot.

Strehl ratio is calculated by comparing the peak intensity of the actual focal spot produced by an optical system with the peak intensity that would be obtained in an ideal diffraction-limited system under the same conditions. In reality, since it is impossible to obtain the focal spot intensity profile across the entire infinitely large image plane from the measurement, Strehl ratio can be calculated by normalizing the intensity of the actual and ideal focal spots within the 3 - 5 times FWHM. It provides a measure of how well the optical system approaches the theoretical ideal performance. The optical system is regarded as diffraction-limited if Strehl ratio is larger than 0.8.

PSF is a fundamental concept in optics and imaging that characterizes the response of an optical system to a point source of light. It describes how a point source is spread or blurred in the image formed by the system. MTF is a measure of the ability of an optical system to transfer or reproduce contrast in an image. It is defined as the ratio of the modulation of the image produced by the system to the modulation of the original object. It is typically measured as a function of spatial frequency. Two different approaches can be utilized to estimate the MTF of the optical system. The

first one uses the object with different frequencies and sharp edges that has white to black transition, and the MTF can be calculated by the definition from the captured image of the optical system. Alternatively, it can also be calculated as the Fourier transform of the PSF, which is more efficient in the simulation. It quantifies the system's ability to preserve spatial details or high-frequency components of an object when imaged.

Bulk efficiency of the metasurface is defined as the power that transmit through the metasurface divided by the total incident power. It can be approximated as the average transmittance of all the meta-atoms. Focusing efficiency is defined as the power near the focal spot (typically 3 - 5 FWHM area) divided by the total incident power, and therefore is smaller than the bulk efficiency. It characterizes the fraction of the power that enters the focal spot area. Therefore, the bulk efficiency minus the focusing efficiency characterizes the power that contributes to the background noise. In the actual measurement, however, it is difficult to get the accurate power near the focal spot. In this case, a pinhole with around 50 - 200 μm diameter can be placed near the focal spot to block the stray light, the power goes through the pinhole can be regarded as an estimation of the focusing power.

These parameters are utilized to characterize the metalens performance in the following chapters.

2.6 Flat optics applications

Flat optics have gained significant attention in recent years due to their unique capabilities of wavefront control. A few notable applications are listed in the following:

- Imaging and microscopy. Metasurfaces offer new possibilities for high-resolution imaging and microscopy. By controlling the phase and polarization of light, metasurfaces can shape the wavefront and enable aberration correction, extending the depth of field, and improving image quality. They can also be used to create flat lenses, enabling the miniaturization of optical systems.

- Optical polarization control. Metasurfaces can efficiently manipulate the polarization of light at subwavelength scales. They find applications in polarization optics, including polarizers, waveplates, and beam splitters. Metasurface-based polarizers are compact, thin, and lightweight alternatives to traditional polarizing elements, offering improved performance and integration capabilities.

- Holography and 3-D displays. Metasurfaces enable the generation of complex wavefronts required for holography and 3D displays. By controlling the phase and amplitude of light, metasurfaces can shape the wavefronts to create realistic and immersive 3D visualizations without the need for bulky optical elements.

- Light manipulation and beam steering. Metasurfaces provide precise control over the direction and shape of light beams. They can deflect, focus, or shape light with high efficiency and flexibility. This capability is useful in applications such as optical communications, LiDAR systems, and laser beam steering.

- Optical sensing and spectroscopy. Metasurfaces enable the development of highly sensitive optical sensors and spectroscopic devices. They can enhance light-matter interactions, leading to improved sensitivity and selectivity in sensing applications. Metasurface-based sensors can be integrated with microfluidics, enabling lab-on-a-chip systems for biological and chemical analysis.

- Nonlinear optics. Metasurfaces can enhance and control nonlinear optical processes, where light interacts with materials to generate new frequencies or modulate its properties. By engineering the metasurface design, nonlinear effects can be tailored for applications in frequency conversion, ultrafast optics, and nonlinear imaging.

- Light trapping and solar energy harvesting. Metasurfaces can enhance light absorption and trapping in photovoltaic devices. They can be designed to selectively absorb specific wavelengths or angles of incident light, improving the efficiency of solar cells and enabling new strategies for light management in energy-harvesting systems.

- Stealth technology and cloaking. Metasurfaces have been explored for their potential in creating invisibility cloaks and stealth technologies. By manipulating the properties of incident light, metasurfaces can redirect and conceal the presence of objects, making them invisible or difficult to detect by certain wavelengths or sensors.

In the following chapters, we will discuss the imaging and sensing applications of the metasurfaces, and focus on features including WFOV, broad bandwidth, 3-D depth sensing, and also active tunability.

Chapter 3

Wide field-of-view metalens

3.1 Overview of wide field-of-view metalens

The canonical metalens design assumes a hyperbolic phase profile to convert an incident plane wave to a spherical wavefront. The phase profile is given by[147]:

$$\phi_0 = -\frac{2\pi}{\lambda}\left(\sqrt{f^2 + x^2 + y^2} - f\right) \tag{3.1}$$

where x and y are the coordinates of meta-atoms, and f is the metalens focal length. The design eliminates spherical aberration at normal incidence. When a beam arrives at a metasurface at an oblique incident angle (θ_x,θ_y), the desired phase distribution becomes:

$$\phi_{\theta_x,\theta_y} = -\frac{2\pi}{\lambda} \cdot \left[\sqrt{f^2 + (x - x_0)^2 + (y - y_0)^2} - \sqrt{f^2 + x_0^2 + y_0^2} + (xsin\theta_x + ysin\theta_y)\right] \tag{3.2}$$

where $x_0 = ftan\theta_x$ and $y_0 = ftan\theta_y$ are the coordinates of the focal spot on the image plane. The difference between the two phase profiles is responsible for other third order (Seidel) aberrations including coma, astigmatism, and field curvature, all of which are dependent on the AOI.

Various design strategies have been proposed to mitigate these aberrations and

thereby expand the FOV of metalenses.

The sensitivity to off-axis aberration can be alleviated by resorting to a phase distribution that is invariant with respect to incident angle change. A quadratic phase function assuming the following form fulfills this requirement:

$$\phi(r) = -\frac{\pi}{\lambda} \cdot \frac{r^2}{f} \tag{3.3}$$

where r, λ and f represent the radial position from the lens center, free-space wavelength, and effective focal length, respectively. For an oblique incident beam at $AOI = \theta$ within in the x-z plane (where z denotes the optical axis), a linear phase gradient term $(2\pi/\lambda) \cdot sin\theta$ added, yielding the following phase distribution after it exits the metasurface:

$$\phi(r) = -\frac{\pi}{\lambda} \cdot \frac{r^2}{f} - \frac{2\pi}{\lambda} x sin\theta = -\frac{\pi}{\lambda f}\left[(x + f sin\theta)^2 + y^2\right] + \frac{\pi f sin^2\theta}{\lambda} \tag{3.4}$$

Eq. 3.4 indicates that the phase profile can be regarded as the same parabolic function as Eq. 3.3 (neglecting the constant phase term) but laterally shifted along the x-axis for a distance of $-f sin\theta$. Therefore, focusing properties are preserved for oblique incident beams.

The quadratic phase concept was first proposed by Pu *et al.*[41] and later on also numerically investigated by other authors[42, 43, 148, 149]. One important characteristic of the quadratic phase lens is the existence of a virtual aperture. This can be understood by noticing that the phase gradient of a quadratic function (Eq. 3.3) increases linearly with r. At $r > f$, $d\phi/dr$ is greater than $2\pi/\lambda$ or the free-space wave number, and therefore waves exiting the metasurface become evanescent. In other words, the incident light will either be reflected or trapped in the substrate by total internal reflection. For an oblique incident beam, a virtual aperture with the same radius f is similarly present with its center shifted to $x = -f sin\theta$. The presence of virtual apertures reduces the nominal transmission efficiency of quadratic lens when normalized against incident power over the entire metasurface area (which can be up

to 4 times larger than the virtual aperture area). The large phase gradient at the outer region of a quadratic lens also constrains the practically attainable FOV due to phase discretization effect as pointed out by Lassalle *et al*[150].

Despite its conceptual simplicity and elegance, one drawback of the quadratic singlet design is that it incurs large spherical aberration, resulting in significant stray background as well as low focusing efficiency. This shortcoming of quadratic phase singlet can be mitigated by incorporating a second metasurface layer to correct spherical aberration. The doublet configuration consists of two layers of cascaded metasurfaces, the bottom metasurface carries the main focusing power, and the top metasurface functions as a phase corrector analogous to a Schmidt plate in classical refractive optics, designed to have a phase distribution that neutralizes the spherical aberration of the bottom lens at normal incidence. At oblique incidence, two changes to the optical phase distribution are introduced compared to the normal incidence case. First, the oblique incident beam carries an additional in-plane linear phase gradient, which combines with the quadratic phase yields a laterally displaced quadratic phase profile. The top metasurface phase is also projected to a laterally shifted, off-center position. A laterally offset hyperbolic phase distribution can be recovered when the lateral displacements of the bottom metasurface quadratic phase and the top metasurface correcting phase are aligned, thus producing a sharp focal spot in a telecentric configuration.

The WFOV design approaches discussed so far are based on ray optics and have not actively exploited the potential to tailor an angle-dependent optical phase profile – a capability unique to nonlocal metasurfaces[151]. The basic principle of angular phase control is to engineer the metasurface's phase distribution ϕ such that its dependence on spatial coordinates and AOI fulfills Eq. 3.2. This can be accomplished by topology optimization (TO), which explores the tremendous number of design variables available in a complex, deep sub-wavelength metamaterial structure via gradient-based optimization[152–156]. The technique has already been extensively applied to designing freeform metasurfaces[69, 157–161] as well as other nanophotonic structures with non-intuitive geometries[162–167].

Compared to other WFOV metalens designs, this scheme uniquely allows an ultra-thin profile approaching the fundamental thickness limit of WFOV optics without compromising focusing quality. The presence of the thickness limit can be rationalized by considering the angular memory effect[168]: when a light beam incident on a disordered medium is tilted, the transmitted wavefront remains identical in shape albeit tilted by the same angle, provided that the input wave vector change is smaller than approximately one over the medium thickness. The angular memory effect stipulates that the metasurface optics must be sufficiently thick to accommodate a phase profile which sensitively depends on the AOI. Li et al. formulated lower bound of metalens thickness L for diffraction-limited WFOV metalenses defined in terms of the lens NA, angular FOV (in radian), and the output aperture size s:[169]

$$L \sim \left(\frac{1}{3}NA\right) \cdot s \cdot sin\left(\frac{\pi}{2}sin\frac{FOV}{2}\right) \tag{3.5}$$

For typical metalenses with $\sim 1mm$ aperture size, Eq. 3.5 specifies a thickness bound of $\sim 100\mu m$ - far below those of the aperture stop or doublet designs. In comparison, the inversed designed multilayer metalenses[170] are able to closely approach this limit. In addition, as one may intuitively anticipate, increasing aperture size, NA, and FOV require more rapid angular variations of the optical phase, therefore warranting a larger multilayer metasurface thickness. The escalating structural complexity ultimately delimits the practically accessible optics dimensions. Finally, the bound in Eq. 3.5 only applies to lenses with (near-)diffraction-limited quality. Heavily aberrated lenses, such as the quadratic phase singlet, are not subjected to the thickness limit[171, 172].

Geometric aberrations pertinent to WFOV imaging can also be alleviated by dividing up the FOV into a multitude of sub-segments and using a separate set of optics to address each sub-FOV. The sub-images are then stitched together computationally to capture the full WFOV scene. This multi-aperture scheme has been implemented with refractive microlens arrays[173–177], and more recently with metalenses[178].

The key advantage of the multi-aperture scheme is that each imaging element can

be individually optimized to attain minimal aberration and distortion within a small sub-FOV. The main limitation is the reduction of optical throughput: for an imager that divides the FOV to j segments, the total received signal is approximately lower by j-fold, which compromises the signal-to-noise ratio (SNR) and dynamic range. The multi-aperture design could be useful when very large optical apertures are needed, in which case the geometric aberrations of a single-aperture WFOV system become challenging to suppress.

The approaches discussed thus far have all relied upon metasurfaces or DOEs on a flat plane commensurate with standard microfabrication technologies. Recent advances have enabled fabrication of optical and optoelectronic devices on curved surfaces, either via direct writing techniques[179–181] or conformal integration of flexible membranes[173, 182–185]. This new possibility has inspired alternative designs exploiting curved optical elements. An aplanatic lens free of both spherical and coma aberrations can be realized by integrating a metasurface or diffractive optics on a spherical surface[186, 187]. The aplanatic imaging condition, which builds on the Abbe sine condition, is however only rigorously satisfied for small objects and thus does not scale to large FOV[188]. Another approach makes use of a monocentric configuration, whose spherical symmetry naturally eliminates coma and astigmatism[189–191]. For example, large-angle focusing has been demonstrated with in-plane (i.e. 2-D sectioned) Luneburg lenses[192, 193], although implementation of a 3-D Luneburg lens at optical frequencies remains a non-trivial challenge[194]. Non-planar metasurface optics can also potentially be coupled with curved image sensors (focal plane arrays) to further suppress aberrations[195].

In this chapter, we introduce a simple architecture to increase the FOV of the flat lens by placing an aperture stop in front of a flat metasurface. We start with deriving an analytical solution to optimize the phase profile of the WFOV metalens, and analyze the dependence of focusing quality on the design parameters. We then proceed with demonstrating a few applications, analyzing its working bandwidth properties, and we finally draw the conclusion at the end of the chapter.

3.2 Optimization of wide field-of-view metalens: an analytical solution

The basic concept of the single-layer WFOV flat lens is illustrated in Fig. 3-1a. An aperture is placed at the front surface of a substrate and a metasurface (or a DOE surface) is patterned on the back surface to act as an optical phase mask. Beams from different angles of incidence (AOIs) are refracted at the front surface and arrive at different and yet continuous portions of the backside phase mask. This architecture and optimized designs enable diffraction-limited focusing performance continuously across the near-180° FOV [1]. At large AOIs, the optical transmission drops due to the cosine dependence of the projected aperture area, which ultimately limits the practical FOV. This limitation can be potentially addressed by using a front aperture with a curved surface.

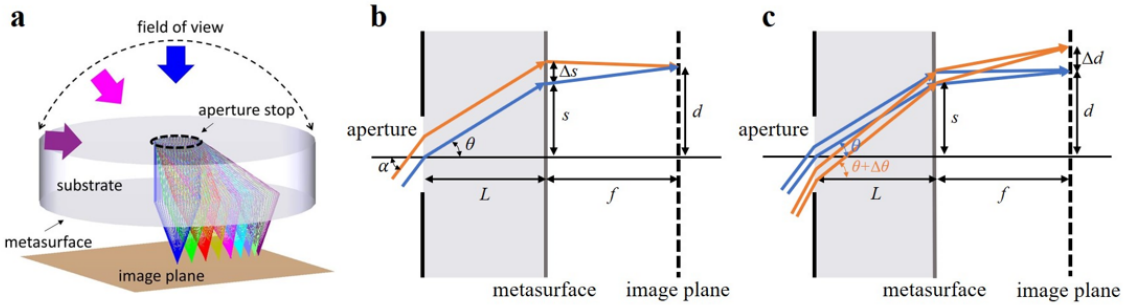

Figure 3-1: Schematic illustration of WFOV metalens design. (a) 3-D structure. (b) Illustration of the phase profile derivation. (c) Illustration of the image height derivation. Fig. 1(a) is reprinted with permission from the American Chemical Society[1].

The phase profile of the metasurface will be derived by assuming stigmatic focusing for a pencil of parallel rays incident on the aperture from all directions across the 180° FOV. In the WFOV lens configuration depicted in Fig. 3-1b, the phase profile of the metasurface is given by a function $\phi(s)$, where s denotes the radial position from the lens center. Here we consider two parallel rays separated by a small spacing Δs both focused by the metasurface to the same point on the image plane. The AOI of the rays inside the substrate is labeled as θ. The stigmatic focusing condition specifies

that their propagation path length difference must be exactly compensated by the metasurface, which yields:

$$\Delta s \cdot nsin\theta + \Delta\phi\frac{\lambda}{2\pi} + \left(\frac{\partial}{\partial s}\sqrt{(s-d)^2+f^2}\right)\Delta s = 0. \tag{3.6}$$

Here n is the refractive index of the substrate, λ is the free-space wavelength and $\Delta\phi$ gives the phase difference the metasurface imparts on the two rays. All other variables are defined following Fig. 3-1b. The first term corresponds to the phase difference accumulated at the aperture side, the second term is the one given by metasurface, the third term comes from the difference between the two converging rays separated by distance Δs from metasurface to the focal spot. Integration of ϕ in Eq. 3.6 with respect to s reveals the phase profile of the metasurface:

$$\phi(s) = -\frac{2\pi}{\lambda}\int_0^s \left(\frac{ns}{\sqrt{s^2+L^2}} + \frac{s-d}{\sqrt{f^2+(s-d)^2}}\right) ds. \tag{3.7}$$

The only unknown variable in Eq. 3.6 is d, the image height, which is a function of the AOI of the light ray. To determine d, we now consider the configuration in Fig. 3-1c, where two pencils of parallel rays with slightly different AOIs θ and $\theta+\Delta\theta$ impinge on the same metasurface area. The two pencils of rays are focused on two different spots on the image plane with image heights of d and $d+\Delta d$, respectively. For the rays with AOI $= \theta$, it follows Eq. 3.6. Similarly, for the rays with AOI $= \theta + \Delta\theta$, the condition becomes:

$$\Delta s \cdot nsin(\theta+\Delta\theta) + \Delta\phi\frac{\lambda}{2\pi} + \left(\frac{\partial}{\partial s}\sqrt{(s-(d+\Delta d))^2+f^2}\right)\Delta s = 0 \tag{3.8}$$

Since the two pencils of rays share the same metasurface area, $\Delta\phi$ is the same for Eqs. 3.6 and 3.8 assuming that the angular dependence of meta-atom phase delay is weak, an assumption that is in general satisfied for waveguide-type and resonator-type meta-atoms, which are commonly employed in meta-optics. In the case of strong angular dependence, the second term of Eq. 3.8 should be modified to include the

dependence of AOI, and the phase profile can be similarly derived as follows. Eq. 3.8 - Eq. 3.6 yields an equation relating d to θ:

$$ncos\theta\Delta\theta + \frac{\partial}{\partial d}\left(\frac{s-d}{\sqrt{(s-d)^2+f^2}}\right)\Delta d = 0 \tag{3.9}$$

The AOI from free space α is related to θ via the Snell's law $sin\alpha = nsin\theta$, and hence Eq. 3.9 translates to:

$$\Delta d = \left[\left(\frac{Lsin\alpha}{\sqrt{n^2-sin^2\alpha}} - d\right)^2 + f^2\right]^{\frac{3}{2}} \frac{cos\alpha}{f^2}\Delta\alpha \tag{3.10}$$

Substituting Eq. 3.10 into Eq. 3.7 leads to the integral form of the target phase profile.

The derivation is generic and applicable to different wavelengths, substrate materials, and meta-atom or diffractive element designs. It can also be extended to cases with multiple substrate layers (with thickness of the i-th given by L_i). In this case, the new expression of $s = \sum_i L_i tan\theta_i$ can be substituted into Eq. 3.6 and the rest of the analytical formalism remains similar. This is a useful architectural variant which not only opens a larger design space but also allows incorporation of an air gap in between solid substrates to reduce weight or a solid spacer to facilitate fabrication and assembly processes.

The main assumption in this analytical formalism is that Δs is an infinitesimal quantity, which suggests that the ideal stigmatic focusing condition is only rigorously satisfied in the "small aperture" limit. This is intuitive since larger aperture size leads to more spatial overlap of the pencils of rays with different AOIs, which tends to degrade the focusing performance. Next we consider this finite aperture size effect and derive the condition that yields the optimal performance.

When Δs is not an infinitesimal quantity, the optical path length difference ΔP between the two rays in Fig. 3-1b can be derived in a manner similar to Eq. 3.6:

$$\Delta P = \Delta s \cdot n sin\theta + [\phi(s+\Delta s) - \phi(s)] \left(\frac{\lambda}{2\pi}\right) + \sqrt{(s+\Delta s-d)^2 + f^2} - \sqrt{(s-d)^2 + f^2} \tag{3.11}$$

To ensure sharp focusing, ΔP must be minimized. Using Eq. 3.7 and Eq. 3.10 and note that d is a function of s, we compute the first three orders of derivatives of ΔP with respect to Δs:

$$\frac{d(\Delta P)}{d(\Delta s)} = 0 \tag{3.12}$$

$$\frac{d^2(\Delta P)}{d(\Delta s)^2} = 0 \tag{3.13}$$

$$\frac{d^3(\Delta P)}{d(\Delta s)^3} = -\frac{3nL^2(s-d)}{\left(f^2 + (s-d)^2\right)(L^2+s^2)^{\frac{3}{2}}} \tag{3.14}$$

Denoting aperture diameter as D, we compute RMS wavefront error σ across the aperture using the derivatives to characterize aberration when $D < f$:

$$\sigma \approx \frac{3nL^2D^3|s-d|}{160\left(f^2 + (s-d)^2\right)(L^2+s^2)^{\frac{3}{2}}} \tag{3.15}$$

This expression explicitly reveals the dependence of lens performance on configuration parameters including focal length, aperture size, substrate thickness and refractive index of substrate. To achieve better performance, one can in general increase the f-number (aka decreasing numerical aperture NA), increase the substrate thickness, and/or reduce the refractive index of substrate. An alternative strategy is to minimize the term $|s-d|$, which implies that a telecentric configuration is conducive to enhanced focusing quality. We further note that this term is dependent on n, L and f according to Eq. 3.10, which constrains these parameters and explains for example the existence of an optimal substrate thickness for best focusing performance. We want to emphasize that rigorously speaking, our lens structure is not telecentric since the exact condition $s = d$ is inconsistent with Eq. 3.9 and Eq. 3.10.

When $|s-d|$ is much smaller than f and L, the aberration becomes dominated by the fourth order derivative and the RMS wavefront error σ is:

$$\sigma \approx \frac{nL^2D^4}{192\sqrt{5}f^2\left(L^2+s^2\right)^{\frac{3}{2}}}\left|\frac{nL^2f}{\left(L^2+s^2\right)^{\frac{3}{2}}}-2\right| \tag{3.16}$$

The equation reveals a similar dependence of lens performance on design parameters.

We show in the following that the design maintains diffraction-limited performance over the entire hemispherical FOV up to a moderate NA of ~0.25 (corresponding to f/1.9), and that the analytical solution is consistent with numerically optimized designs by considering an exemplary WFOV metalens design operating at 5 μm wavelength. The lens consists of a 1 mm diameter circular aperture on the front side and a 5 mm diameter circular metasurface on the back side of a 2 mm thick BaF_2 substrate ($n = 1.45$). The effective focal length (spacing between the metasurface and the image plane) is set to 2 mm, corresponding to a NA of 0.24. The analytically derived radial phase profile ϕ and image height d are presented in Figs. 3-2a and 3-2b. As a comparison, we performed numerical optimization using a direct search algorithm [196–200] , and the optimized phase profiles are plotted in the same graphs. The results confirm excellent agreement between the two approaches.

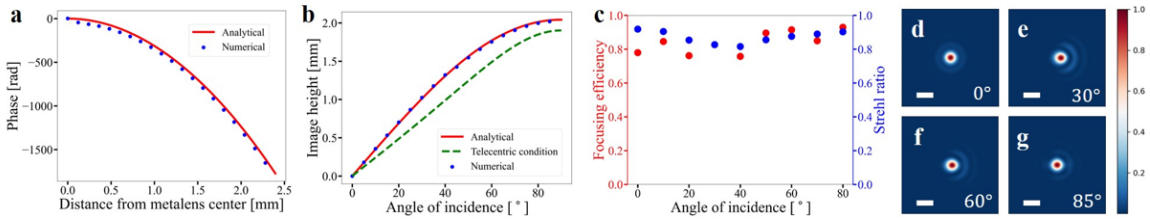

Figure 3-2: Calculated performance of an ideal WFOV lens. (a) Lens phase profile retrieved from analytical and numerical solutions. (b) Image heights with different AOIs from analytical and numerical solutions. The green dashed line represents the telecentric condition which corresponds to $d = s = \frac{Lsin\alpha}{\sqrt{n^2-sin^2\alpha}}$. (c) Focusing efficiency and Strehl ratio for different AOIs. (d)-(g) Normalized intensity profiles at image plane with different AOIs (scale bars are 20 μm)

We then used Kirchhoff diffraction integral [201] to evaluate the focusing performance of the lens. Assuming a meta-atom pitch of 4 μm, the lens focusing efficiency

Table 3.1: **Meta-atom phase delays and transmittance values**

Index	a	b	c	d
Phase delays [°]	0.7	45.0	90.2	135.0
Transmittance	0.84	0.93	0.93	0.95
Index	e	f	g	h
Phase delays [°]	180.1	224.8	269.9	315.3
Transmittance	0.89	0.90	0.92	0.94

(defined as the fraction of power encircled within an area of a diameter equaling to five times the focal spot full-width-at-half-maximum normalized by the total incident power) and Strehl ratio as a function of AOI from air are shown in Fig. 3-2c, and the focal spot profiles at several AOIs are displayed in Figs. 3-2d-3-2g. The lens exhibits diffraction-limited focusing performance with Strehl ratios consistently larger than 0.8 and efficiencies higher than 75% over the entire hemispherical FOV.

The diffraction integral calculations above assume ideal meta-atoms so the metasurface acts as a pure phase mask without imposing intensity modulation and phase error. To make a realistic estimate of the metalens efficiency, next we incorporated actual meta-atom structures and their optical characteristics modeled using full-wave calculations [202]. The all-dielectric, free-form meta-atoms under consideration are made from 1 μm thick PbTe film resting on a BaF_2 substrate [203, 204]. Sample meta-atom structures are shown in Fig. 3-3. The 2-D pattern of each meta-atom was generated with a "Needle Drop" approach. Several rectangular bars, with a minimum generative resolution of 1 pixel, were randomly generated and placed together with a square canvas (64 $\times$ 64 pixels) to form random patterns. The quasi-freeform meta-atoms offer enhanced transmission efficiency and phase coverage compared to meta-atoms with regular geometries[202]. To minimize inter-cell coupling, a minimum spacing of 8 pixels was applied between adjacent meta-atoms.

Full-wave electromagnetic simulations were performed with TE polarization (electric field always parallel to the horizontal direction in the figures) to obtain the phase delays of these generated structures. Then, the phase delays were discretized into 8 groups with $\frac{\pi}{4}$ spacing, and the optimum structures were chosen according to a figure-of-merit which aims to minimize phase deviations and maximize transmission

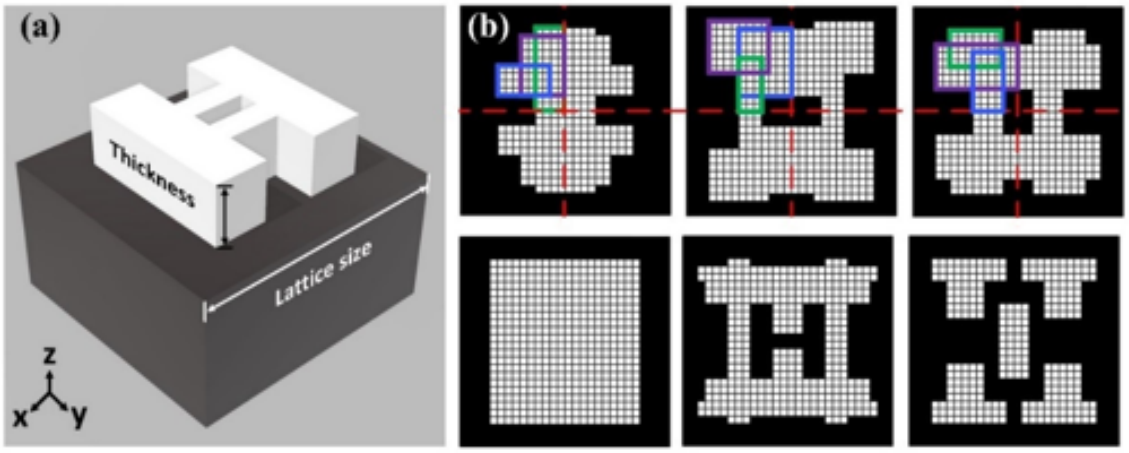

Figure 3-3: Examples of generated meta-atom structures. (a) 3-D view. (b) Several examples of generated 2-D patterns. Rectangles outlined in different colors represent randomly generated high-index "Needles".

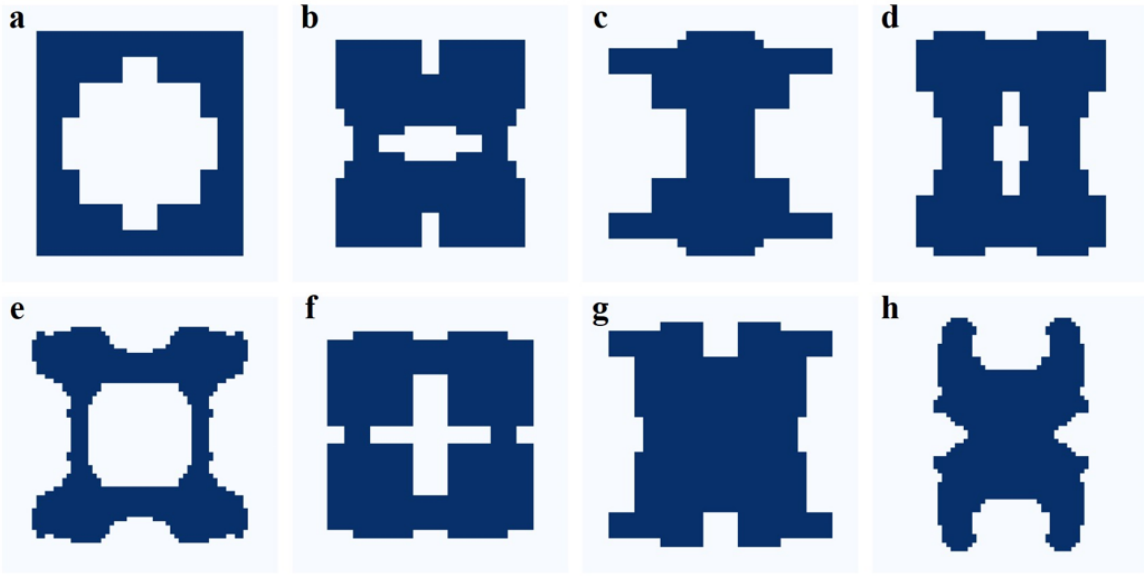

Figure 3-4: Selected 8 meta-atom structures.

amplitudes[65]. The 8 selected meta-atom structures are shown in Fig. 3-4. Their phase delays and transmittance values are summarized in Table 3.1. Our prior work have shown that the dependence of meta-atom phase on AOI is relatively weak for this type of meta-atoms and therefore does not impact the accuracy of the analytical solution[1].

The simulation results are shown in Fig. 3-5. The focusing efficiency and Strehl ratio are slightly reduced compared to the results in Fig. 3-2 (which assumes ideal meta-atoms) due to non-unity efficiency and phase error of the simulated meta-atoms. All factors considered, the lens maintains high efficiencies exceeding 65% and diffraction-limited imaging performance with Strehl ratios above 0.8 across the entire FOV.

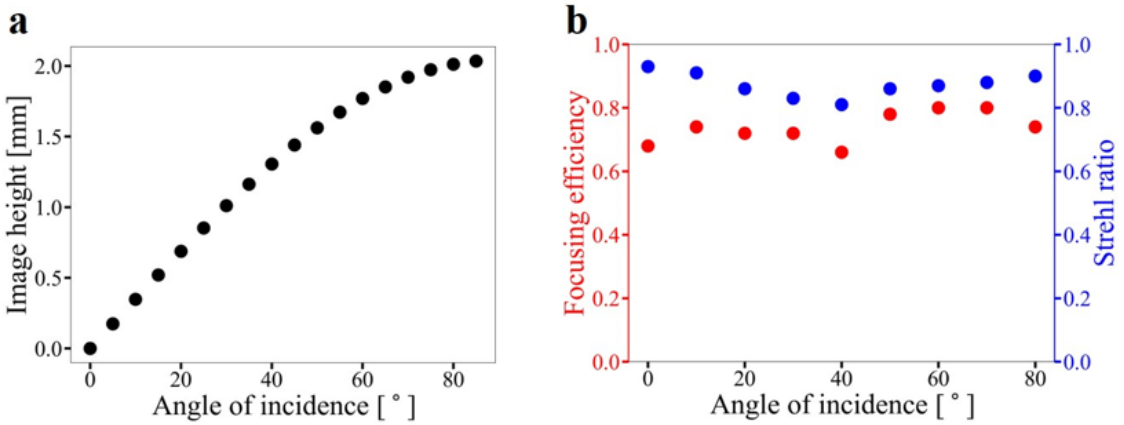

Figure 3-5: Simulated performance of a metalens composed of realistic meta-atoms. (a) Image height, (b) efficiency and Strehl ratio for different AOIs based on full-wave modeled meta-atoms.

The analytical formalism allows computationally efficient design of WFOV flat lenses, especially in cases where ray tracing based numerical optimization cannot be implemented in a reasonable time scale. The analytical solution also elucidate the design trade-offs. For a given wavelength and substrate refractive index, the WFOV lens design is fully defined by three independent parameters: aperture size, substrate thickness, and focal length. In the following, we investigate the effect of varying aperture size, substrate thickness and focal length on focusing performance of the lens for a substrate index $n = 1.45$ and a wavelength $\lambda = 5$ μm. The conclusions can be readily generalized to an arbitrary wavelength as the underlying Maxwell's

equations are scale-invariant.

Figs. 3-6a and 3-6b plot the focusing efficiency and Strehl ratio values (both averaged over the entire near-180° FOV) for WFOV flat lenses with varying NAs. In Fig. 3-6a, the lens aperture diameter is fixed to 1 mm, the substrate thickness is 2 mm, and the focal length is varied to obtain different NAs. In Fig. 3-6b, the focal length is set to 2 mm, the substrate thickness is 2 mm, and the aperture diameter is varied. Shorter focal length requires more abrupt change of optical phase whereas spatial overlap between beams with different AOIs increases with larger aperture size, both of which negatively impact the focusing quality. Consequently, both efficiency and Strehl ratio decrease with increasing NA. Fig. 3-6c depicts the impact of varying the substrate thickness. Increasing substrate thickness leads to lower spatial overlap between beams with different AOIs, thereby improving the focusing quality albeit at the expense of larger device footprint, which explains the improvement of Strehl ratio at thicknesses less than 2 mm. Notably, when the substrate thickness exceeds 2 mm, the design significantly deviates from the telecentric configuration, resulting in lower Strehl ratios. As a result, an optimum thickness arises which maximizes the Strehl ratio as shown in Fig. 3-6c. All these results are in accordance with Eq. 3.15.

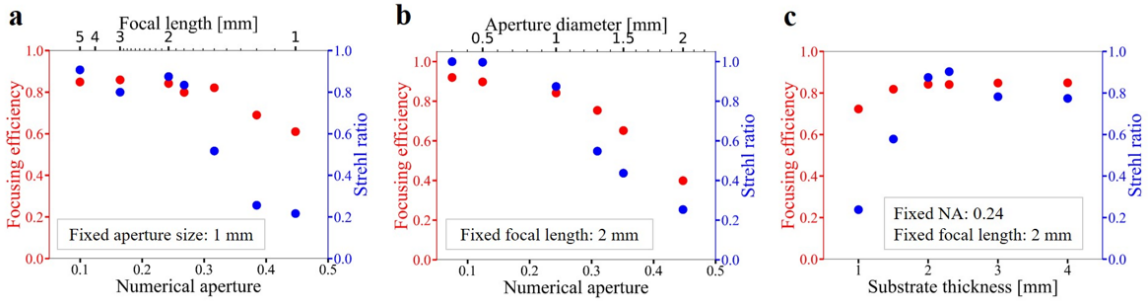

Figure 3-6: (a)-(b) Effects of NA on efficiency and Strehl ratio averaged over the entire near-180° FOV by changing (a) focal length and (b) aperture size. (c) Effects of substrate thickness on averaged efficiency and Strehl ratio.

3.3 Wide field-of-view imaging in long wave infrared band

In this section, we apply the prementioned WFOV metalens architecture and design concept to long wave infrared (LWIR) band and characterize its imaging performance. LWIR, which coincides with the peak blackbody emission wavelengths of near-room-temperature objects, is strategically important to wide-ranging imaging applications spanning nigh vision, remote sensing, robotics, industrial process monitoring, building inspection, automotive sensing, gas detection, and beyond. Since most classical optical materials such as oxide glasses and polymers become opaque at LWIR due to phonon absorption, traditional LWIR optics resort to specialty materials such as single-crystalline Ge and chalcogenide glasses. These materials either incur a high cost to manufacture (Ge), or are mechanically fragile (chalcogenide glasses). Moreover, classical refractive optics made from these materials (Ge in particular) are temperature-sensitive due to thermo-optic focal drift. The challenges are further exacerbated when it comes to applications demanding a wide field-of-view (WFOV), since classical WFOV infrared optics entail a compound lens architecture comprising multiple (in general 4 or more) stacked optical elements to suppress coma aberration[205]. As a result, even LWIR lenses with a moderate FOV of around 60° each cost well above $1,000 off-the-shelf.

While a large collection of metalenses have been implemented at visible and near-infrared wavelengths, relatively few demonstrations targeted the LWIR regime. Pioneering work by several groups have realized silicon-based LWIR metalenses [206–209]. Using Si as the metasurface material is advantageous in that it is amenable to large-area wafer-level manufacturing processes, and that deep reactive ion etching (DRIE) can produce high aspect ratio Si meta-atom structures ideal for large optical phase coverage and potentially dispersion engineering [210]. Si wafers prepared using the common Czochralski method, however, are known to exhibit a strong optical absorption band centering at 9 μm wavelength due to the presence of oxygen impurity [211]. To mitigate the issue, Ge coupled with a ZnS antireflection layer has been

adopted for metalens fabrication to suppress parasitic absorption across the LWIR band [212]. The challenge of coma aberration suppression and expanding the FOV has nonetheless not been tackled by these pioneering investigations. More recently, metalens arrays comprising five lens, each covering a sub-section of the FOV, have been implemented to demonstrate LWIR imaging spanning a horizontal FOV exceeding 60° upon image stitching in post-processing [213]. The approach is however hardly scalable to WFOV applications, as a large FOV (e.g. 100°) in both horizontal and vertical directions would require tens of individual metalenses, severely curtailing the optical throughput while escalating system complexity.

Here, we report the design and experimental demonstration of a WFOV metalens covering 140° circular FOV. The metalens assumed the architecture mentioned in the last section, which consists of an optical aperture stop and a single-layer metasurface patterned in a float-zone Si wafer. The choice of float-zone Si contributes to suppression of the oxygen impurity absorption band while still enabling full leverage of industry-standard Si fabrication processes. We will start with formulating the overarching analytical design approach. Two metalens designs were derived using the method, with an air gap and a ZnSe spacer, respectively. The former features a simpler construction whereas the latter has the advantage of enhanced FOV and imaging quality as predicted by our analytical theory and validated via numerical simulations. We then proceed to describe the fabrication protocols as well as experimental characterization of both metalenses.

The WFOV metalens architecture consisting of an aperture and an all-silicon metasurface is schematically illustrated in Fig. 3-7a. The monochromatic phase profiles of the metasurfaces follows Eq. 3.7, The corresponding RMS wavefront error is given by Eq. 3.15.

As mentioned in the last section, the numerator in the expression above contains the factor $|s - d|$, which corresponds to the transverse offset between the incident position of the chief ray on the metasurface and the corresponding focal spot position (i.e., image height). In an image-space telecentric configuration, the term vanishes, yielding optimal image quality. Optimizing the metalens design therefore involves

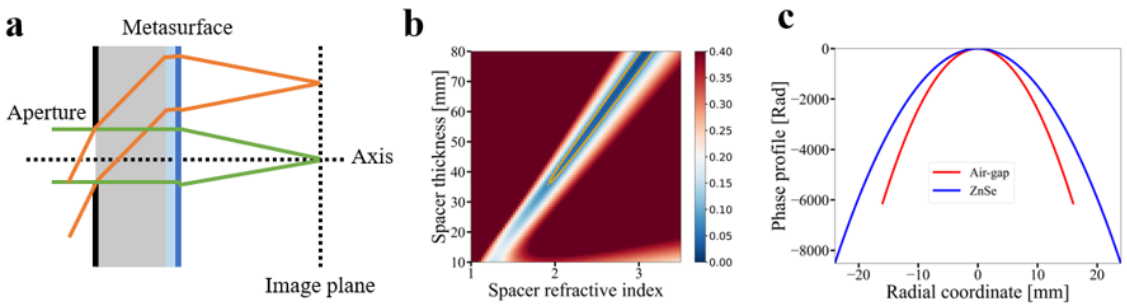

Figure 3-7: Analytically derived WFOV metalens design optimization. (a) Schematic illustration of the WFOV metalens configuration. (b) Averaged RMS wavefront error across the FOV for a range of spacer refractive indices and thicknesses. The simulations assume 140° FOV and 20 mm focal length, upper limit of the RMS wavefront error in the plot is set to 0.4 λ, the orange contour denotes area where RMS wavefront error is smaller than 0.0745 λ, which stands for diffraction-limited performance. (c) Phase profiles of the two metalens designs experimentally implemented in this study.

engineering its image height vs. incident angle relation to mimic the telecentric configuration. This can be accomplished by changing the refractive index n_{sub} of the spacer material, leveraging refraction at the air-spacer front surface as a practical means to modify the image height. Following this rationale, we examine the dependence of the RMS wavefront error for various spacer material refractive indices and thicknesses (Fig. 3-7b).

Guided by the theoretical insight, we have chosen ZnSe ($n_{sub} = 2.40$ at 10.6 μm) as the spacer material. An air-gap design ($n_{sub} = 1$) was also implemented as a comparison. The detailed design parameters are tabulated in Tab.3.2 and Fig. 3-7c plots the phase profiles of the designs.

Next we translate the phase functions into actual metasurface layouts. The all-Si meta-atom structure is depicted in Fig. 3-8a inset, which is composed of 12 μm tall pillars with a 4 μm pitch etched into float-zone Si wafers. Full-wave electromagnetic simulations were performed using the Lumerical FDTD solver, and the transmittance and phase delay of the meta-atoms at 10.6 μm wavelength as functions of the pillar diameter are shown in Figs. 3-8a-b. Eight meta-atoms with approximately $\frac{\pi}{4}$ step size in phase were chosen to construct the metasurfaces. To optimize transmittance while suppressing phase error, we invoked the figure-of-merit function in Eq. 2.1 as the

Table 3.2: Metalens design parameters

	Wavelength	Aperture size	Air-gap/ZnSe thickness	Si substrate thickness
Air-gap	10.6 μm	6 mm	7.5 mm	675 μm
ZnSe	10.6 μm	10 mm	44 mm	675 μm
	Focal length	Metalens size	Image plane size	FOV
Air-gap	12 mm	32 mm	21 mm	120°
ZnSe	20 mm	48 mm	38 mm	140°

criterion to choose the meta-atom diameters [65, 66]. The eight selected meta-atom designs are summarized in Tab. 3.3.

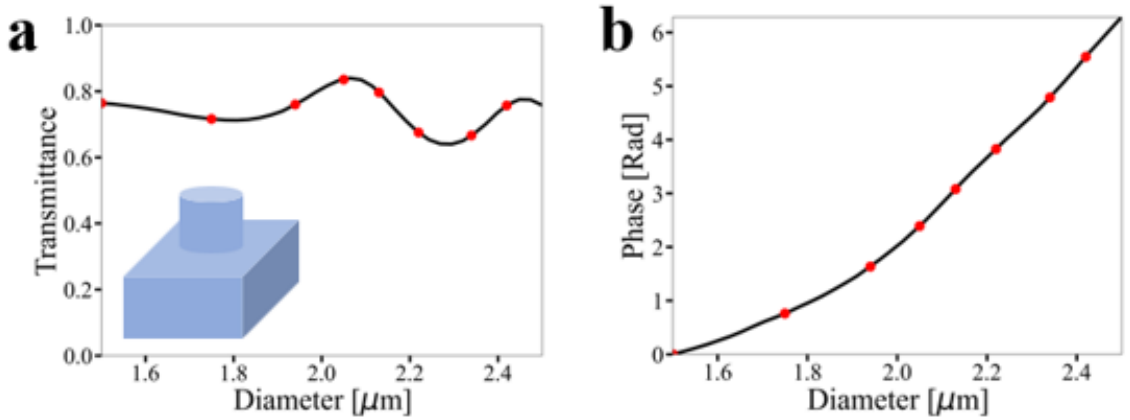

Figure 3-8: All-Si meta-atom design. (a) Transmittance and (c) phase delay responses of the meta-atoms with different pillar diameters. Red dots denote the eight meta-atom structures selected to construct the metasurfaces.

Based on the meta-atom characteristics, performances of the WFOV metalenses can be numerically evaluated using the Kirchhoff diffraction integral. The transverse and longitudinal focal spot intensity profiles of the two WFOV metalens designs at several different angles of incidence (AOIs) are presented in Fig. 3-9 and Fig. 3-9, respectively. The modulation transfer functions (MTFs) at different spatial frequencies were obtained through Fourier transform of the simulated point-spread-functions (PSFs) and are shown in Figs. 3-11a-b.

We now characterize the focusing efficiencies and Strehl ratios of the WFOV met-

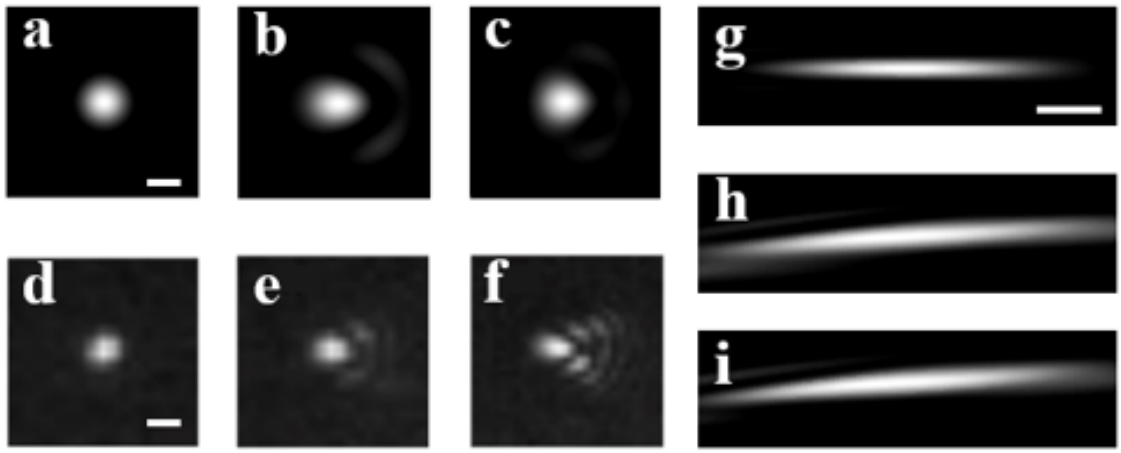

Figure 3-9: Focusing characteristics of the air-gap WFOV metalens at 10.6 μm wavelength. (a)-(c) Simulated PSFs of the metalens at its image plane for AOIs of (a) 0°, (b) 20°, and (c) 40°. (Scale bar: 20 μm.) (d)-(f) Measured PSFs of the metalens at its image plane for AOIs of (d) 0°, (e) 20°, and (f) 40°. (Scale bar: 20 μm.) (g)-(i) simulated longitudinal intensity profiles of the metalens with AOI of (g) 0°, (h) 20°, and (i) 40°. (Scale bar: 100 μm)

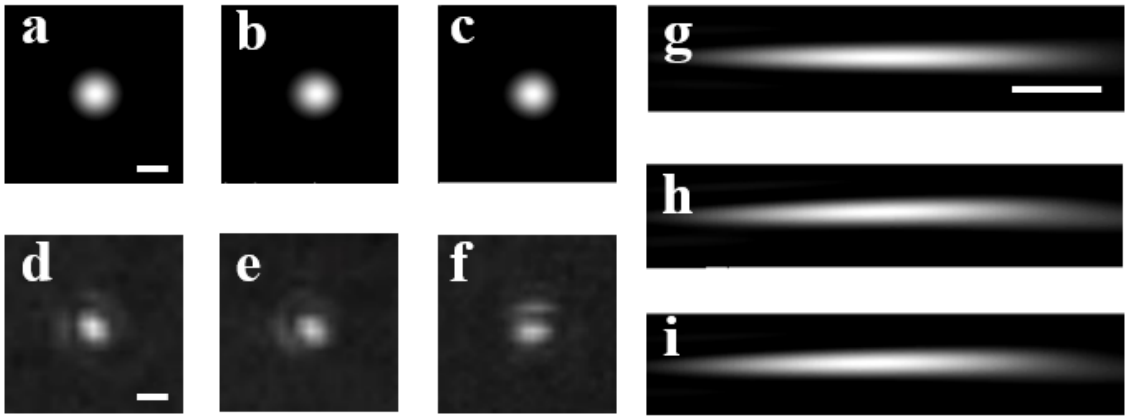

Figure 3-10: Focusing characteristics of the ZnSe-spacer WFOV metalens at 10.6 μm wavelength. (a)-(c) Simulated PSFs of the metalens at its image plane for AOIs of (a) 0°, (b) 30°, and (c) 70°. (Scale bar: 20 μm.) (d)-(f) Measured PSFs of the metalens at its image plane for AOIs of (d) 0°, (e) 30°, and (f) 70°. (Scale bar: 20 μm.) (g)-(i) simulated longitudinal intensity profiles of the metalens with AOI of (g) 0°, (h) 30°, and (i) 70°. (Scale bar: 100 μm)

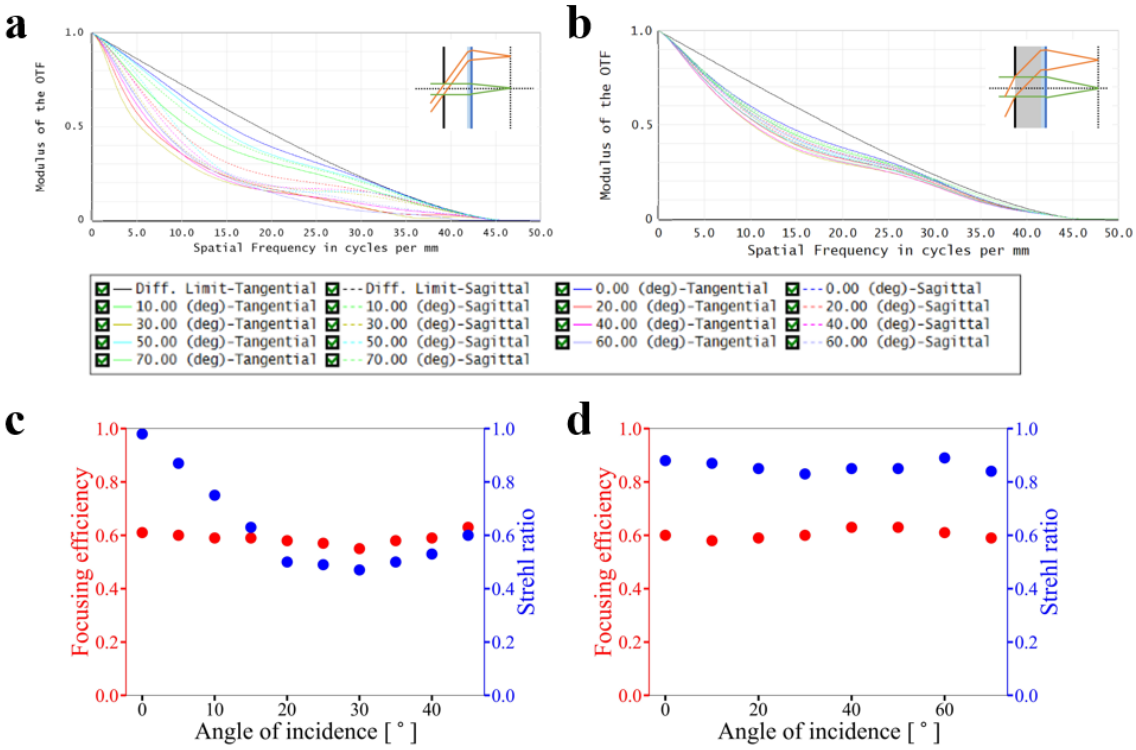

Figure 3-11: Metalens focusing performance at 10.6 μm wavelength. (a)-(b) Simulated MTFs of the (a) air-gap and (b) ZnSe-spacer metalens at different AOIs. (c)-(d) Focusing efficiency and Strehl ratio of the (a) air-gap and (b) ZnSe-spacer metalenses as functions of AOI.

Table 3.3: Meta-atom diameter, transmittance, and phase delay

Meta-atom index	1	2	3	4	5	6	7	8
Phase [°]	0	44	94	137	176	219	274	318
Transmittance	0.76	0.72	0.76	0.84	0.80	0.68	0.67	0.76
Diameter [μm]	1.50	1.75	1.94	2.05	2.13	2.22	2.34	2.42

alenses at 10.6 μm wavelength using the numerical results in Figs. 3-9 and 3-10. Here the focusing efficiency is defined as the fraction of power encircled within a diameter equaling five times the focal spot full-width-at-half-maximum (FWHM), normalized by the total incident power [214]. Figures 3-11c-d plot the two parameters as functions of AOI. The air-gap metalens has a focusing efficiency of 53% and a Strehl ratio of 0.63, both averaged over AOIs across the 90° FOV, whereas the ZnSe-spacer metalens claims a focusing efficiency of 50% and a Strehl ratio of 0.86, similarly averaged over AOIs throughout the entire 140° FOV. The enhanced focusing performance of the ZnSe-spacer lens over the air-gap design, evidenced by its diffraction-limited performance (Strehl ratio > 0.8) over an extended FOV of 140°, validates our theoretical prediction.

To fabricate the metalens, 2 μm thick SiN films were deposited by plasma-enhanced chemical vapor deposition (STS PECVD) on 675 μm thick float zone Si wafers as hard masks for DRIE. To define the metasurface patterns, a negative-tone photoresist (AZ nLOF 2035) was spin-coated onto the substrates at 3000 revolutions per minute (rpm). The resist was soft-baked at 115 °C for 1 minute, exposed on an MLA150 Maskless Aligner, and then post-exposure baked at 115 °C for 1 minute. The photoresist was developed by immersing the sample in Microposit MF-319 developer for 1 minute, followed by rinsing in deionized water. To etch the SiN hard mask, dry etching was performed using dual gas inlets with a mixture of SF6 and C4F8 (STS ICP RIE). The Bosch process was subsequently used to etch the Si meta-atoms (SPTS Rapier DRIE). To mitigate scalloping which is commonly associated with the Bosch process. Finally, the hard mask was removed with a buffered HF (BHF) wet etching process.

Figure 3-12 shows images of the fabricated metasurfaces showing a low-roughness sidewall profile with minimal scalloping.

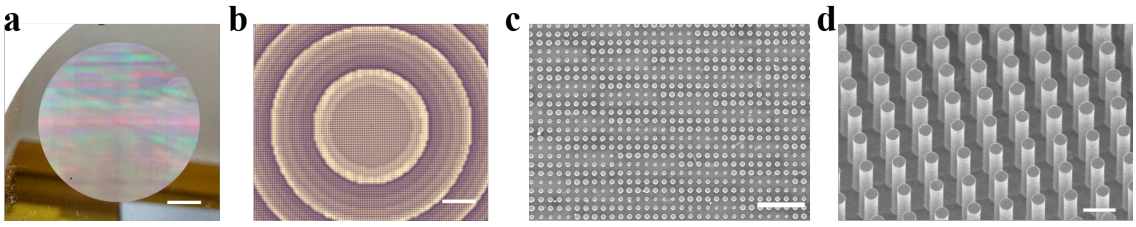

Figure 3-12: Images of fabricated metasurfaces. (a) Photo of a metasurface sample. (Scale bar: 10 mm.) (b) Optical microscopy image of the metasurface. (Scale bar: 60 μm.) (c) Top-view SEM image of the meta-atom structures. (Scale bar: 20 μm.) (d) Tilted-view SEM image showing sidewall profiles of the meta-atoms. (Scale bar: 4 μm.)

Finally, we show that even though metalenses are designed targeting a single operation wavelength of 10.6 μm, it can be applied to broadband unfiltered thermal imaging. The metalens was integrated with an uncooled focal plane array to form a thermal infrared camera. A hot plate was placed half meter away in front of the ZnSe WFOV metalens to generate thermal heat and LWIR illumination. Card board with 'MIT' pattern cut out was placed in between the hot plate and the metalens, which blocks thermal heat in all areas except the inverse 'MIT' pattern. Therefore, it serves as a heat mask, and generates an object of 'MIT' pattern shape with broad bandwidth LWIR illumination. The image was captured by a LWIR focal plane array, which is shown in Fig. 3-13.

3.4 Design of broadband and wide field-of-view metalens

Broadband operation has been a standing challenge for metasurface optics[215]. A number of techniques have been implemented to realize achromatic metalenses. One solution involves dispersion engineering of individual meta-atoms to compensate for chromatic aberration[5, 216–222]. The objective of this approach is to assemble

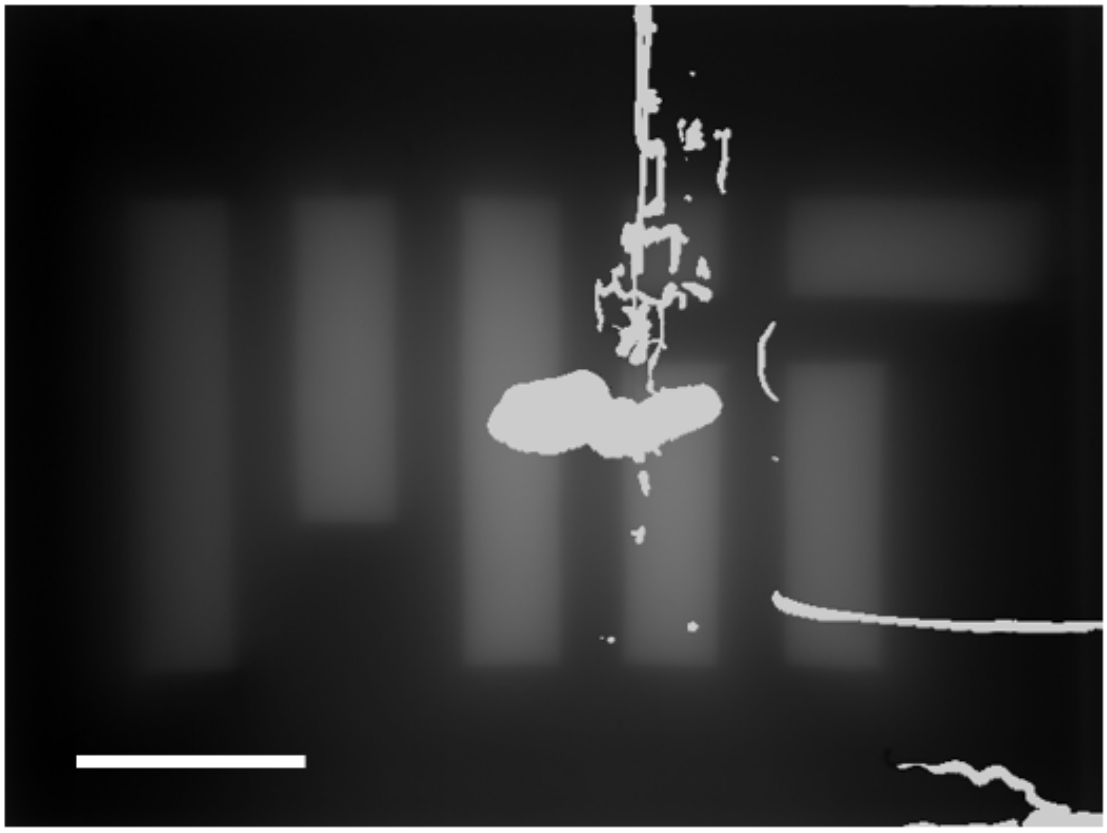

Figure 3-13: Images taken by the thermal infrared camera equipped with the ZnSe-spacer metalens. (Scale bar: 4 *mm*.)

a metalens out of meta-atoms with target dispersion behaviors such that hyperbolic phase profiles corresponding to the same focal length are fulfilled at different wavelengths. Another scheme termed 'zone engineering' has been demonstrated recently[223], where the locations and step sizes for phase wrap are judiciously engineered to maximize the phase coherence at the focal spot. Full-aperture optimization methods (instead of relying on discrete meta-atoms)[69, 170, 224, 225] and cascaded metasurface designs[31] have also been developed, although the computational load becomes prohibitively large when these methods are applied to large-aperture (mm to cm scale) optics. Finally, computational imaging has been proven to be a powerful technique to retrieve high-quality broadband images when coupled with front-end meta-optics engineering[226, 227].

In the thesis, we use the DS algorithm to optimization of metalenses comprising free-form meta-atoms. Our design process starts with generation of a set of meta-atoms with diverse dispersion responses. The generation process capitalizes on our recently developed deep learning algorithm targeting metasurfaces with high degrees of freedom[202, 204], which rapidly yields broadband optical responses (amplitude and phase) of free-form meta-atoms without resorting to full-wave electromagnetic simulations[228, 229]. We started with 3,000 randomly generated meta-atom structures using a needle-drop method[202].

Fig. 3-14 depicts the top-view layouts of several randomly selected examples of the meta-atoms. All meta-atoms in the library are patterned from a 1.4 μm thick Si layer resting on a SiO_2 substrate with a uniform period (pitch) of 0.5 μm. The amplitude and phase responses of the meta-atoms modeled using the deep neural network and full-wave simulations are also compared in Fig. 3-14, showing excellent agreement between the two approaches. In this study, we did not target any specific pre-defined meta-atom dispersion when compiling the meta-atom library.

The 3,000 meta-atoms form the library for subsequent DS optimization. We verified that further expanding the library brings marginal benefits, implying that the library already covers the entire accessible meta-atom design space given the geometric conditions.

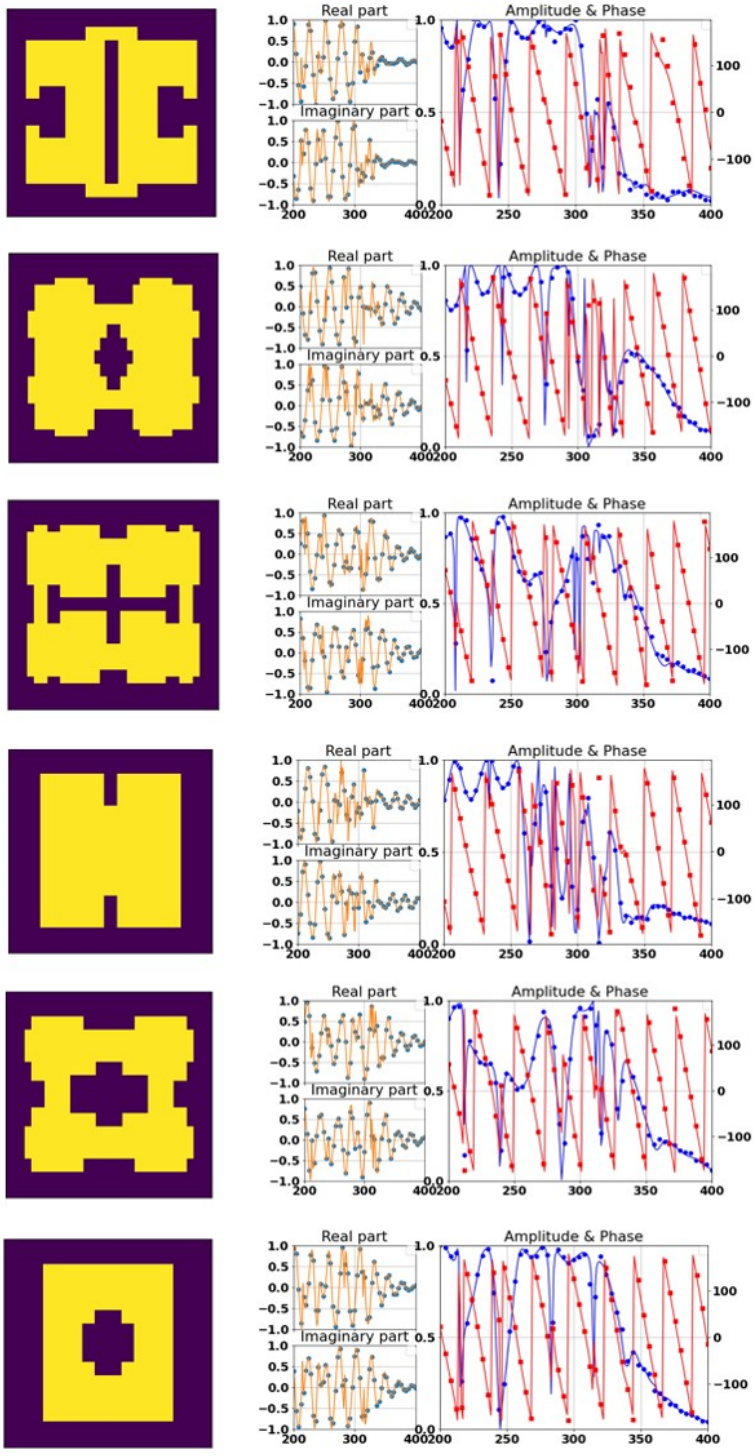

Figure 3-14: Examples of meta-atom structures top-view, and their amplitude and phase response using full-wave simulations (lines) and the deep neural network (dots).

This combination of DS optimization and deep learning algorithm is ideally suited for versatile and computationally efficient metasurface design. The deep learning algorithm is capable of rapidly generating a large number of meta-atom designs, whose free-form layouts enable the exploration of many geometric degrees of freedom to enable a wide range of dispersion properties and thereby maximally boost performance. DS also copes well with the large varieties of meta-atoms, which otherwise can present a throughput challenge for alternative optimization schemes. This is because the DS optimization is sequentially and locally performed on each meta-atom. During the performance evaluation step, partial diffraction integrals representing the contribution from all meta-atoms other than the one being replaced remain constant and thus do not need to be re-computed. Moreover, the diffraction integral evaluation is an 'embarrassingly parallel' task and was thus executed leveraging commercial cloud computing service to drastically reduce the iteration time. For this reason, the approach can be readily scaled to metasurfaces with large (centimeter-scale) optical apertures.

The main assumption of the optmization scheme is that mutual coupling between meta-atoms is insignificant. This assumption is a reasonable approximation for high-index meta-atoms with strong field confinement. However, corrections must be applied when such coupling is not negligible[230].

Our first design example is an achromatic single-layer metalens operating across the 1-1.5 μm spectral range with a diameter of 200 μm and a focal length (f) of 400 μm, corresponding to a numerical aperture (NA) of 0.24. Cross-sectional intensity distributions of the focal spot at several wavelengths and on the same image plane (f = 400 μm) are displayed in Figs. 3-15a-f, alongside the focal spot profiles from an ideal aberration-free lens of the same NA. Intensity distributions along the optical axis at these wavelengths are displayed in Figs. 3-15i-n, alongside the intensity distributions from an ideal aberration-free lens at wavelengths of 1.0 μm and 1.5 μm shown in Figs. 3-15g-h. The average longitudinal chromatic focal shift is 1.6% over the spectral range (Fig. 3-15o). The relatively small chromatic focal shift ensures that the fixed image plane falls within focal tolerance of the lens throughout most of the

spectral band, which accounts for the high Strehl ratio. The wavelength-dependent focusing efficiency (defined as the fraction of power encircled within an area of a diameter equaling to three times the focal spot full-width-at-half-maximum normalized by the total incident power) and Strehl ratio calculated using the Kirchhoff diffraction integral are plotted in Fig. 3-15p. The design yields a spectrally averaged focusing efficiency of 42% and Strehl ratio of 0.67.

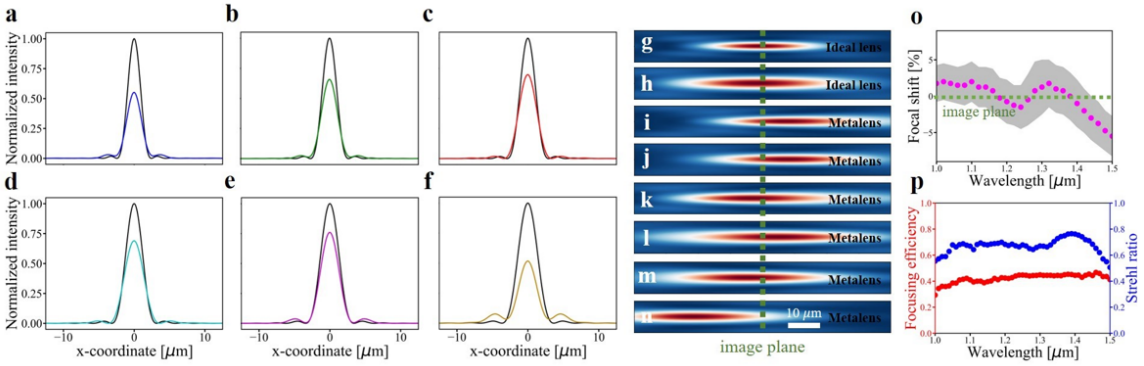

Figure 3-15: (a)-(f) Normalized intensity distributions of the focal spot on image plane at wavelengths of (a)1.0 μm, (b)1.1 μm, (c)1.2 μm, (d)1.3 μm, (e)1.4 μm, and (f)1.5 μm from the broadband metalens (color lines) and an ideal aberration-free lens (black lines). (g, h) Normalized intensity distribution along the optical axis for an aberration-free lens at wavelengths of (g) 1.0 μm and (h) 1.5 μm. (i)-(n) Normalized intensity distribution along the optical axis for the broadband metalens at wavelengths of (i) 1.0 μm, (j) 1.1 μm, (k) 1.2 μm, (l) 1.3 μm, (m) 1.4 μm, and (n) 1.5 μm. (o) Longitudinal chromatic focal shift of the metalens: the shaded area represents focal tolerance (defined as the longitudinal range where the on-axis intensity is above 80% of the peak intensity at the focal spot). (p) Focusing efficiency and Strehl ratio of the metalens.

As a comparison, we applied the same optimization approach to multilevel diffractive lenses (MDLs). In MDLs, height of unit cells on the lens surface is utilized to control the phase response of the broadband lens. In the optimization, the same unit cell period of 0.5 μm and maximum layer thickness of 1.4 μm are assumed for both metalens and MDLs. It is important to note that the broadband performances of both metalens and MDLs improve with increasing unit cell height, since the group delay increases with larger thickness.[215, 231] Therefore, the same thickness is assumed for the sake of drawing a fair comparison. Fig. 3-16 compares the simulated wavelength-averaged focusing efficiency and Strehl ratio of the metalens in Fig. 3-15

and MDLs with diffractive surface refractive indices varying from 1.5 to 3.5. The metalens offers superior efficiency and Strehl ratio compared to the MDLs thanks to the diverse dispersion characteristics of the free-form meta-atoms.

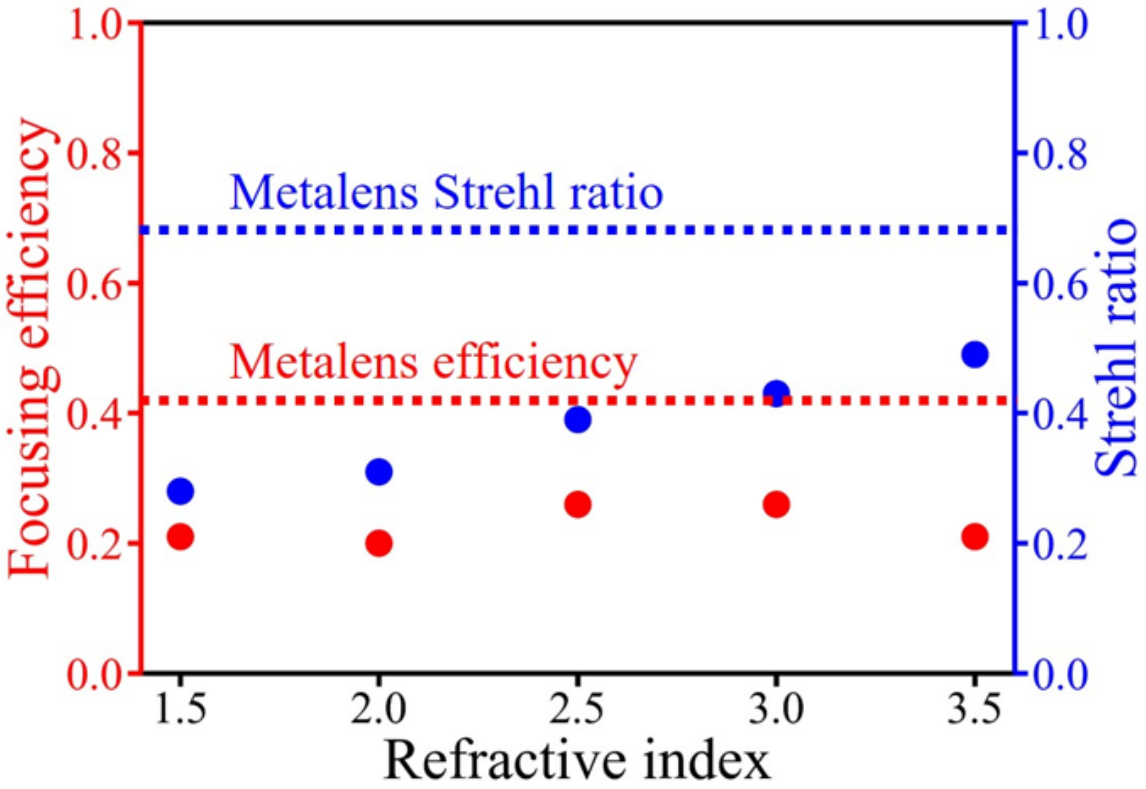

Figure 3-16: 1-1.5 μm wavelength-averaged focusing efficiency and Strehl ratio of MDLs with varying diffractive surface refractive indices. The dashed lines give performances of the metalens shown in Fig. 3-15.

We further extend the comparison of flat lenses considering a wide range of design parameters. Figure 3-17 compares the spectrally averaged focusing efficiency and Strehl ratio of metalenses and MDLs of varying NA and aperture size, both optimized using the DS approach over the 1-1.5 μm band. The diffractive surface refractive index of MDLs is set to 3.5 with a maximum thickness of 1.4 μm, the same as the metalens design. The performances of metalenses based on free-form meta-atoms are consistently superior or at least on par with their MDL counterparts. The result highlights facile dispersion engineering as an important advantage of free-from meta-atom structures[232, 233], where their increased geometric degrees of freedom enable tailor-

ing of waveguiding and multipole resonance behaviors to produce favorable dispersion responses[234, 235].

Finally, we demonstrate that the DS + deep learning design paradigm can also be harnessed to realize advanced metalens architectures. As an example, here for the first time, we present the design of a wide-FOV and broadband achromatic metalens. The configuration of the lens is illustrated in Fig. 3-18. The phase profile of the backside metasurface is optimized using the DS algorithm with the AOI-dependent image height (lateral displacement of the focal spot with respect to the optical axis) given by 3.10.

In the equation, d is the image height, $n = 1.45$ denotes the substrate refractive index, α represents the AOI, $L = 200$ μm is the substrate thickness, and the focal length is set to $f = 280$ μm. The top aperture has a diameter of 100 μm. This equation is exact for a single-wavelength design. As bandwidth increases, transverse chromatic aberration becomes more pronounced and the in-plane focal spot position progressively deviates from the equation. We note that this effect is unique to wide-FOV lenses; prior achromatic metalens designs were constrained to a small on-axis FOV and the transverse chromatic aberration is insignificant. Fig. 3-19a presents the AOI and wavelength averaged transverse chromatic focal shift as a function of metalens spectral bandwidth. The wide-FOV metalens bandwidth becomes limited by the transverse chromatic aberration rather than the axial chromatic focal shift.

We choose an exemplary design operating across 1-1.2 μm wavelength range and targeting 180° FOV, using the same meta-atom library as in the preceding examples. Within the spectral range, the transverse chromatic focal shift is far smaller than the focal spot size and thus the lens is close to achromatic. The results are shown in Figs. 3-19b-e. Kirchhoff diffraction integral was applied to calculate the focusing efficiency and Strehl ratio of the broadband and wide-FOV metalens. It maintains high focal spot quality across the entire 1-1.2 μm band and FOV with an average focusing efficiency of 45% and a Strehl ratio of 0.64.

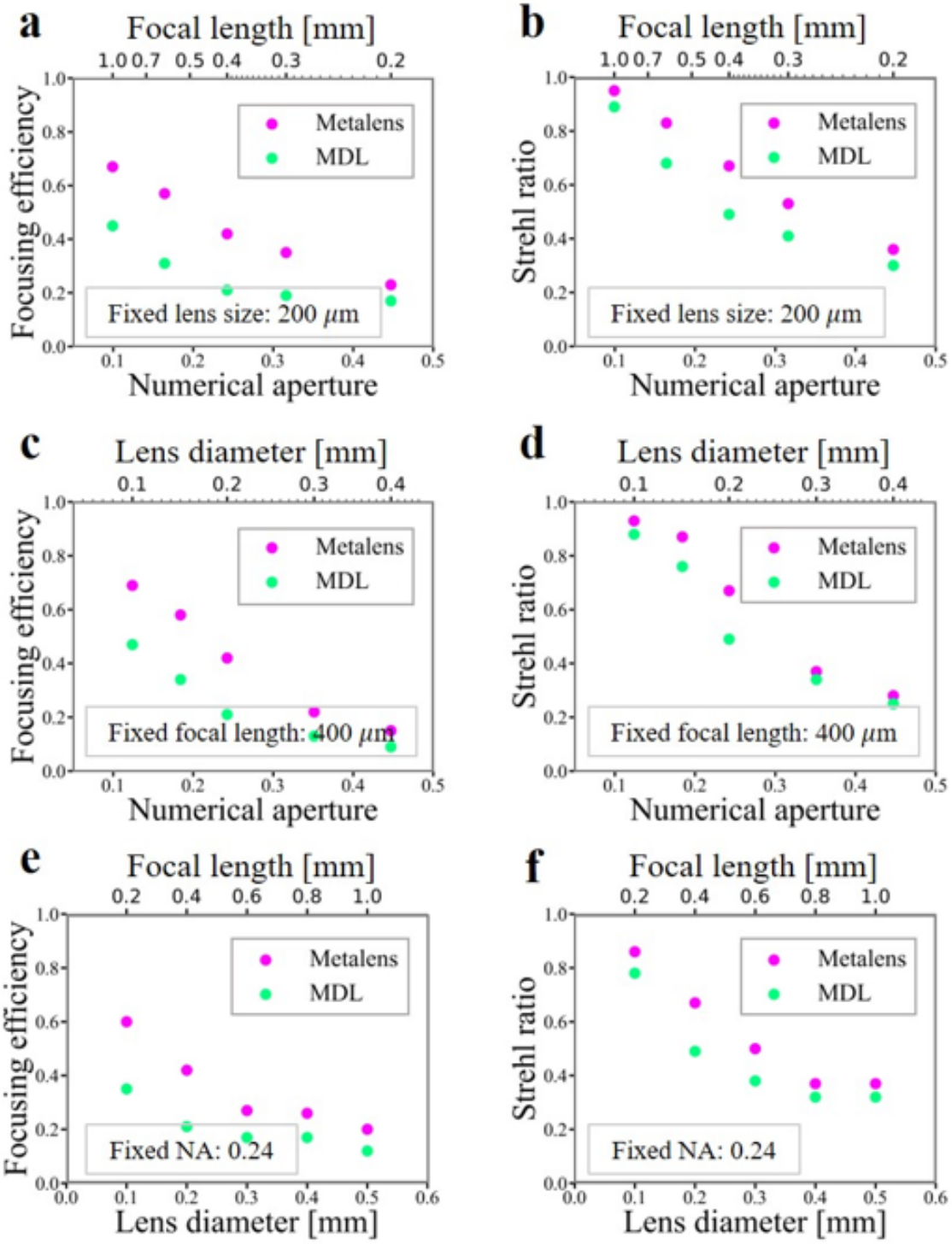

Figure 3-17: Performance comparison between metalens and MDLs with varying design parameters, showing spectrally averaged focusing efficiency and Strehl ratio as functions of: (a)-(b) NA with varying focal length; (c)-(d) NA with varying lens aperture size; and (e)-(f) aperture size with constant NA.

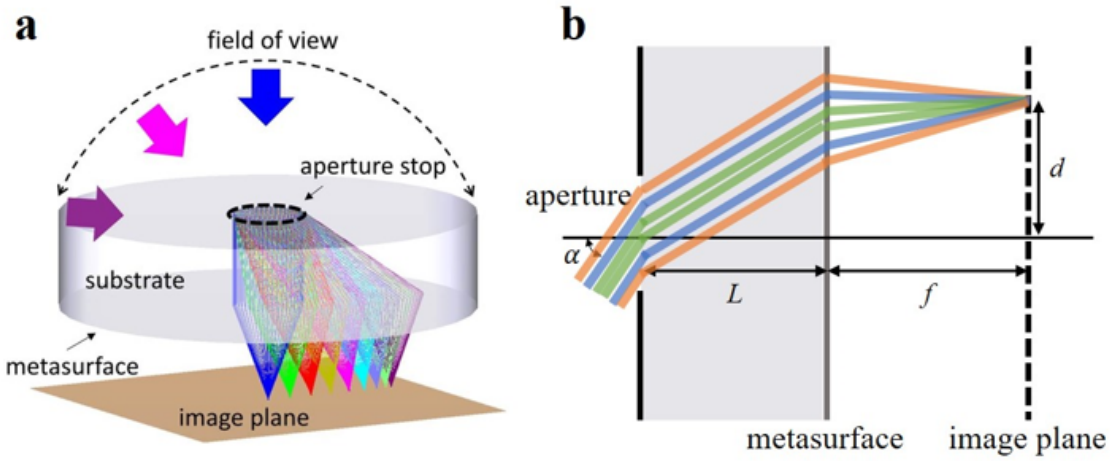

Figure 3-18: Schematic illustration of broadband and wide-FOV metalens design. (a) 3-D structure. (b) Beams of different wavelengths all focus at the same focal spot with distance d (image height) depending on AOI α.

3.5 Wide field-of-view metalens with extended depth-of-focus

Depth of focus refers to the range of distances within which objects appear sharp and in focus. Traditional lenses and the WFOV metalens in the previous sections have a limited depth of focus, meaning that only objects at a specific distance can be captured sharply, while objects in front of or behind that plane may appear blurry. However, advancements in lens technology have led to the development of lenses with extended depth-of-focus (EDOF), revolutionizing various fields such as photography, microscopy, and ophthalmology.

EDOF metalens can be designed via a wavefront coding term[112]:

$$\phi(x, y) = \frac{\alpha}{L^3}(x^3 + y^3) \tag{3.17}$$

where L is the radius of the metasurface, and α is a constant. The cubic phase generates an accelerating Airy beam and produces the EDOF PSF[236–241]. However, the EDOF metalens configurations proposed so far apply cubic phase directly onto the hyperbolic phase, and therefore are restricted to a narrow FOV due to the angle-

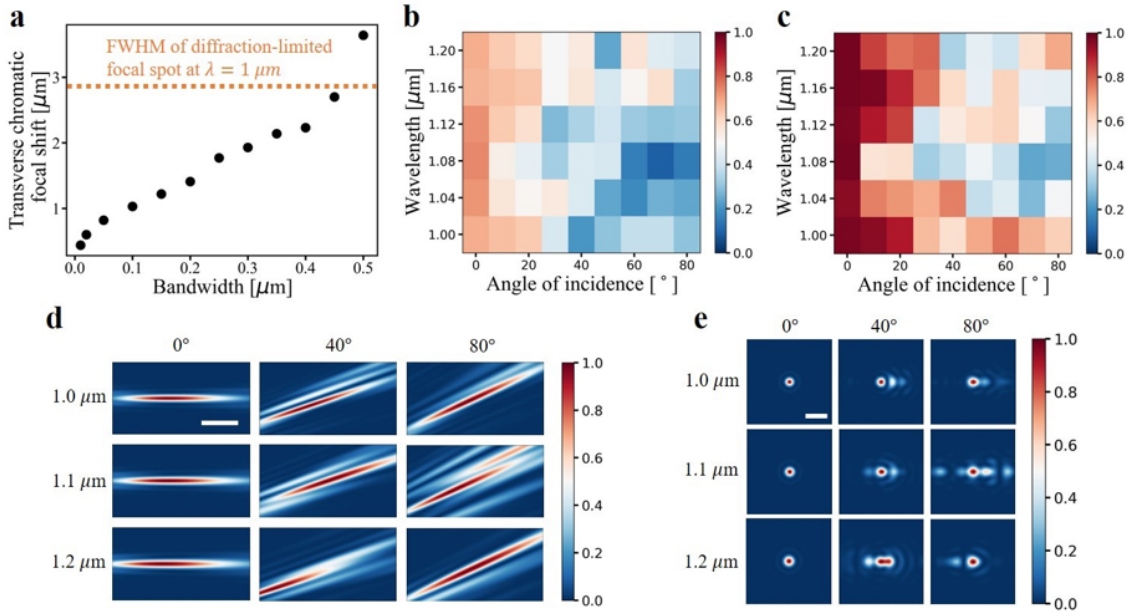

Figure 3-19: Broadband and wide-FOV metalens performance characterization. (a) Transverse chromatic focal shift (averaged over the full 180° FOV and the 1-1.2 μm spectral range) relative to the analytically derived image heights in Eq. 3.10 for wide-FOV metalenses with varying bandwidths. Here the lower end of the wavelength is fixed at 1 μm. (b) Focusing efficiency and (c) Strehl ratio dependences on both wavelength and AOI. (d) Axial intensity distributions of the focal spot on the meridional plane at different wavelengths and AOIs (scale bar: 20 μm). Centers of all the figures are the focal spot position derived from Eq. 3.10 on the image plane. (e) Intensity distributions on the image plane at different wavelengths and AOIs (scale bar: 10 μm).

dependent aberrations discussed in the previous sections. In this thesis, we combine the EDOF design concept with the aforementioned WFOV metalens architecture to obtain a metalens doublet that features EDOF in the near-180° FOV.

The doublet configuration is similar as shown in Fig. 3-1a, except that the front aperture is substituted with an EDOF metasurface. The EDOF metasurface has a diameter of 1 mm, and the WFOV metasurface has a diameter of 5.5 mm, they are separated by a SiO_2 substrate with a thickness of 2.4 mm and refractive index of 1.45. The metalens works in the wavelength of 940 nm with a back focal length of 2.86 mm. The EDOF metasurface has a cubic phase expressed in Eq. 3.17 with the constant $\alpha = 1000\pi$, the phase profile of the WFOV metasurface is expressed by the sum of polynomials following Eq. 2.2. The polynomial terms are listed in Tab. 3.4

Table 3.4: Polynomial terms of the WFOV metasurface

A_1	A_2	A_3	A_4	A_5	A_6
-1.669×10^3	7.592	-6.706	1.304×10^1	-7.390	2.083
A_7	A_8	A_9	A_{10}	A_{11}	
-3.015×10^{-1}	1.581×10^{-2}	1.238×10^{-3}	-2.029×10^{-4}	7.612×10^{-6}	

The simulated PSF using ray tracing at different object depths and AOIs are shown in Fig. 3-20, which have little variation with both object depth and AOI. Therefore, the depth-invariant image can be retrieved through deconvolution between captured image and the EDOF PSF. The detailed image deconvolution process will be discussed in detail in Chapter 5.

3.6 Summary

In conclusion, we demonstrate a few WFOV metalens designes based on a simple architecture which involves placing an aperture stop in front of a flat metasurface. Light entering the aperture is spatially dispersed depending on the AOI, and as a result beams incident at different angles interact with different (yet continuous) portions of the metasurface. The rays are then focused onto a flat image plane in a (near-

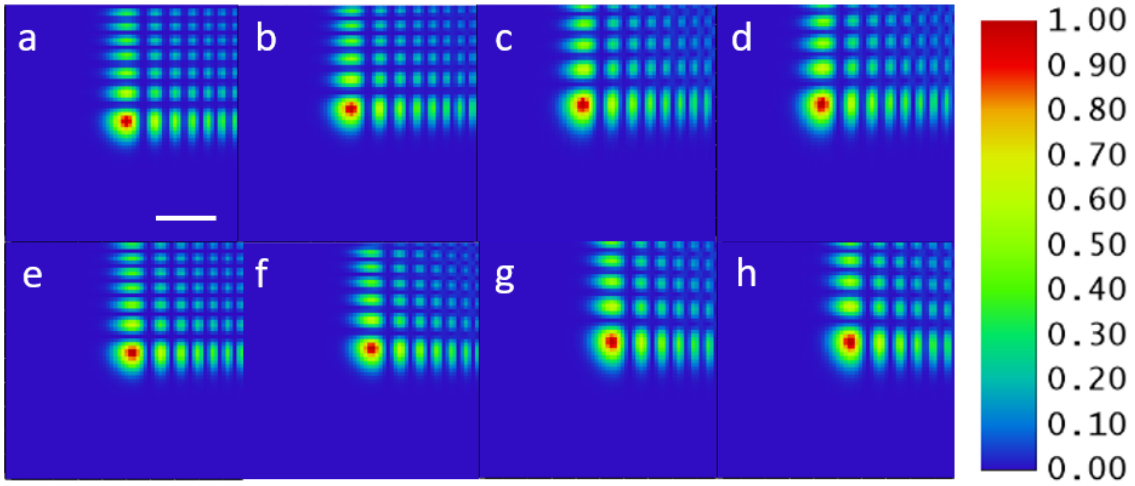

Figure 3-20: Similated PSF of EDOF WFOV metalens doublet. (a)-(d) PSF with point source distance of 3 mm and AOI of (a) 0°, (b) 60°, (c) 80°, and (d) 89°. (e)-(h) PSF with point source distance of 10 mm and AOI of (e) 0°, (f) 60°, (g) 80°, and (h) 89°. (Scale bar: 50 μm.)

)telecentric configuration. This scheme therefore allows angle-dependent engineering of the metasurface phase profile to suppress aberrations. The physical aperture reduces the spherical aberration compared to the virtue aperture of the singlet metalens with quadratic phase profile. Compared to metalens doublet and other non-intuitive nonlocal and multi-aperture design concepts, it features reduced computational load, and easier device fabrication and integration.

Following the architecture, we derived an analytical design approach for flat (metasurface or diffractive) fisheye lenses capable of imaging over near-180° FOV. We demonstrate that lenses designed using this scheme can achieve nearly diffraction-limited performance across the entire FOV while maintaining high focusing efficiencies above 65%. This design approach not only sheds light on the key design trade-offs of the WFOV lens, but is also poised to supersede the traditional iterative design scheme.

Through the utilization of the analytical solution, we reported the design and experimental demonstration of metalenses operating at the LWIR band with an ultra-wide FOV of 140°. The analytical model was also used to rationally guide the lens spacer material choice. Following the designs, the centimeter-scale metasurfaces were

fabricated on float-zone silicon wafers using large-area photolithographic patterning and optimized DRIE protocols. Experimental characterization of the metalenses validated our theoretical design and demonstrated unfiltered thermal imaging using a metalens-integrated infrared camera. Benefitting from its simple architecture, scalable fabrication process, and exceptional wide-FOV imaging capability, the WFOV metalens technology potentially offers an appealing alternative to existing LWIR compound lens optics.

We then demonstrate that the combination of direct search optimization and deep learning meta-atom generation networks present a generic and computationally efficient scheme for objective-driven design of metasurface optics. We show that meta-optics designed using the scheme offer enhanced performances over their MDL counterparts exploiting the diverse dispersion characteristics of the free-form meta-atoms that form the metasurface. We further applied the scheme to develop the first broadband and wide field-of-view metalens design.

Finally, we substitute the front aperture with an EDOF metasurface of cubic phase profile, the EDOF + WFOV metalens doublet configuration shows depth-invariant PSF over the 3 - 10 mm object range and near-180° FOV. Information of the original object can be retrieved through the deconvolution between captured image and EDOF PSF.

The design concept discussed in this chapter offers large degree-of-freedom to accommodate different application requirements through the modification of both the front aperture and the back metasurface. For example, the achromatic WFOV metalens use non-intuitive meta-atoms on the back metasurface to accommodate the dispersion requirement, whereas the EDOF WFOV metalens substitutes the front aperture with an EDOF metasurface to include the EDOF feature.

For decades, WFOV optics have been synonymous with bulky and complicated multi-lens assembly. The advent of metasurfaces is set to transform the field, enabling flat WFOV lenses that are compact and light-weight while offering exceptional optical quality with drastically reduced element count. WFOV imaging and sensing therefore also epitomize an emerging area where optical metasurface technologies are most

likely to make significant practical impacts. In light of the growing importance of this dynamic field, this chapter presented an overview of the proposed WFOV metalens designs, analyzed the intrinsic performance trade-offs of various WFOV metalens configurational parameters, and spotlighted promising applications of WFOV metalens technologies. To conclude, we foresee that exciting applications will come to fruition in this wide-open space as we embrace imminent new developments and innovations of WFOV metalens technologies over the next few years.

Chapter 4

Metalens for 3-D depth sensing

4.1 Introduction of 3-D depth sensing

3D depth sensing refers to the capability of a system or device to accurately perceive and measure the distance or depth information of objects in a three-dimensional space. It allows for the creation of depth maps, which represents the spatial layout of the scene.

Depth sensing has become increasingly important in various fields, including computer vision, robotics, augmented reality, autonomous vehicles, gaming, and more. It enables applications such as gesture recognition, object tracking, 3D scanning, immersive experiences, and accurate spatial mapping.

Various technologies for 3-D depth sensing have been proposed, they are generally divided into two different strategies: the passive depth sensing and active depth sensing. Passive depth sensing refers to the process of capturing depth information without actively projecting any signals onto the scene. It relies on analyzing existing light or image data to infer depth. On the other side, active depth sensing involves the use of active illumination or projection of signals onto the scene to measure and capture depth information. The conventional 3-D depth sensing systems require the stacking of multiple refractive optical components, and therefore can be substituted with metasurfaces to simplify the architectures and reduce the element count. Moreover, metasurfaces provide improved image quality and arbitrary wavefront encoding

capability, which can be utilized to improve the depth sensing accuracy as we will discuss in detail in the following sections.

Passive depth sensing techniques include stereoscopic imaging and PSF engineering. Stereoscopic Imaging uses two or more cameras to capture images from different viewpoints, and depth information can be extracted by comparing the disparities between the images. PSF engineering involves encoding wavefront coding term in the lens phase profile, and analyze the depth information from the depth-dependent PSF through image deconvolution. Stereoscopic imaging will be discussed in Section 4.2, and PSF engineering will be discussed in Section 5.2.

Active depth sensing techniques include structured light projection and beam steering. Compared to passive depth sensing techniques, active sensing techniques usually have higher depth measurement accuracy at the sacrifice of introducing extra active optical components and higher power consumption. Structured light projection involves projecting a carefully designed pattern of light onto the subject and analyzing the deformation or displacement of the pattern to determine depth. Beam steering is a crucial aspect of Light Detection and Ranging (LiDAR) systems used for 3D depth sensing. LiDAR technology uses lasers to measure distances and create high-resolution 3D maps of the surrounding environment. Beam steering allows LiDAR systems to scan the environment by directing laser beams in different directions to gather depth information. These techniques will be discussed in Section 4.3.

4.2 Passive depth sensing using wide field-of-view stereo metalenses

Conventional stereoscopic imaging techniques involves the utilization of two identical refractive lenses, and integrate them side by side to construct the stereoscopic camera module. Due to the angle-dependent aberration, single-layer refractive lens has limited FOV, which therefore also restricts the FOV of the sensing module. On the other side, by utilizing the single-layer fisheye metalens mentioned in the previous

chapter, depth mapping with an unprecedented FOV of 170° FOV can be achieved.

The 3-D sensor module comprises a pair of juxtaposed fisheye cameras, each equipped with a wide FOV metalens operating at 670 nm wavelength. The architecture of the lens along with ray trace simulation results for light impinging at different incident angles are depicted in Fig. 4-1a. The front aperture has a diameter of 1 mm and was patterned by lift-off of evaporated Sn metal on a fused silica substrate. The metalens is made of PECVD amorphous silicon deposited on a second fused silica substrate. The metasurface pattern was composed of cylindrical pillars with a period of 320 nm, height of 464 nm, and diameters varying from 110 nm to 170 nm to provide full 2π phase delay coverage. The metasurface patterning was accomplished by electron beam lithography followed by deep reactive ion etching. Fig. 4-1b shows excellent pattern fidelity of the nanopillars. The two substrates are subsequently aligned and bonded together via optical adhesives to form a monolithic element with a target thickness of 3 mm (Fig. 4-1c). The architecture allows incident light from different angles to interact with different and yet continuous portions of the metasurface. We have shown that with an analytical derived metasurface phase profile, diffraction-limited focusing onto a flat image plane can be achieved in the last chapter.

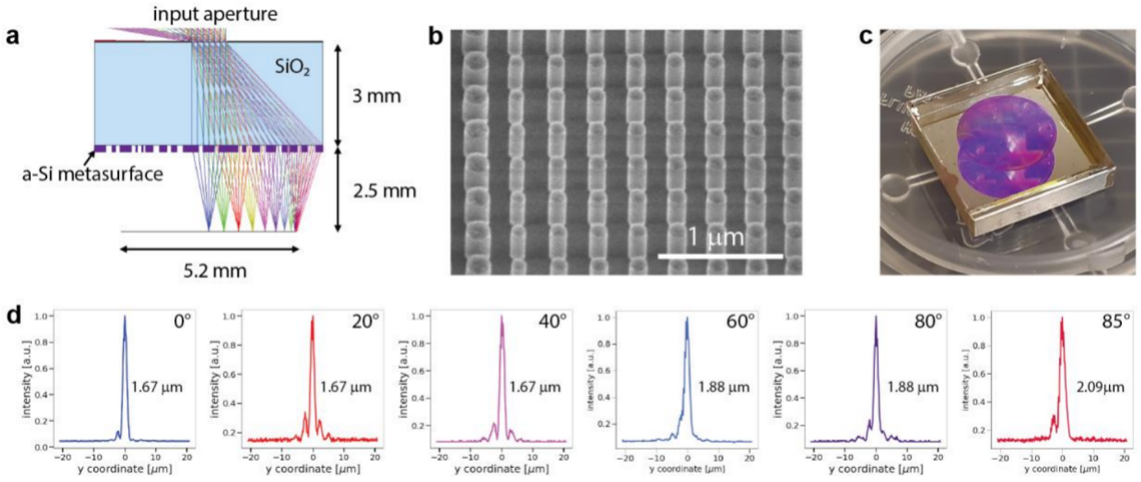

Figure 4-1: Fisheye metalens design and characterization. (a) Layout and ray trace modeling of the fisheye metalens. (b) SEM image detailing the circular a-Si pillar pattern with excellent fidelity. (c) Snapshot of a fabricated metalens. (d) Measured focal spot profiles for angles of incidence varying from 0° to 85° with the corresponding FWHM values.

Focusing performance of the metalens was characterized by mounting a laser on a circular rail while capturing the focal spot profile via a microscope (for focal spot characterization) or a detector integrated with a 200 μm pinhole (for efficiency measurement). We measured its point spread function (PSF) for a range of angles of incidence (Fig. 4-1d), showing formation of sharp focal spots across the entire 170° FOV. The focusing efficiency, defined as the fraction of optical power collected by the pinhole detector normalized over the power incident on the metasurface, varies from 70% at normal incidence to 60% at large incident angles.

The metalenses were then attached to off-the-shelf CMOS imager sensors (Arducam 10MP MT9J001, 3664 ×2748 pixels with a pixel pitch of 1.67 μm) using home-built mechanical housings fabricated via precision computer numerical control machining and 3D printing (Figs. 4-2a and 4-2b). A red LED lamp with a center wavelength of 660 nm was used as the illumination source. Figs. 4-2c and 4-2d present images taken by the two juxtaposed metasurface cameras, showing excellent resolution despite the presence of chromatic aberration due to spectral width and center wavelength offset of the illumination source. The images exhibit clear barrel distortion, which is characteristic of fisheye imaging systems and was corrected using camera calibration and distortion-correction algorithms in image post-processing. A standard disparity-based approach was applied to the undistorted images to retrieve the depth map (Fig. 4-2e).

4.3 Active depth sensing with structured light projection and beam steering

Active depth sensing refers to the process of measuring the object distance by actively emitting a light source and analyzing the reflected or scattered light, such as time-of-flight(ToF) and structured light(SL)[12, 45, 53, 55, 242–246]. ToF technique involves scanning the laser beam across a wide field-of-view(FOV), and measure the time delay of the backscattered beam. On the contrary, SL technique involves projecting the 2-

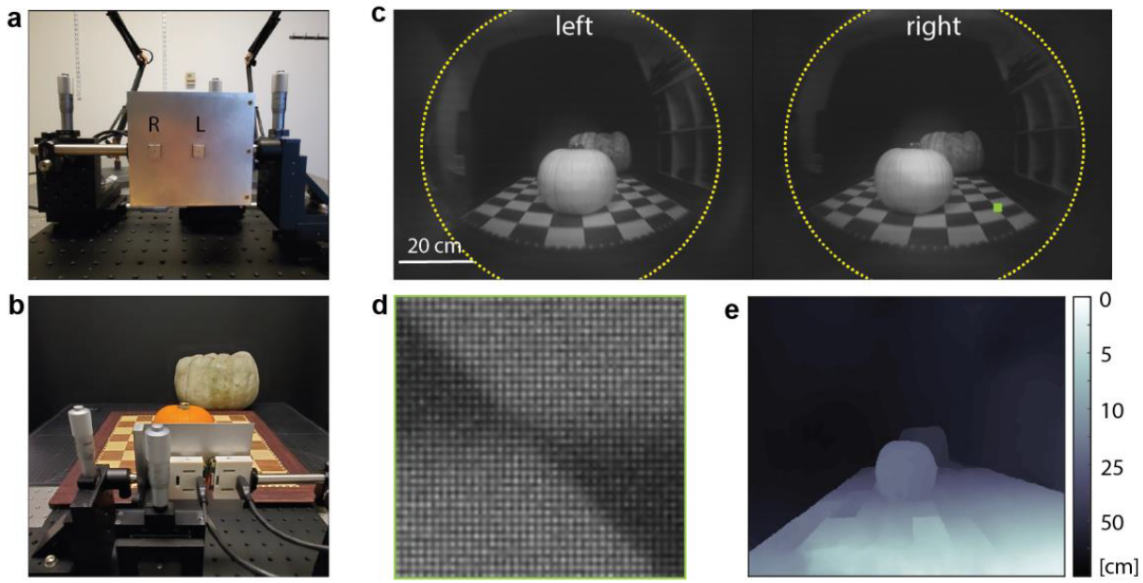

Figure 4-2: Wide FOV stereoscopic depth imaging demonstration. Photographs showing (a) front and (b) back of the experimental setup. (c) Panoramic images of the objects (a large white jarranhdale and a small orange 'sugar-pie' pumpkin) taken by the two juxtaposed fisheye cameras. (d) Magnified pitch of the captured image (green square in the right figure (c)) depicting pixel-level resolution. (e) Depth map retrieved from the disparities of the left and right camera images after distortion correction.

D light patterns onto the objects through the high density dot projection system, and measuring the distortion of the backscattered pattern. Though differ in the mechanism and the depth calculation algorithm, they all involve the projection of the laser beam into a large angular space.

Conventional structured light projectors use diffractive optical elements (DOEs) or spatial light modulators (SLMs) to project the structured patterns, and the phase or amplitude profiles of the optical elements are optimized through the numerical algorithms[247–250]. Recently, metasurfaces have been introduced to serve as the phase mask of the structured light projector[12, 53, 55, 242]. The wavefront of the light is modulated through the arrangement of sub-wavelength nanostructures[251–259]. Compared to DOEs, they feature higher efficiency and improved uniformity of the projected beams due to the sub-wavelength resolution. To further improve the integration of the system, the single laser beam illuminating the optical components can be replaced with vertical cavity surface-emitting laser (VCSEL) array, and therefore

on-chip integration and high power density can be achieved simultaneously[54, 260].

On the other side, conventional ToF techniques steer the beam through the rotating mirrors or the microelectromechanical systems (MEMS)[261–270]. However, they feature bulky components, limited response time, high power consumption, and restricted scanning range. Chip scale beam steering has been demonstrated to replace the conventional mechanical scanners[45], which however still limited by the scanning FOV. Lens-assisted beam steering (LABS) provides an alternative approach to achieve WFOV scanning range by combining waveguide switches with refractive lens or metasurface[47, 48, 271–276]. Recently, further improvement has been realized through the integration of metasurfaces with VCSEL array[46, 277].

In both cases, the design of the DOEs or metasurfaces was accomplished through the iterative numerical optimization of the amplitude and phase profiles, which is computationally intensive. Moreover, the projected pattern exhibits distortion at large bending angles, and therefore restricts the resolution of the large FOV applications. In this thesis, we derive an analytical solution to the optimum phase profile of the metasurface for the beam steering and structured light projection with VCSEL array integration. We show that, when using a single layer metasurface and assuming small beam size, the optimum design adopts a quadratic phase profile. We then mathematically prove that by using metasurface doublet, the projection angle with object height relationship can be customized at will. Following this derivation, we further propose the optimum metasurface doublet configuration to correct the distortion of the projected pattern, and demonstrate the trade-off between distortion and aberration of the projected beams.

4.3.1 Single-layer metasurface dot projector

In essence, metasurface-assisted beam steering and pattern projection are functionally identical in that both transform light emanating from a light source array into a set of free-space optical beams. The baseline configuration of an optical projection module is depicted in Fig. 4-3. Light emitted from each single source (henceforth referred to as a pixel) is mapped into an optical beam in the angular space by the projection

meta-optics, where the beam propagation direction is defined by the location of the pixel. The projection optics can contain either a single layer metasurface pattern, or cascaded multiple metasurfaces (e.g., a doublet with two layers of metasurfaces) for advanced functions, as we will show later. The main design task is therefore to identify suitable optical phase profiles of the projection meta-optics to ensure optimal beam quality over the field-of-view (FOV). The phase profiles of metasurfaces used in these applications have so far been designed entirely through numerical optimization[12, 53, 247, 260], which not only adds to the computational overhead but also shed little physical insight on the design parameter choices.

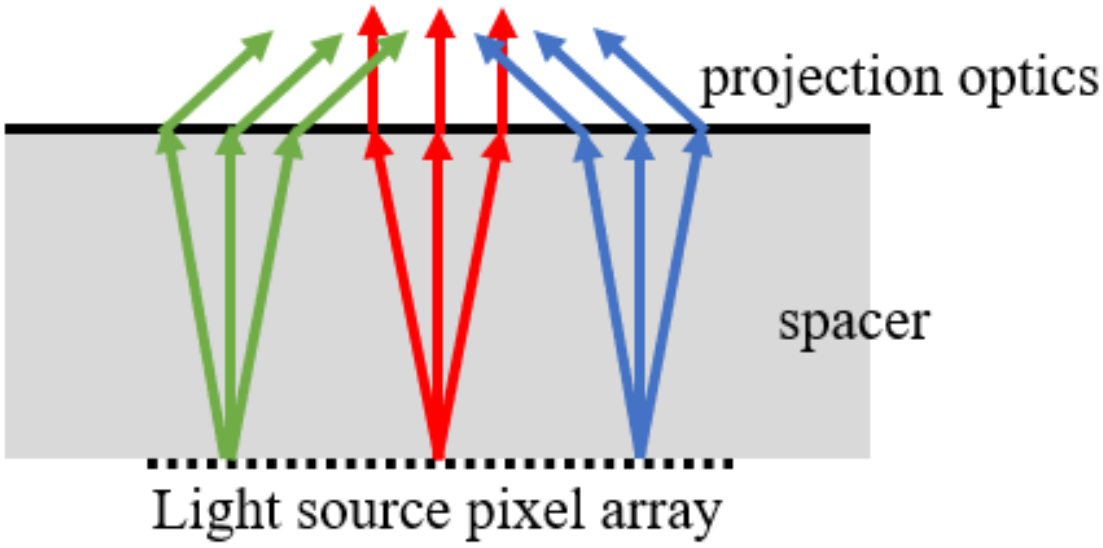

Figure 4-3: Schematic illustration of singlet metasurface projector design.

We start by clarifying the assumptions made in our theoretical derivation. Firstly, our model is derived for a single operation wavelength. For projection modules using light sources with a non-negligible spectral bandwidth (e.g. LEDs), the same analytical phase profile solution holds for each and every wavelength. Fulfilling the phase functions at different wavelengths necessitates dispersion engineering of the metasurface which has been extensively discussed in literature[278, 279]. Secondly, each single source or pixel is assumed to be a point source. This is in general an accurate approximation as the output aperture size of VCSELs or micro-LEDs used in the

projection module is typically in the range of a few micrometers to tens of micrometers, which is far smaller compared to the dimensions of the metasurfaces. Thirdly, in our initial analytical model we assume that the divergence angle of the light cone emitted from the sources is small. For light sources relevant to practical applications (e.g., VCSEL arrays employed in structured light projectors), the divergence angle is as small as 10° - 20°, and the approximation minimally impacts the performance of metasurface optics designed using our analytical approach. For cases where the small divergence angle approximation becomes inaccurate, the analytical design derived under the assumption still serves as an excellent heuristic solution that not only dramatically simplifies further numerical refinement but also guarantees convergence upon the globally optimal design, as we shall show later.

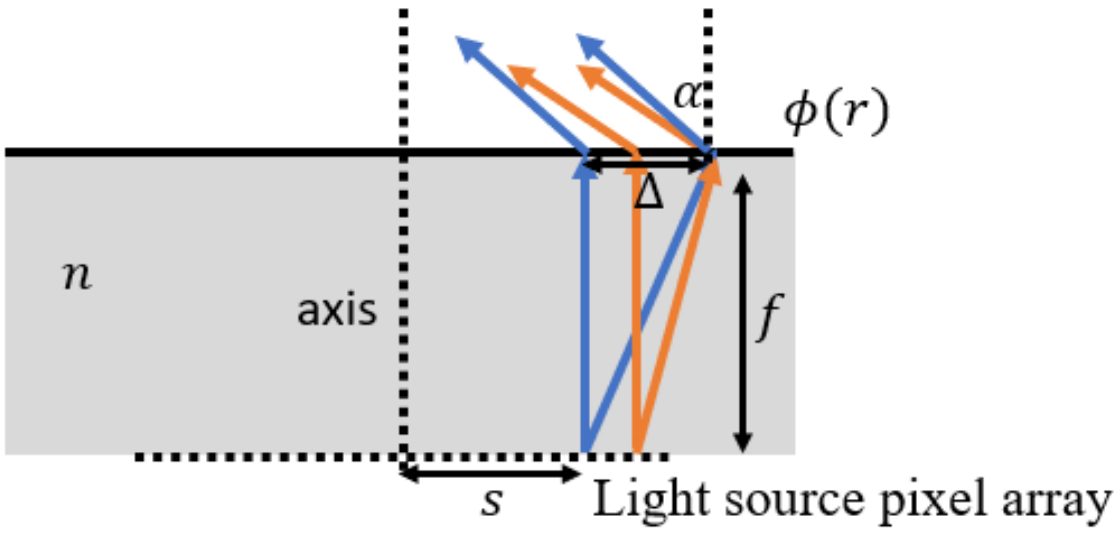

Figure 4-4: Illustration of the singlet metasurface projector phase profile derivation.

The optimum phase profile of the metasurface will be derived following the schematic shown in Fig. 4-4. The pencils of rays originating from the pixel are transformed into parallel rays after propagating through the metasurface. We first consider rays near the center of the emitting cone of the light source, which illuminate the metasurface in the surface-normal direction. In this case, the optical path lengths (OPLs) of the rays inside the spacer are identical to the first order approximation, and the metasurface

locally acts as a grating to diffract the beam to a certain direction. Therefore, the phase gradient of the metasurface follows Eq. 4.1:

$$\frac{d\phi(s)}{ds} = -\left(\frac{2\pi}{\lambda}\right) \cdot sin[\alpha(s)] \tag{4.1}$$

Here, s is the distance of the pixel to the center of the metasurface, $\phi(s)$ is the phase profile of the metasurface, λ is the wavelength of the light source, and $\alpha = \alpha(s)$ is the projection angle of the beam which depends on the pixel position (i.e., object height). To determine this relationship, we now consider the configuration depicted in Fig. 4-4, where two sets of rays coming from two neighboring pixels are analyzed. The two rays denoted as blue lines are coming from the center and edge of the first pixel's emission cone, which are separated by a distance Δ when arriving at the metasurface. Since light emitted from each pixel is collimated by the metasurface to form parallel rays, the OPL difference between the two blue rays must be compensated by the metasurface, which yields:

$$\phi(s+\Delta) - \phi(s) = -\left(\frac{2\pi}{\lambda}\right) \cdot n \cdot \left(\sqrt{f^2 + \Delta^2} - f\right) - \left(\frac{2\pi}{\lambda}\right) \cdot sin\left(\alpha(s)\right) \cdot \Delta \tag{4.2}$$

In the equation, n is the refractive index of the spacer separating the metasurface from the light source array and f is the thickness of the spacer. We then consider two rays coming from the neighboring pixel (represented as orange lines), with a distance of $s+\delta s$ away from the center of the metasurface. One of them comes from the center of the neighboring pixel's emission cone, and the other arrives at the same position on the metasurface as the edge ray from the center pixel (i.e., the slanted blue line). The two rays must become parallel after passing through the metasurface. The condition reduces to:

$$\phi(s+\Delta) - \phi(s+\delta s) = -\left(\frac{2\pi}{\lambda}\right) \cdot n \cdot \left(\sqrt{f^2 + (\Delta - \delta s)^2} - f\right) - \left(\frac{2\pi}{\lambda}\right) \cdot sin(\alpha((s+\delta s))) \cdot (\Delta - \delta s) \tag{4.3}$$

By subtracting Eq. 4.2 from Eq. 4.3 and applying Eq. 4.1, we have the relationship between the pixel position s and the beam projection angle α:

$$sin(\alpha) = \frac{n \cdot s}{\sqrt{f^2 + \Delta^2}} \tag{4.4}$$

We note that Eq. 4.4 depends on Δ. Therefore Eq. 4.4 cannot be rigorously satisfied for rays emitted at different angles. In the limit of a small divergence angle such that $\Delta \ll f$, Eq. 4.4 simplifies to:

$$sin(\alpha) = \frac{n \cdot s}{f} \tag{4.5}$$

Substituting Eq. 4.5 into Eq. 4.1 reveals the optimum phase profile of the metasurface in the small divergence limit:

$$\phi(s) = -\left(\frac{2\pi}{\lambda}\right) \cdot \frac{n \cdot s^2}{2f} \tag{4.6}$$

We see that the phase profile assumes a quadratic form. Interestingly, the quadratic phase function has also been implemented to realize wide FOV metalenses for imaging and sensing applications [41–43, 148, 149, 280]. While it may be tempting to suggest that the beam projection design is equivalent to a quadratic-phase imaging metalens considering optical reciprocity, there is one important difference. In an imaging metalens, the spatial extent of the incident beam is truncated by a virtual aperture. In the projection optics, the beam size is defined by the divergence of the light source and is generally much smaller than the virtual aperture (which spans an apex angle of 90° [36]). Spherical aberration inherent to the quadratic phase[70] thus has a significantly diminished impact on beam forming quality from the projection meta-optics. As we demonstrate next, the single-layer metasurface projection optics can readily attain diffraction-limited performance, which is not possible for the imaging lenses.

In the following, we present a design example capable of diffraction-limited wide-FOV (140°) beam steering or optical projection with realistic device parameters. The light sources consist of a VCSEL array at 940 nm wavelength with a total diameter of 780 μm, and a metasurface with a diameter of 930 μm. They are separated by

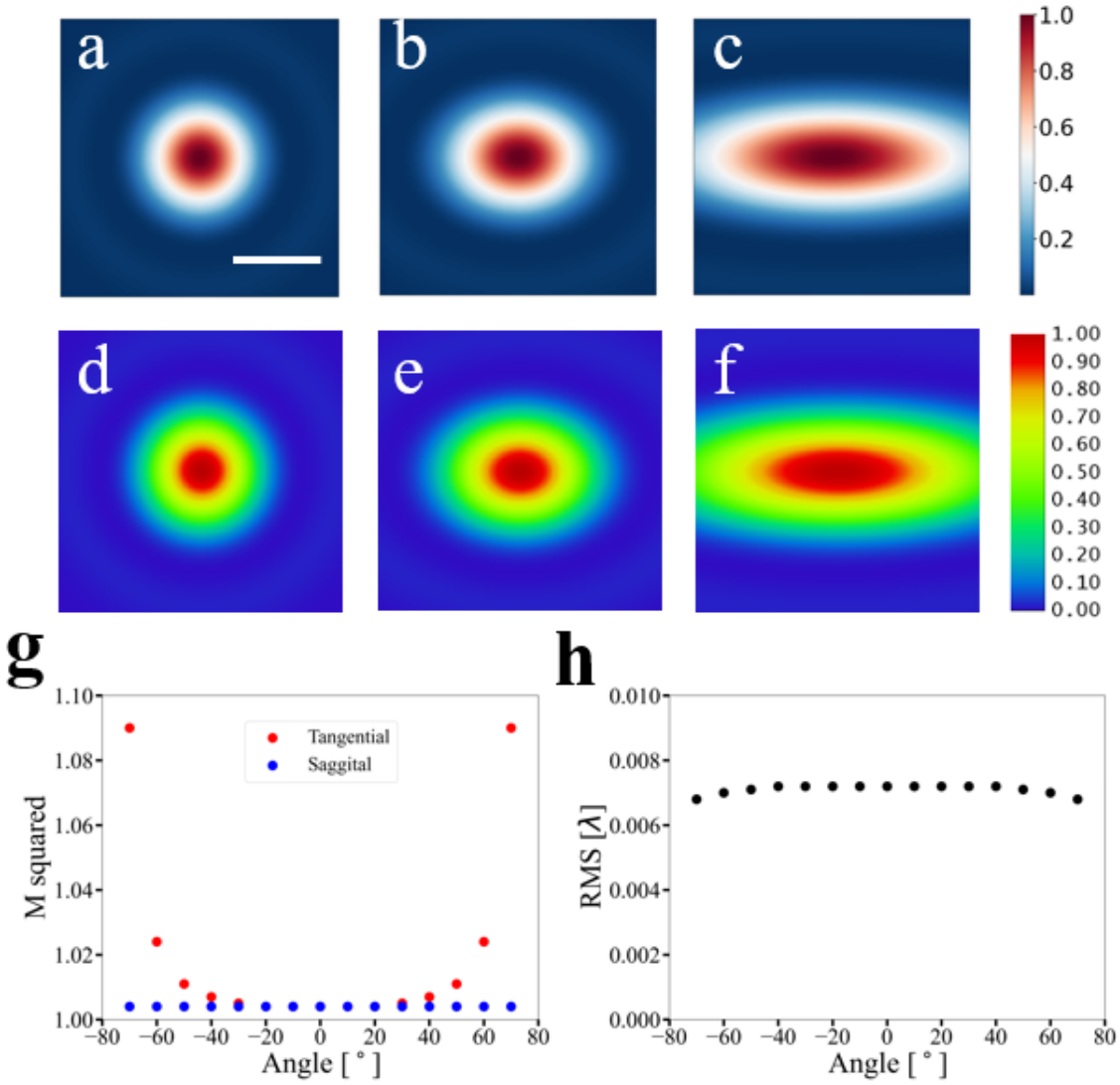

Figure 4-5: Simulated performance of a single-layer metasurface optical projector. (a)-(c) PSFs at projection angles of (a) 0°, (b) 40°, and (c) 70° modeled using diffraction integral. (Scale bar: 0.4°) (d)-(f) PSFs at projection angles of (d) 0°, (e) 40°, and (f) 70° calculated with OpticStudio. (g) M^2 and (h) RMS wavefront error (given in free-space wavelength λ) as functions of projection angle.

a SiO_2 glass spacer with a thickness of 600 μm and a refractive index of 1.45. We assume that the divergence angle of the VCSEL (defined as the apex angle of its emission cone in air) to be 20° consistent with commercial off-the-shelf VCSEL array specifications. The point-spread-functions (PSFs) in the angular space at different projection angles across the 140° FOV were simulated using two methods: the Kirchhoff diffraction integral following previously established procedures [71, 214], and with the commercial software package OpticStudio. The results are displayed in Figs. 4-5 a-f, showing excellent agreement between the two methods. We further simulated the M^2 parameter and the root-mean-square (RMS) wavefront error as functions of projection angle, which are shown in Figs. 4-5g-h. The near-unity M^2 values suggest that the projection optics achieve diffraction-limited performance with minimal wavefront distortion throughout the entire 140° FOV.

The projection optics design maps the VCSEL array pattern shown in Fig. 4-6a (with a VCSEL spacing of 40 μm) into a projected beam pattern shown in Fig. 4-6b in the angular space. Pincushion distortion is apparent towards the edge of the FOV where the angular spacing of the projected beam spots increases with the projection angle. The distortion is dictated by Eq. 4.4, which specifies that the pixel position relates to the projection angle following a sine function. We show in the following section that such distortion can be corrected using a doublet meta-optic, and an analytical design formalism is provided for the doublet projector design.

4.3.2 Metasurface doublet dot projector for distortion correction

In this sections, we demonstrate that a two-layer or doublet metasurface projector offers additional design degrees of freedom to tailor the pixel position-beam angle relation at will.

The doublet projection optics structure is schematically illustrated in Fig. 4-7a, where two layers of metasurfaces, MS-1 and MS-2, are separated by a substrate. Here we take the substrate as having the same refractive index as the spacer between MS-2

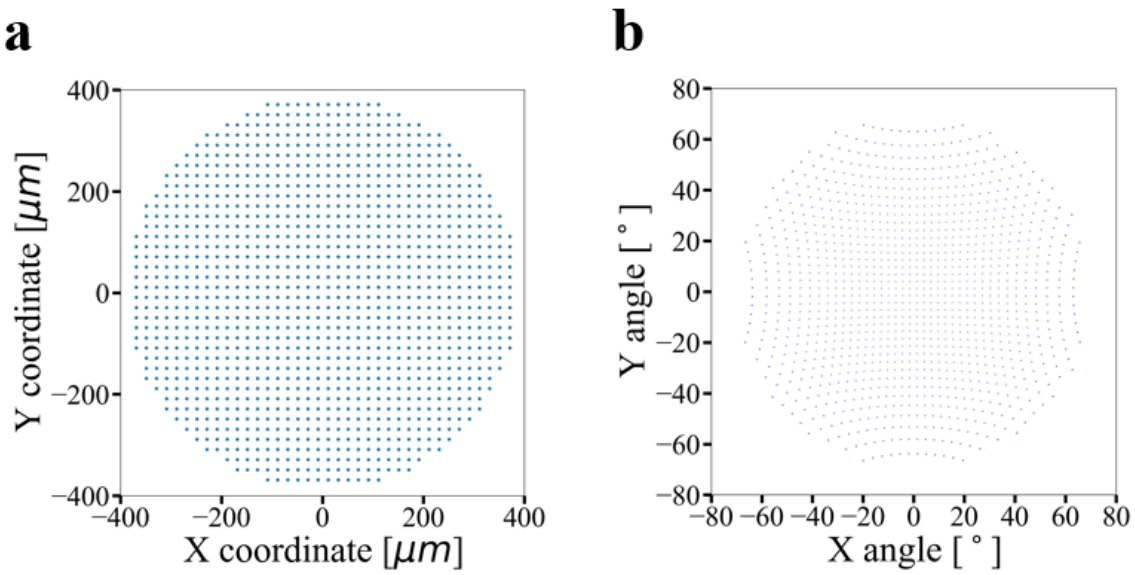

Figure 4-6: Illustration of structured light projection using singlet metasurface. (a) VCSEL array arrangement. (b) Projected pattern.

and the light source pixel array, although the analysis is generic and can be readily extended to the case where the two materials are different. Laser beams from the light source array are diffracted by the two metasurfaces sequentially, and projected to different directions. Here we consider a light ray emitting from a pixel with distance s to the center of the metasurface, which adopts an exit angle of θ with respect to surface normal inside the spacer. The ray trajectory is schematically illustrated in Fig. 4-7b. The projection angle α can be expressed in terms of s, θ, and the phase profiles of the two metasurfaces $\phi_1(r)$ and $\phi_2(r)$ as:

$$\alpha(s, \theta, \phi_1, \phi_2) = arcsin\left[nsin\gamma - \left(\frac{\lambda}{2\pi}\right)\phi_1'(r_1)\right] \tag{4.7}$$

$$r_1 = r_2 - L_1 tan\gamma \tag{4.8}$$

$$r_2 = s - L_2 tan\theta \tag{4.9}$$

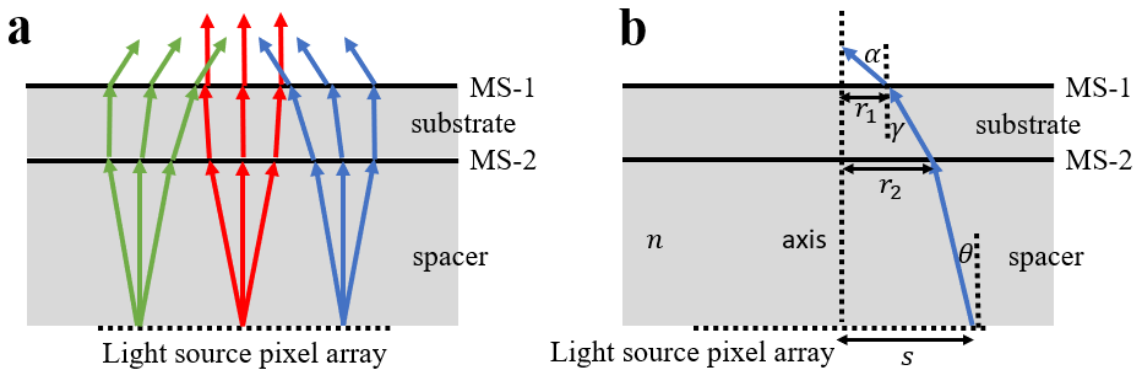

Figure 4-7: Schematic illustration of doublet metasurface projection optics design. (a) Schematic of the projector configuration. (b) Illustration of the ray trajectory under consideration.

$$\gamma = arcsin\left[sin\theta - \frac{1}{n}\cdot\frac{\lambda}{2\pi}\phi_2'(r_2)\right] \tag{4.10}$$

where L_1 and L_2 are the thicknesses of the substrate and the spacer, respectively. Similarly, the OPL of the ray L can be written in terms of the same four parameters:

$$L(s,\theta,\phi_1,\phi_2) = n\cdot\frac{L_2}{cos\theta} + n\cdot\frac{L_1}{cos\gamma} + r_1 sin\alpha + \left(\frac{\lambda}{2\pi}\right)\cdot[\phi_1(r_1)+\phi_2(r_2)] \tag{4.11}$$

In order to minimize wavefront error of the projected beam, the OPL of different rays emitted from the same pixel should be identical, which is equivalent to L being stationary as θ changes. We therefore set the first two orders of derivatives of L with respect to θ to be zero:

$$\frac{\partial L}{\partial\theta}_{\theta=0} = 0 \tag{4.12}$$

$$\frac{\partial^2 L}{\partial\theta^2}_{\theta=0} = 0 \tag{4.13}$$

Here, we again assume a small divergence angle of the light cone from the source, so we only need to solve Eq. 4.12 and Eq. 4.13 when $\theta = 0$, i.e., at normal incidence. The two equations contain three parameters s, ϕ_1, and ϕ_2, and therefore the system

can accommodate one more constraint to uniquely define the phase profiles of the two metasurfaces. We present three possible options below as the additional constraint in Eqs. 4.14-4.16, respectively.

In the case of a singlet metasurface, the third constraint can be written as:

$$\phi_2 = 0 \tag{4.14}$$

Combining Eqs. 4.12-4.14, the same quadratic phase of the first metasurface can be derived as before.

To further suppress the wavefront error and aberration, the third order derivative of L with respect to θ can be set to zero:

$$\frac{\partial^3 L}{\partial \theta^3}_{\theta=0} = 0 \tag{4.15}$$

In this case, the optimum phase profiles of the doublet metasurfaces can be derived by combing Eqs. 4.12, 4.13, and 4.15 to nullify the third order wavefront error terms.

Finally, a custom pixel position-projection angle relation can be added as the constraint to enable on-demand distortion compensation. A simple example is a linear relationship between the pixel position and the beam projection angle:

$$\alpha = c \cdot s \tag{4.16}$$

where c is a constant. Combining Eqs. 4.12, 4.13, and 4.16 uniquely specifies the doublet metasurface phase profiles.

Eqs. 4.12-4.13 contain the first order derivatives of ϕ_1 and ϕ_2 (phase gradients of the metasurfaces), and the derivatives of θ up to the second order. Thus, it is not possible to obtain explicit solutions of the doublet phase profiles. We instead developed an algorithm to solve the equations numerically.

The projector structure under investigation is shown in Fig. 4-8. We consider the chief ray emitted from a pixel, which intersects with the two metasurfaces (MS-1 and MS-2) at distances of r_1 and r_2 from the optical axis. Assuming that the phase functions ϕ_1 and ϕ_2 of the two metasurfaces as well as their gradients ϕ_1' and ϕ_2' are

known at r_1 and r_2, the iterative algorithm can then solve the values of these quantities at new positions $r_1 + \delta r_1$ and $r_2 + \delta r_2$. The entire phase profiles are determined by repeating the iterative steps.

To do so, we consider a slightly off-axis ray emitted from the same pixel with an emission angle $\theta \to 0$. Its projection angle is determined by the phase gradient of the metasurfaces at the new intersection positions $r_1 + \delta r_1$ and $r_2 + \delta r_2$:

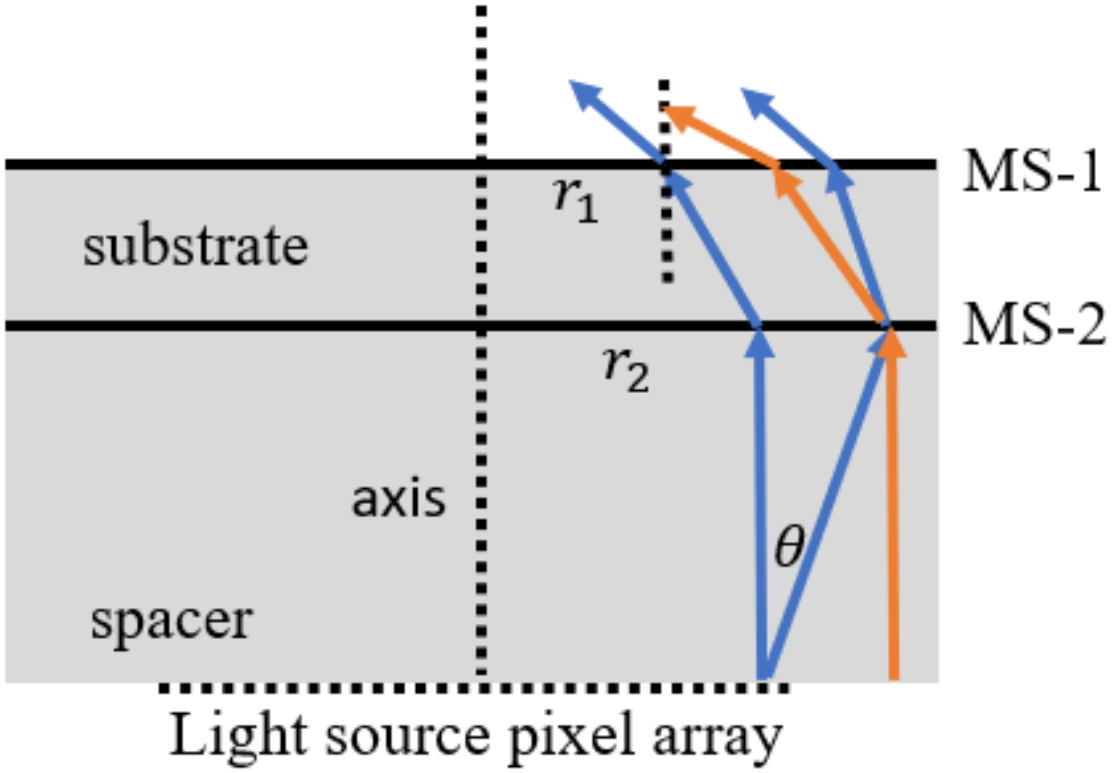

Figure 4-8: Configuration for iterative solution of doublet metasurfaces phase profiles.

$$\alpha(s) = \alpha(\phi_1'(r_1 + \delta r_1), \phi_2'(r_2 + \delta r_2)) \tag{4.17}$$

One can reference Eqs. 4.7-4.10 regarding the complete form of Eq. 4.17. We note that Eq. 4.17 is an alternative expression of Eq. 4.12. Next we look at the chief ray from the neighboring pixel, which intersects MS-2 at the same position $r_2 + \delta r_2$ as the off-axis ray from the first pixel. Its projection angle can be written as:

$$\alpha(s+\delta s) = \alpha(\phi_1'(r_1+\Delta r_1), \phi_2'(r_2+\delta r_2)) \tag{4.18}$$

Here Δr_1 represents the distance between the chief ray from the first pixel (the blue rays on the left) and the orange ray on MS-1, which is different from δr_1 (distance between the intersection points of the two blue rays on MS-1). This equation is an alternative form of Eq. 4.13, which we proved in [71]. The phase gradients at the three positions on MS-1 can be related through Eq. 4.19, assuming that the first order derivatives of the phase gradient is constant in the $\theta \to 0$ limit:

$$\frac{\phi_1'(r_1+\delta r_1) - \phi_1'(r_1)}{\delta r_1} = \frac{\phi_1'(r_1+\Delta r_1) - \phi_1'(r_1)}{\Delta r_1} \tag{4.19}$$

Combing Eqs. 4.17-4.19, the phase gradient of the metasurfaces at the new positions $\phi_1'(r_1+\Delta r_1)$ and $\phi_2'(r_2+\delta r_2)$ can be computed.

Using the algorithm, the equations can be solved in a few seconds for metasurfaces sized in the millimeter-scale on a personal computer (e.g., Intel i7-10700 with 8 cores), thereby dramatically reducing the computational load compared to other numerical optimization algorithms[12, 53, 247, 260]. In the following, we apply this approach to further examine the design trade-offs encountered in projection optics with custom distortion profiles.

The structure of the doublet metasurface projection optics under consideration is shown in Fig. 4-9a. The metasurfaces are designed to fulfill a FOV of 120°. The pixel array has a diameter of 870 μm, which emits light with a divergence angle of 20° (apex angle of light cone in air) at 940 nm wavelength. The spacer and the substrate are both made of SiO_2 with a refractive index of 1.45. The substrate between the two metasurfaces is 200 μm thick, and the spacer between MS-2 and pixel array has a thickness of 600 μm. The optimized diameters of MS-1 and MS-2 are 0.98 mm and 0.96 mm, respectively. The optimized phase profiles of the two metasurfaces are plotted in Fig. 4-9b, which are derived using the analytical expressions of Eqs. 4.12, 4.13, and 4.16. The constant c is chosen as:

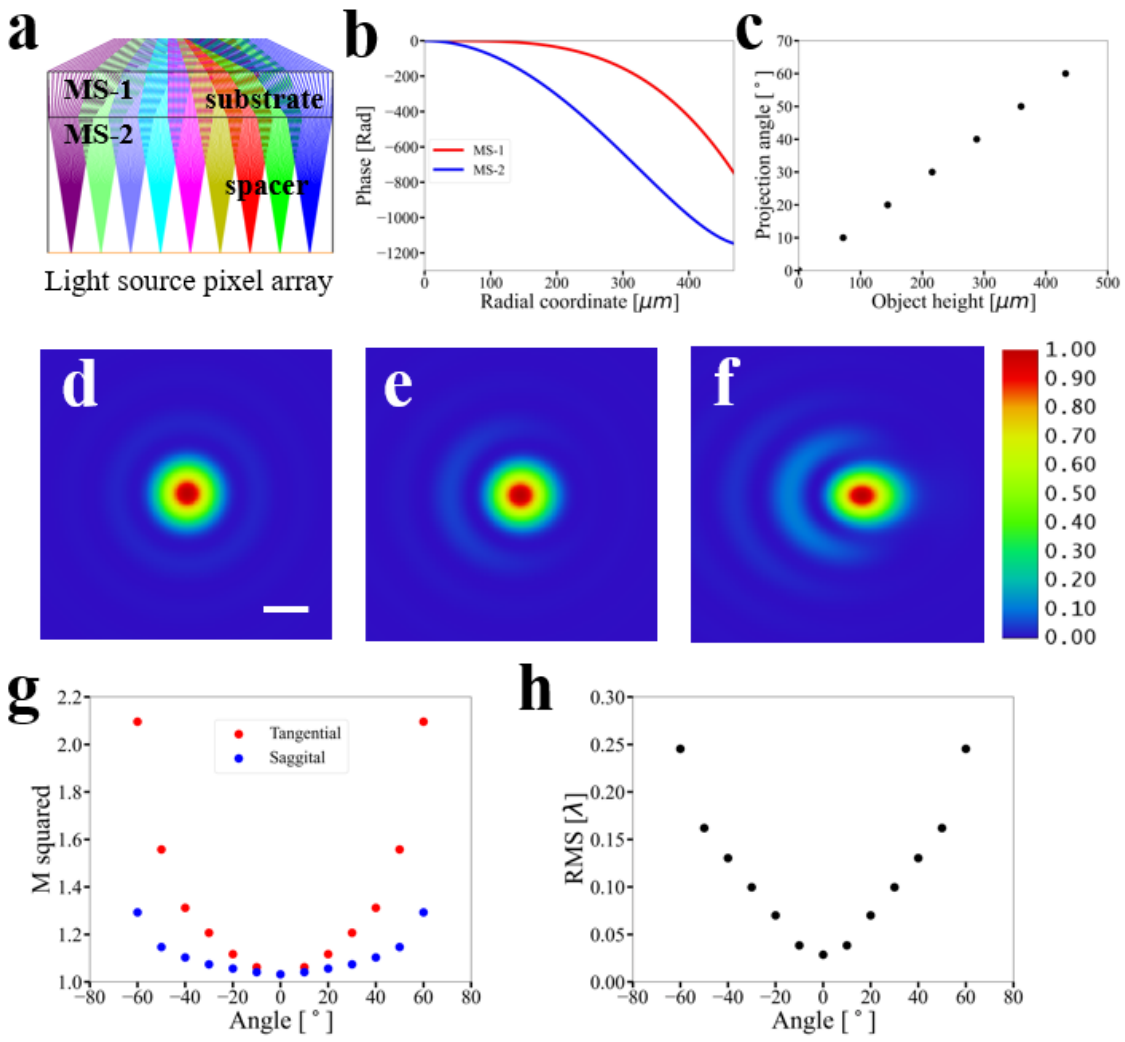

Figure 4-9: Simulated performance of the analytically designed doublet metasurface projector. (a) Configuration of projection meta-optics. (b) Optimized phase profiles of the metasurfaces. (c) Pixel position vs. projection angle. (d)-(f) Simulated angular PSFs at projection angles of (d) 0°, (e) 30°, and (f) 60°. Scale bar: 0.4°. Dependence of the (g) M^2 and (h) RMS wavefront error on the projection angle.

$$c = \frac{n}{L_2} \tag{4.20}$$

where $n = 1.45$ and $L_2 = 600\ \mu m$ are the refractive index and thickness of the spacer. The relationship is identical to that of a spherical lens with a focal length of 600 μm in the paraxial limit. We therefore conclude that MS-2 primarily performs the collimation/projection function, whereas MS-1 serves to correct the spherical aberration, which explains the fact that the phase gradient at the center area of MS-1 is close to zero. We plot the pixel position versus the projection angle in Fig. 4-9c, and the linear relationship validates our distortion-engineering design approach. OpticStudio was used to simulate the angular PSFs of the projected beams, and the results are plotted in Figs. 4-9d-f. Here the phase profiles of the metasurfaces are represented by a series of polynomial terms shown in Tab. 4.1 to facilitate numerical simulation. We further modeled the M^2 and the RMS wavefront error versus the projection angle (Figs. 4-9g-h).

Table 4.1: Polynomial coefficients of the doublet metasurfaces in Fig. 4-9

$A_{1,1}$	$A_{1,2}$	$A_{1,3}$	$A_{1,4}$	$A_{1,5}$	$A_{1,6}$
-8.96	-2.58×10^4	1.18×10^5	-6.52×10^5	2.45×10^6	-6.18×10^6
$A_{1,7}$	$A_{1,8}$	$A_{1,9}$	$A_{1,10}$	$A_{1,11}$	
1.09×10^7	-1.35×10^7	1.11×10^7	-5.35×10^6	1.15×10^6	
$A_{2,1}$	$A_{2,2}$	$A_{2,3}$	$A_{2,4}$	$A_{2,5}$	$A_{2,6}$
-8.12×10^3	1.36×10^4	-8.90×10^4	2.06×10^6	-2.91×10^7	2.60×10^8
$A_{2,7}$	$A_{2,8}$	$A_{2,9}$	$A_{2,10}$	$A_{2,11}$	
-1.48×10^9	5.32×10^9	-1.17×10^{10}	1.41×10^{10}	-7.14×10^9	

We want to point out that a trade-off exists between beam quality, distortion, and FOV. Improved projected beam quality and expanded FOV can be achieved if larger distortion can be tolerated. In the analytically derived design depicted in Fig. 4-9, the increasing aberration at large projection angles is attributed to the breakdown of the small divergence angle assumption. As phase gradient increases with the projection angle, the OPL difference between the chief and marginal rays also increases. To improve the performance of the projection optics at large angles, we further optimized the design numerically by allowing a small deviation from the linear condition Eq.

4.16. The analytically derived phase profiles (Fig. 4-9b) were used as the initial input to numerical optimization. The polynomial terms defining the phase profiles were fine tuned to minimize the sum of M^2 values of the projected beams across the 120° FOV, subject to the constraint that the deviation of the projected chief ray from the linear relationship should be less than 0.1°. The optimized phase profiles are presented in Fig. 4-10a with the corresponding polynomial coefficients listed in Tab. 4.2. We plot the pixel position versus the projection angle of the new design in Fig. 4-10b, which still closely approximates a linear relationship. The simulated PSFs of the projected beams as well as the corresponding M^2 and RMS wavefront error are displayed in Figs. 4-10c-g. Compared to Figs. 4-9d-h, the improved beam quality at large projection angles is evident. The optimized design retains near-diffraction-limited performance across the entire 120° FOV.

Table 4.2: Polynomial coefficients of the doublet metasurfaces in Fig. 4-10

$A_{1,1}$	$A_{1,2}$	$A_{1,3}$	$A_{1,4}$	$A_{1,5}$	$A_{1,6}$
-9.62	-2.58×10^4	1.18×10^5	-6.52×10^5	2.45×10^6	-6.17×10^6
$A_{1,7}$	$A_{1,8}$	$A_{1,9}$	$A_{1,10}$	$A_{1,11}$	
1.09×10^7	-1.35×10^7	1.11×10^7	-5.35×10^6	1.14×10^6	
$A_{2,1}$	$A_{2,2}$	$A_{2,3}$	$A_{2,4}$	$A_{2,5}$	$A_{2,6}$
-8.13×10^3	1.36×10^4	-8.90×10^4	2.06×10^6	-2.91×10^7	2.60×10^8
$A_{2,7}$	$A_{2,8}$	$A_{2,9}$	$A_{2,10}$	$A_{2,11}$	
-1.48×10^9	5.32×10^9	-1.17×10^{10}	1.41×10^{10}	-7.14×10^9	

Finally, using a light source array depicted in Fig. 4-11a with a pixel spacing of 40 μm, we simulated the corresponding projected beam pattern (Fig. 4-11b). Compared to the projection pattern of the single-layer metasurface (Fig. 4-6b), distortion in the angular domain is almost completely eliminated. The beam spot size also increases due to aberration at large projection angles.

4.4 Summary

In summary, we demonstrated metalens architectures for both passive and active depth sensing mechanisms. For passive depth sensing, we positioned two identical

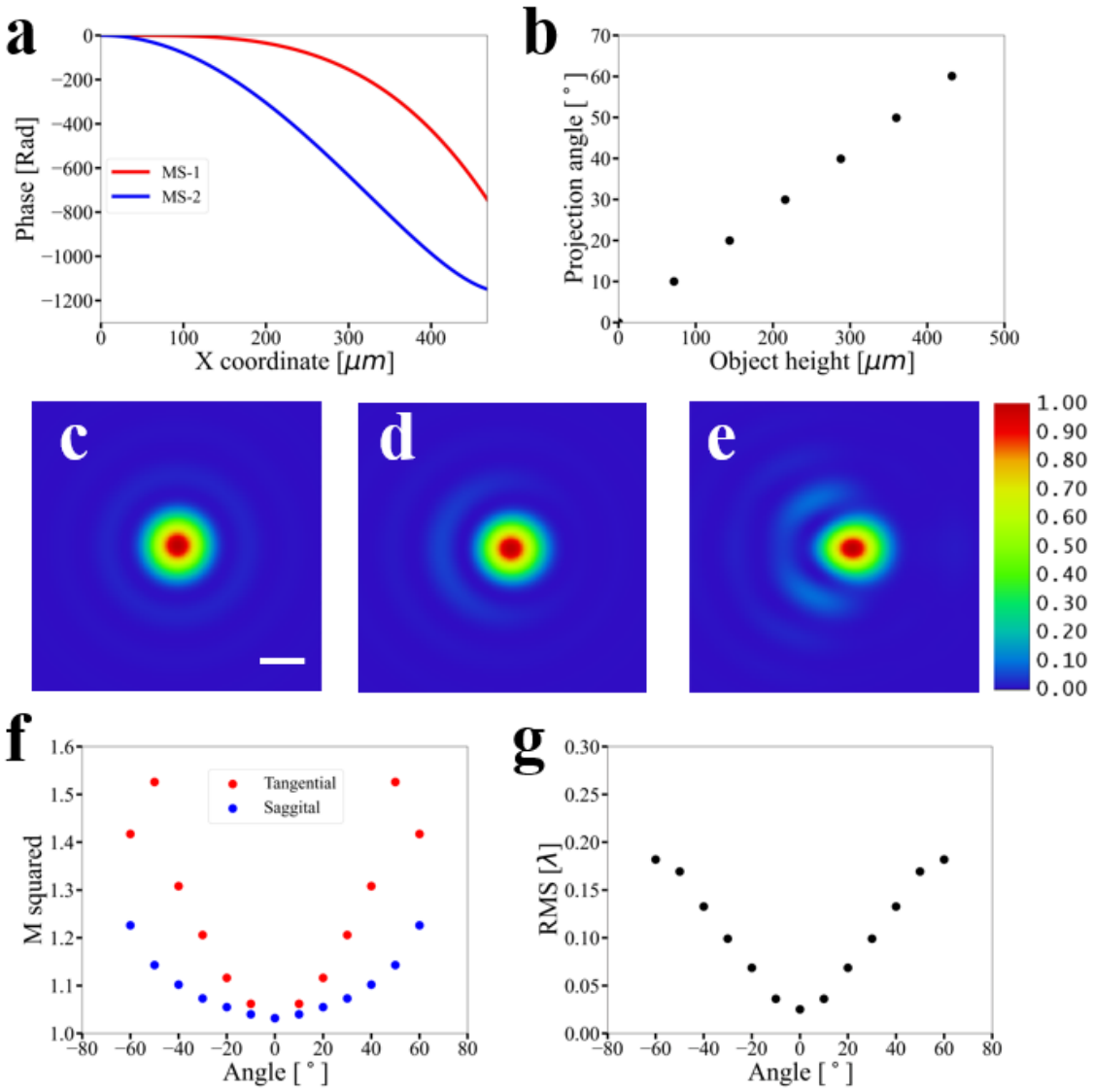

Figure 4-10: Simulated performance of the doublet metasurface projector after numerical refinement. (a) Optimized phase profiles of the metasurfaces. (b) Pixel position vs. projection angle. (c)-(e) Simulated angular PSFs at projection angles of (c) 0°, (d) 30°, and (e) 60°. Scale bar: 0.4°. (f) M^2 and (g) RMS wavefront error versus projection angle.

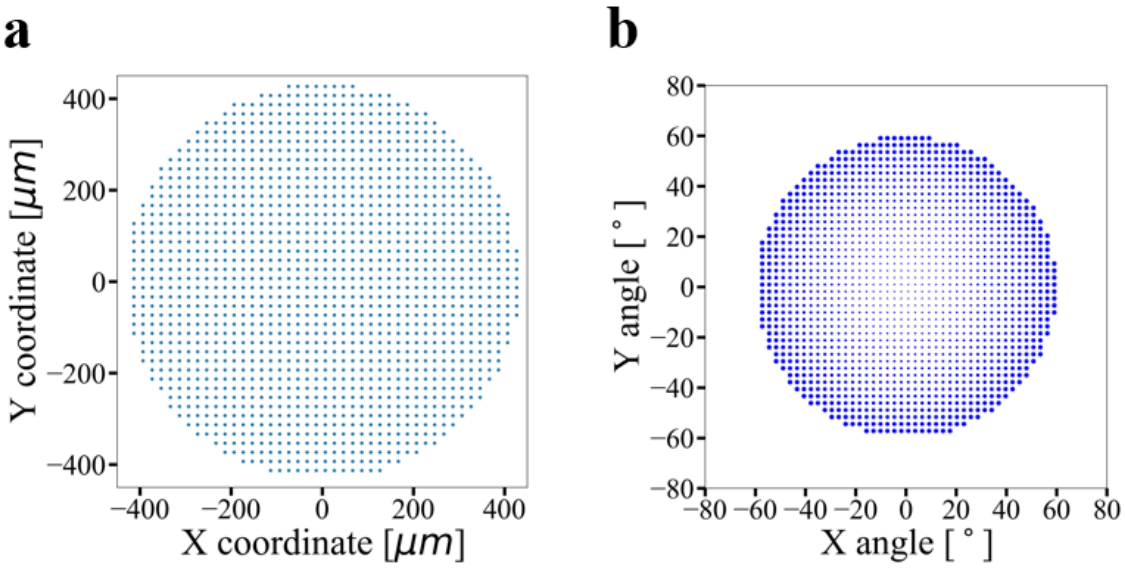

Figure 4-11: Optical projection using the doublet metasurface. (a) Light source array arrangement. (b) Simulated projected pattern in the angular space.

WFOV metalenses working in the 670 nm wavelength and 170° FOV side by side to construct the WFOV stereo camera. The WFOV images taken by the two lenses shift along the horizontal direction, which depends on the distance of the object. Through the image calibration and scene separation, we retrieved the pixel shifts of the objects and obtained the corresponding depth map. Compared to the traditional stereo camera, our metasurface-enabled stereoscopic imaging features the all-plain structure, easy integration, and an unprecedented FOV of 170°.

For active depth sensing, we formulated an analytical design framework for metasurface projection optics. We prove that the quadratic phase profile yields optimal beam quality for single-layer metasurface projectors, and demonstrate a singlet metasurface projector design with 140° FOV and diffraction-limited performance. We further show that distortion of the projected pattern can be corrected by resorting to a doublet meta-optics architecture, and implement a doublet projector design concurrently achieving 120° FOV, diffraction-limited performance, and vanishing distortion.

The proposed design frameworks foresee vast potential applications in areas including LiDAR, 3-D depth sensing, near-eye displays, and beyond. They can be potentially applied to different scenarios depending on the specific requirements, where

passive depth sensing techniques typically have less power consumption at the sacrifice of depth measurement accuracy. PSF engineering can be utilized to improve the accuracy of the passive depth sensing techniques, and further reduce the size and integration complexity of the device, which we will discuss in detail in the next chapter.

Chapter 5

Reconfigurable metalens using polarization-multiplexing

5.1 Introduction of polarization-multiplexing

In recent years, the field of metamaterials has undergone tremendous advancements, enabling unprecedented control over the behavior of electromagnetic waves. However, while conventional metasurfaces offer remarkable functionality, their static nature limits their adaptability and hampers their potential in dynamic environments. To overcome this constraint, the concept of reconfigurable metasurfaces has been introduced, allowing for real-time control over their electromagnetic response. By harnessing active or passive elements, such as varactors, MEMS, phase-change materials, or liquid crystals, these metasurfaces offer unprecedented capabilities to dynamically alter their properties in response to external stimuli.

The main objective of the following two chapters is to explore the vast possibilities offered by reconfigurable metasurfaces and to investigate their potential for revolutionizing light manipulation and wave-based technologies. By dynamically altering the meta-atom properties, such as resonance frequency, amplitude, phase, polarization, or scattering characteristics, we can harness the unique ability of reconfigurable metasurfaces to actively control and mold electromagnetic waves with unparalleled flexibility.

Conventional reconfigurable metasurfaces involve the integration of active elements that can actively manipulate the electromagnetic response. Active components, such as varactors, electro-optic materials, or MEMS devices, can be incorporated into the meta-atom structure to enable dynamic control of the metasurface properties. By applying external stimuli such as voltage, electric fields, or mechanical forces, the active elements modify the resonance frequency, phase, or polarization response of the meta-atoms, thereby achieving reconfigurability.

Active components, however, add up system complexity, power consumption, and also bring the integration challenge. Liquid crystals (LCs) offer another versatile method for achieving reconfigurable metasurfaces. LCs are highly responsive to external stimuli, such as electric fields, temperature, or light, and exhibit controllable refractive indices and birefringence. By embedding LCs into the meta-atom design, the orientation and alignment of LC molecules can be manipulated, leading to tunable optical properties. The reorientation of LCs allows for the dynamic modification of metasurface characteristics, such as polarization-dependent response or beam steering, making LC-based metasurfaces highly adaptable and reconfigurable.

While LCs offer low driving voltage and continuous tunability, they are limited by the resolution, which makes them difficult to have nanoscale integration. In the thesis, we propose two different active tuning mechanisms - through polarization multiplexing and using PCMs, which bring meta-atom level flexibility, and enables the active tuning of the metasurface wavefront. Polarization multiplexing will be discussed in detail in the chapter, and PCMs will be discussed in the next chapter.

Polarization-multiplexing involves the design of the meta-atom geometry, so that it has different optical phase delay and amplitude response under the incident of light with different polarization states. This can be achieved using the meta-atoms without four-fold symmetry, which brings the asymmetry of the dielectric components to the polarization direction. In this way, two or more phase profiles can be integrated into a single layer metasurface through the distribution of the meta-atoms of various geometry patterns onto the entire metasurface.

In the next two sections, we discuss two applications of the polarization-multiplexed

metasurfaces, where a double-helix (DH) metasurface with two DH PSFs rotating in the opposite direction under the two orthogonal polarization states is shown in Section 5.2, and a reconfigurable parfocal zoom metalens in the visible band with 10x different zoom ratio in the orthogonal polarization states is shown in Section 5.3.

5.2 Double-helix metalens for monocular depth sensing

Chapter 4 discussed a variety of passive and active depth sensing techniques. As mentioned, active depth sensing techniques require active illumination and modulation components, which add to system complexity, cost and power consumption. On the other hand, stereoscopic imaging techniques are limited by the trade-off between system size and depth resolution.

To solve these issues, point-spread-function (PSF) engineering has been invented. It contains special phase mask that engineers PSF of the system, and depth information can be encoded into the captured image directly. Depth-from-defocus methods[92–97] use PSFs from standard lenses, and object depths can be extracted from a sequence of blurred images at different system conditions. They have low depth estimation accuracy due to the intrinsic limitation that defocused PSF varies slowly along the opical axis. In order to increase precision, a variety of special PSFs have been designed that exhibit significant change with object depth. They include astigmatic PSF[100], biplane PSF[101], tetrapod-like PSF[102–104], etc. Among them, double-helix (DH) PSF engineering[105–110] contains a phase mask that modifies the wavefront, and generates PSF of two rotating foci, where the rotation angle determines the object depth. It simplifies image data post-processing due to its shape simplicity. To achieve wavefront modulation, a DH phase mask generated by the spatial light modulator (SLM) is placed in the Fourier plane of the 4f system, which however brings alignment problems and restricts compactness of the entire system.

A single layer DH metasurface was experimentally realized by Jin *et al*[111]. The

image captured by the DH metasurface is the convolution of the scene with the DH PSF, which means rotation angle can only be estimated with the prior knowledge of the original object. To solve this issue, Colburn *et al* placed a DH metasurface and extended depth-of-focus (EDOF) metasurface side to side, where the image of the original object can be obtained from the EDOF lens through scene reconstruction[112]. However, two metasurfaces build up system cost, and special algorithm needs to be utilized to account for the off-axis illumination. Also, the system resolution is limited by the EDOF metasurface PSF. The two metasurfaces can be multiplexed together through the phase change materials[113], but they are limited by the fabrication cost and applicable spectral range. Decoupled pair of conjugate single-helix PSF can be used to substitute the DH and EDOF PSFs[281], however, it requires accurate calibration of the lateral displacement of the focal spots between the two states.

In this section, we propose a polarization-multiplexed DH metasurface design offering both depth sensing and scene reconstruction with a single metasurface, which shows optimal system simplicity and resolves the off-axis illumination issue. The resolution is determined by the DH phase mask alone. As one specific example, the design works in 635 nm wavelength with the depth range of 40-210 mm and rotation angle of 80°. This concept is generically applicable to other wavelengths and depth ranges.

The DH phase mask is constructed based on superposition of Laguerre-Gaussian modes[282–284], it modifies the wavefront emitted from a point-source to generates two foci on the image plane, where orientation of the line connecting the foci depends on the point source distance. Rotation rate and depth range are determined by the choice of the Laguerre-Gaussian mode set. In previous implementations, a block-iterative weighted projection algorithm was utilized to optimize the DH phase mask and suppress the focal spot sidelobes, thereby improving depth estimation accuracy[112, 284, 285]. However, the optimization procedure is a time-consuming empirical process which requires constant human intervention. Here, we use a direct search (DS) algorithm[71, 196, 199, 214, 286] to optimize the DH phase mask. The figure-of-merit (FOM) for the DS is defined in Eqs. 5.1-5.3. It comprises the sum of

the lower intensities between the two foci over a discrete set of sampling rotation angles, minus variance of the intensities between different angles. Here, $I_1(\phi)$ and $I_2(\phi)$ are the intensities of the two foci of a certain rotation angle ϕ, $c(\phi)$ compensates for illumination intensity decrease of the point source at increasing distance, $z(\phi)$ denotes the distance of the point source, N represents the total number of rotation angles sampled, $S^2\{I(\phi)\}$ calculates the variance of the intensities among different angles, and $\kappa = 1$ is a weighting factor. Eq. 5.4 gives the relationship between rotation angle and distance using the same notations as in Ref. [112], with V_1 and ω_0 being free parameters to control the rotation rate and depth range.

$$FOM = \frac{1}{N}\sum_{i=1}^{N} I(\phi_i) - \kappa \cdot S^2\{I(\phi_i)\} \tag{5.1}$$

$$I(\phi) = min\{I_1(\phi), I_2(\phi)\} \cdot c(\phi) \tag{5.2}$$

$$c(\phi) = z(\phi)^2 \tag{5.3}$$

$$z = \frac{\pi\omega_0^2}{\lambda} tan(\frac{\phi_0 - \phi}{V_1}) \tag{5.4}$$

With a DH phase mask, an image formed through the metalens is the convolution of the DH PSF and the object. Without prior knowledge of the object, it is not possible to extract the true object information from a single-shot image. We eliminate this ambiguity by multiplexing two DH phase masks with opposite rotation directions into a single metalens. The two phase masks share an identical layout albeit with their x and y coordinates swapped, and therefore only one phase mask design is required. After acquiring two images corresponding to the two polarization states, a series of deconvolution operation is performed on them assuming DH PSFs of varying rotation angles. Since the two images capture the same object, their deconvolved outcome should be identical provided that a correct rotation angle is used. Therefore, by identifying the deconvolved image pair with maximum similarity, the rotation

angle and hence object depth can be unambiguously determined. More details of the depth retrieval algorithm are discussed in the following part of the section. Further improvement of the design is possible leveraging the rise of end-to-end optimization framework in recent years, which provides an alternative approach to optimize both the meta-optical frontend and the reconstruction algorithm[227, 287, 288].

An approach similar to that in ref. [66] is employed to design polarization-multiplexed meta-atoms. The meta-atom structure is schematically depicted in Fig. 5-1(a), comprising a 450 nm thick rectangular amorphous silicon nano-post sitting on a fused silica substrate. The geometries of the nano-posts are designed according to the polarization directions of the incident light. The meta-atom pitch is fixed at 300 nm. The finite-difference time-domain (FDTD) method is used to analyze the meta-atom responses. The phase delay and transmittance of the meta-atoms under x-polarized incident light are shown in Figs. 5-1(b)-(c). Data pertinent to y-polarized light can be trivially obtained by swapping the x and y coordinates. The phase difference between two polarization states is shown in Fig. 5-1(d). A 2-bit design [235] containing 16 meta-atom structures of different lateral dimensions is chosen to allow independent control of the metalens' phase profiles in both polarization states. The meta-atom dimensions are listed in Tab. 5.1.

Table 5.1: Polarization-multiplexed meta-atoms

Meta-atom index	**1**	**2**	**3**	**4**	**5**	**6**	**7**	**8**
X dimension [nm]	136	159	159	148	90	98	90	90
Y dimension [nm]	140	90	98	109	159	98	117	132
X-pol phase [°]	-3	-17	-4	-10	125	87	83	98
Y-pol phase [°]	5	125	183	273	-17	87	180	274
X-pol transmittance	0.87	0.89	0.89	0.89	0.81	0.88	0.89	0.86
Y-pol transmittance	0.88	0.81	0.76	0.76	0.89	0.88	0.74	0.78
Meta-atom index	**9**	**10**	**11**	**12**	**13**	**14**	**15**	**16**
X dimension [nm]	98	117	228	105	109	132	121	117
Y dimension [nm]	159	90	228	121	148	90	105	117
X-pol phase [°]	183	180	185	186	273	274	261	264
Y-pol phase [°]	-4	83	185	261	-10	98	186	264
X-pol transmittance	0.76	0.74	0.70	0.74	0.76	0.78	0.77	0.77
Y-pol transmittance	0.89	0.89	0.70	0.77	0.89	0.86	0.74	0.77

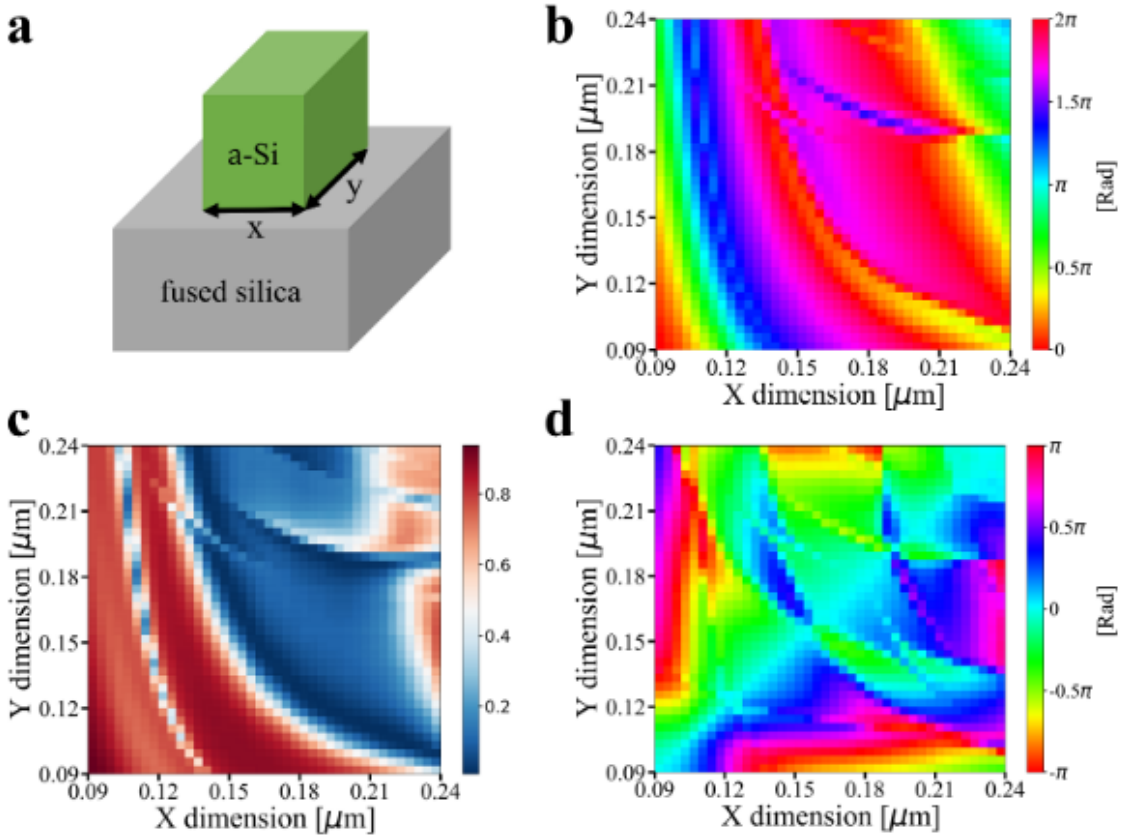

Figure 5-1: Polarization-multiplexed meta-atom design. (a) Illustration of the meta-atom structure. (b) Phase delay and (c) transmittance of the meta-atoms with x-polarized incident light. (d) Phase delay difference between the two polarization states.

As a proof of concept, we designed a metalens with 1 mm aperture size and 5 mm focal length. Parameters in Eq. 5.4 are taken as $\omega_0 = 125$, $\phi_0 = 180°$ and $V_1 = 2$, identical to those in ref. [112]. The DS optimization was performed with $N = 41$ in Eq. 5.1, i.e. with 41 evenly spaced discrete rotation angles at a step size of 2°. The designed metalens has a rotation angle up to 80°, corresponding to a depth sensing range of 45 - 212 mm.

The so-designed metalens was fabricated through electron-beam lithography followed by reactive-ion etching. Figure 5-2 presents optical microscope and scanning electron microscope (SEM) images of the fabricated metalens, showing excellent uniformity and pattern fidelity.

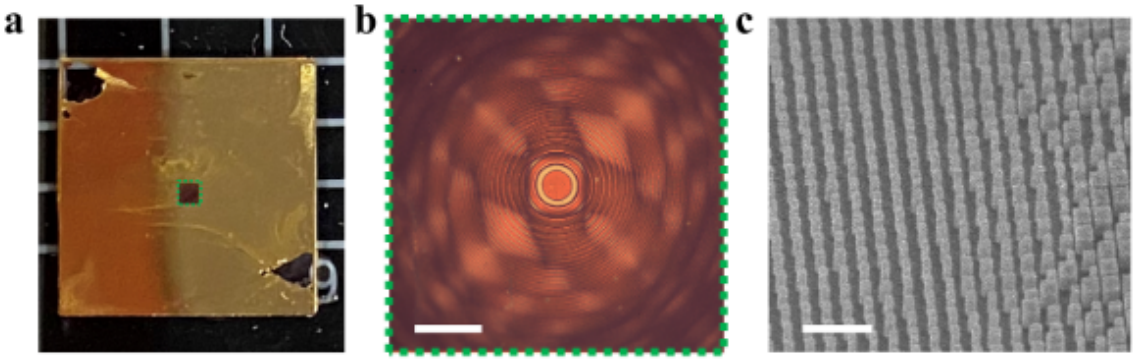

Figure 5-2: (a) Fabricated metalens on the silica substrate with metal mask. (b) Optical microscope image of the metalens. (Scale bar: 200 μm.) (c) Scanning electron microscope image of the metalens. (Scale bar: 1 μm.)

The PSF of the fabricated metalens was first characterized. Figure 5-3 compares the simulated and measured PSFs with different rotation angles. In the simulation, Kirchhoff diffraction integral[201] is used to transform the near-field wavefront after exiting the metasurface to the intensity distribution on the image plane. During the PSF measurement, a monochrome micro-LED display (Jade Bird Display 5000DPI AMuLED Panel) is placed in front of the metalens at different distances, and a 40 μm diameter circular spot is displayed to emulate a point object. A telescope assembly is placed between the DH metalens and an image sensor (Arducam MT9J001) with a calibrated magnification of 5. A polarizer is mounted in front of the sensor to control the polarization state of the incident light. As seen from Fig. 5-3, excellent agreement

is obtained between our design and experiment throughout the entire depth range.

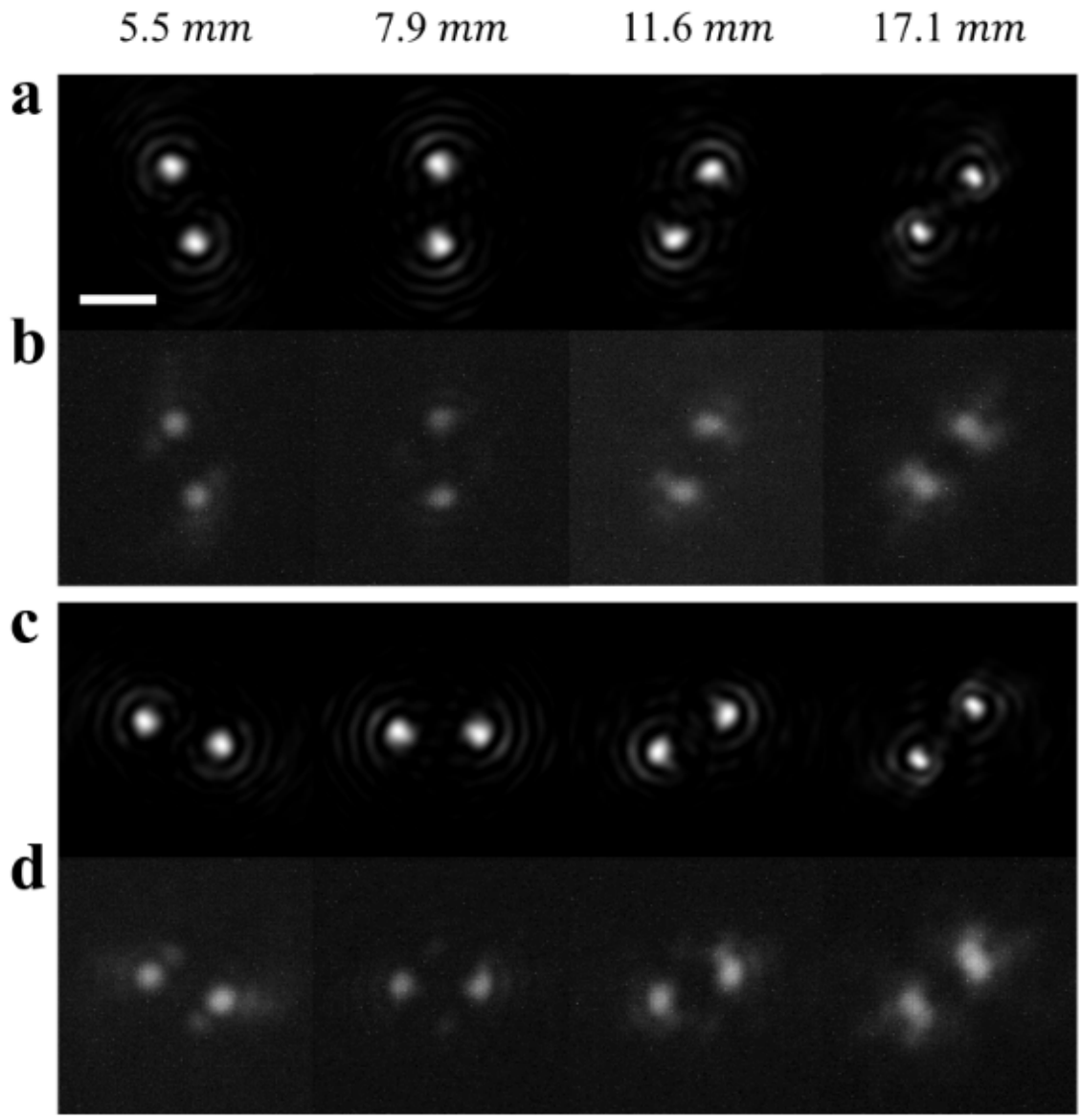

Figure 5-3: Metalens PSF. (a) Simulation and (b) experimental measurement of PSFs for different source distances in the x polarization state. (c) Simulation and (d) experimental measurement of PSFs in the y polarization state (scale bar: 20 μm).

The experimental setup consists of the micro-LED display projecting a '+' shaped pattern shown in Fig. 5-4(a) and placed at varying distances. The images captured by the DH metalens are shown in Fig. 5-4(b) and Fig. 5-4(c) for the two polarization states, respectively. To extract depth information and reconstruct the scene, these images are deconvolved using a set of PSF pairs with different rotation angles. Since

the two phase masks corresponding to orthogonal polarizations are linked via a reflection transformation, the sum of rotation angles of every PSF pair must equal 90°. We use Wiener deconvolution given in Eq. 5.5, where H is the Fourier transform of the image formed by the lens, G gives the Fourier transform of DH PSF (i.e., a cosine function), F denotes the Fourier transform of the deconvolved image, and $SNR = 0.1$ is the signal-to-noise ratio, which is an intrinsic parameter of the image sensor.

$$F = \frac{H \cdot G}{G^2 + SNR} \tag{5.5}$$

Three pairs of deconvolved images in two polarization states are shown in Figs. 5-4(d)-(e), each assuming a different rotation angle. We then computed the image correlation map between the image pair using Eq. 5.6, where 'corr' stands for the image correlation map, and h_1 and h_2 represent the deconvolved image pair. We further define the similarity parameter as the maximum value within the image correlation map, and Fig. 5-4f plots the parameter as a function of the rotation angle. Since the pair of images depict the same object, the similarity curve should reach maximum when the rotation angles of the DH PSFs used in the deconvolution are correct. The object depth can then be inferred according to the correct rotation angles.

$$corr(x, y) = \int h_1(x', y') \cdot h_2(x' - x, y' - y) dx' dy' \tag{5.6}$$

The protocol described above was applied to depth estimation of objects placed at different distances, and the measured depth values are shown as red dots in Fig. 5-4g. The analytical expression of Eq. 5.4 that our lens design is based on is also plotted as a solid line, showing excellent agreement.

To further characterize the lateral spatial resolution of the DH metalens, we replaced the '+' pattern on the micro-LED display with a standard USAF resolution chart. As an example, the captured images under x and y polarized light are shown in Figs. 5-5(a)-(b) for an object distance of 5.5 mm. The same deconvolution algorithm was performed to reconstruct the scene shown in Fig. 5-5c. The modulation transfer function (MTF) at different spatial frequencies was obtained from the image contrast

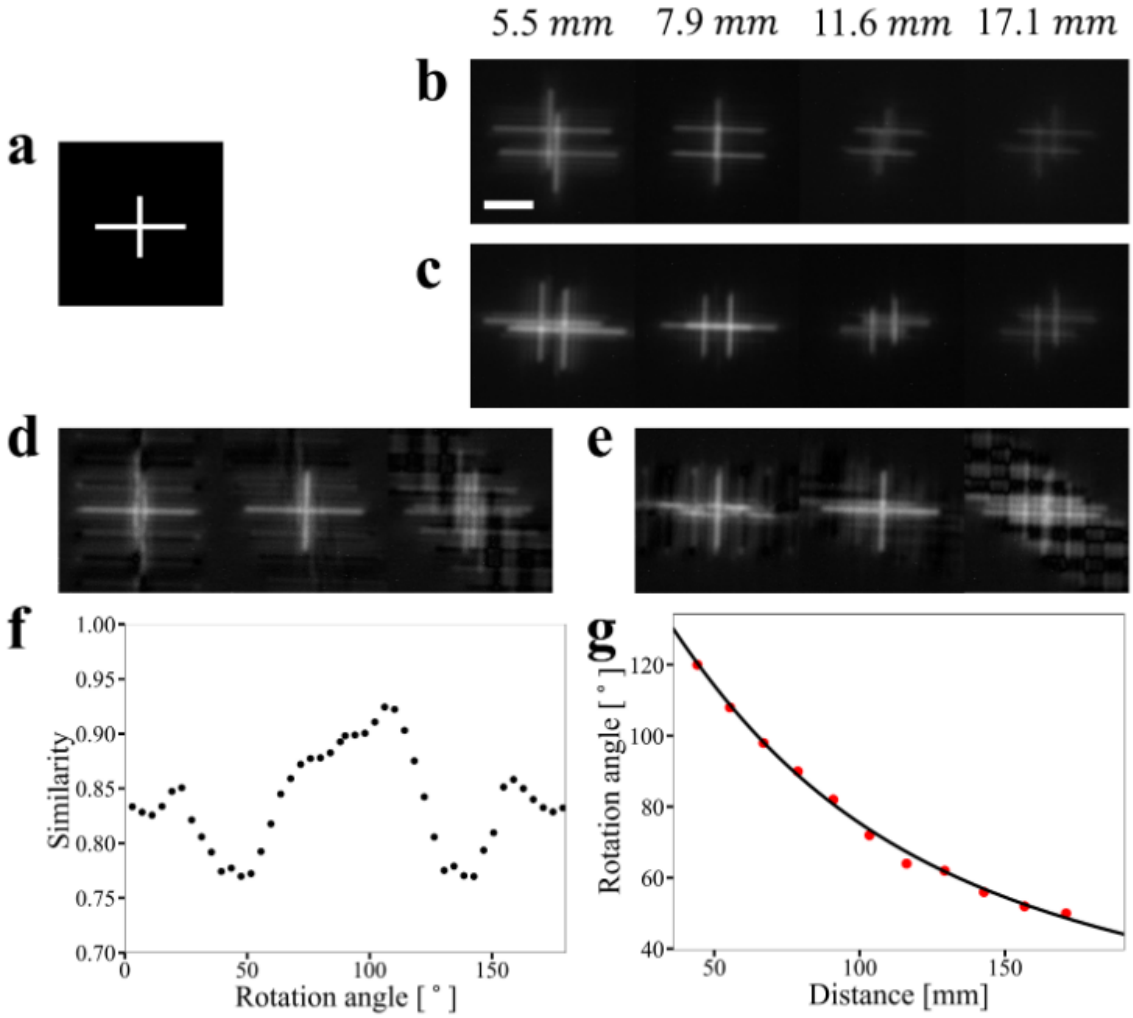

Figure 5-4: Experimental demonstration of image deconvolution to enable concurrent depth mapping and scene reconstruction. (a) A '+' pattern on the micro-LED display emulates an object. (b, c) Images in the (b) x-polarization state and (c) y-polarization state with different object distances. (d) Deconvolved images of the object at 5.5 cm distance using DH PSF rotation angles of 90°, 110°, and 130° (left to right), respectively. (e) Deconvolved images of the object at 5.5 cm distance with DH PSF rotation angles of 0°, −20°, and −40° (left to right), respectively. (f) Similarity of image pairs deconvolved using different DH PSF rotation angles. The maxmium point corresponds to the correct rotation angle. (g) Object depth estimation based on analytical expression (solid line) and experimental measurement (red dots). (Scale bar: 40 μm).

of the reconstructed resolution chart. In addition to the direct MTF measurement, we also evaluated the MTF from Fourier transform of the measured DH PSFs. Both sets of results are plotted in Fig. 5-5d with excellent agreement, which assures accuracy of our reconstruction algorithm.

Lastly, real world imaging was demonstrated using letters of 'M', 'I', and 'T' printed on card boards. The letters were displaced at different distances as shown in Fig. 5-6a. An LED light source with a center wavelength of 625 nm and 20 nm full-width-at-half-maximum (FWHM) spectral bandwidth was used to illuminate the scene, and a filter with 635 nm center wavelength and 10 nm FWHM bandwidth was placed in front of the image sensor to reject out-of-band light. The images recorded in the two polarization states are shown in Figs. 5-6(b)-(c). The aforementioned algorithm was implemented to infer the depth of the objects, with the caveat that oblique incidence onto the metalens (which leads to additional phase delay) was accounted for and corrected following procedures outlined in ref. [112]. The extracted depths are shown in Fig. 5-6d, which agrees well with the ground truth. The average error of depth estimation is 2.7%.

5.3 Reconfigurable parfocal zoom metalens in the visible band

Zoom lenses with adjustable effective focal length and magnification ratio are widely employed in cameras, microscopes, tracking, and monitoring applications. Conventional zoom lenses are composed of multiple refractive lens elements. They have mechanical movement along the optical axis[115–117] or shape change[118–122] to tune the effective focal lengths. However, the assembly of the multiple bulky optical components inevitably adds up the cost and the complexity of the system.

Zoom lenses remains a challenge to metasurface optics. A few designs have been proposed to realize zoom metalens. They can be integrated with stretchable substrate[75, 123, 289–291], lateral actuation[76, 128], and microelectromechanical

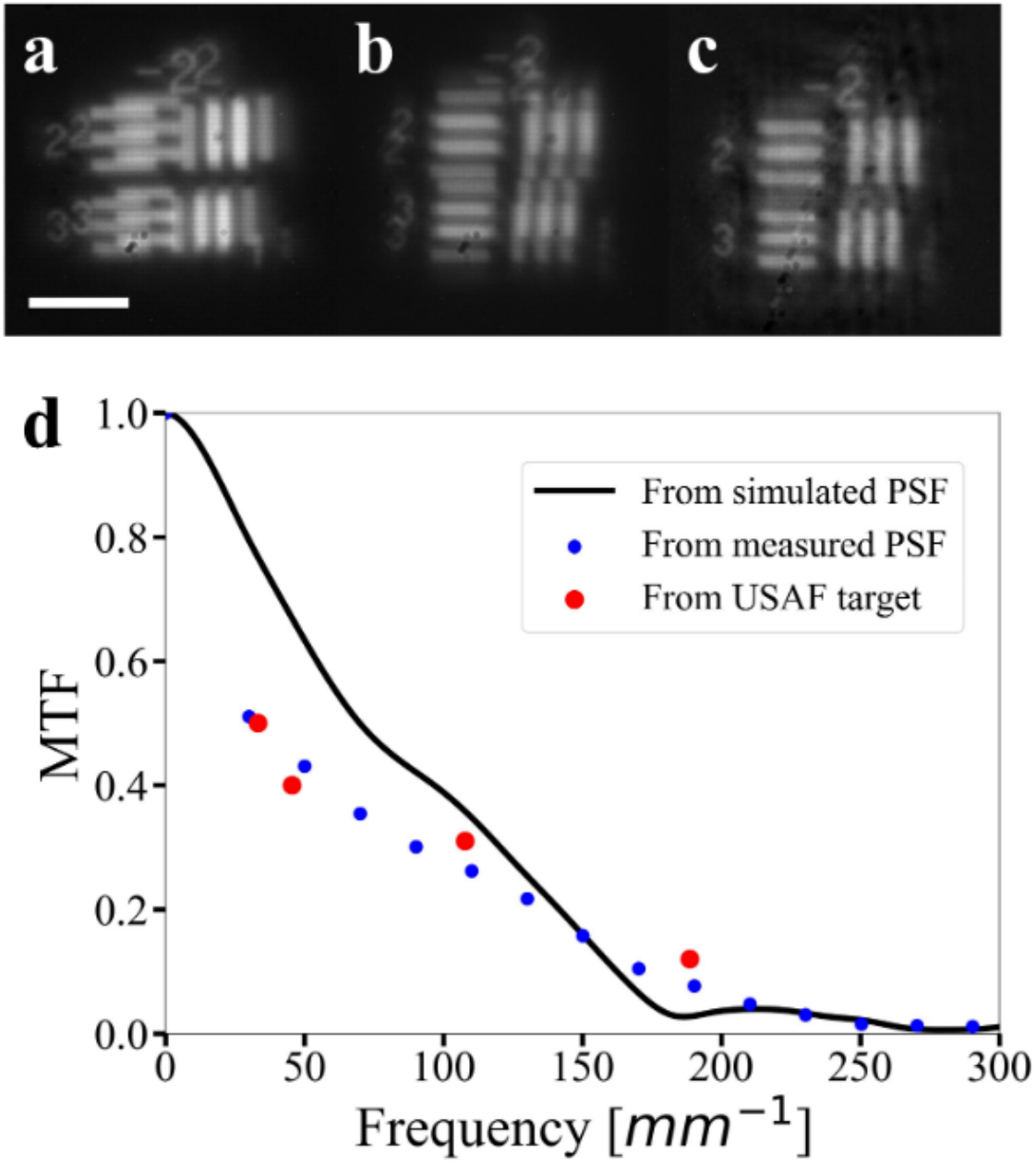

Figure 5-5: Imaging of the USAF target for evaluating the lateral resolution. Experimentally captured images in the (a) x-polarization and (b) y-polarization states. (c) Reconstructed image of the USAF resolution target pattern. (d) Measured MTF of the metalens at an object distance of 5.5 mm. The red dots correspond to MTF measured from the USAF target and the blue dots are MTF calculated from experimentally measured PSFs via Fourier transform. The solid line gives MTF inferred from PSFs simulated by diffraction integral. (Scale bar: 80 μm).

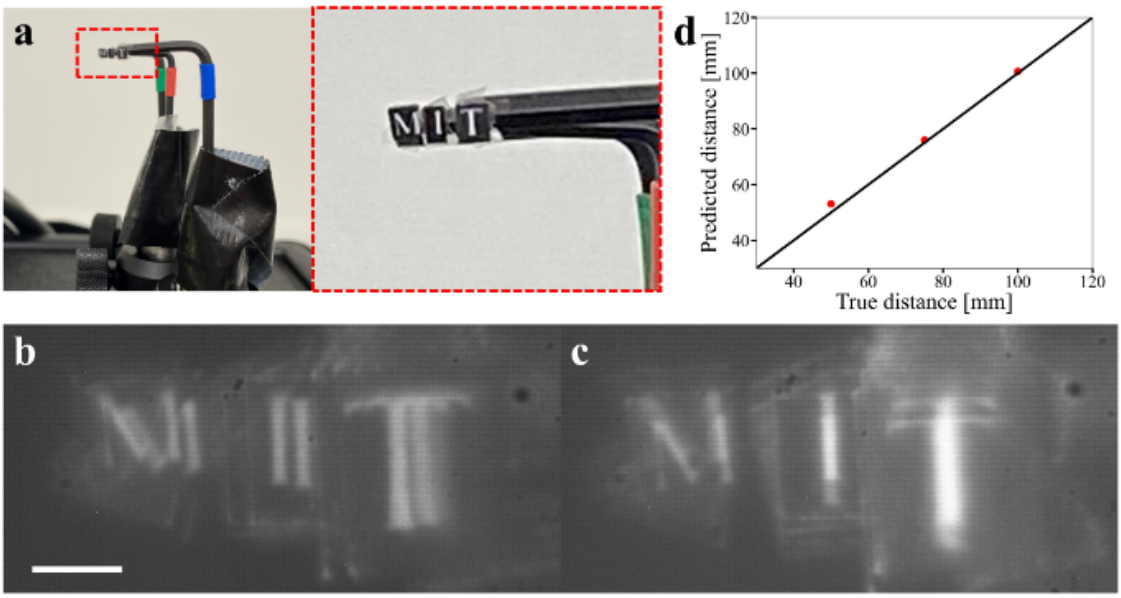

Figure 5-6: Experimental demonstration of depth sensing. (a) Photos of printed letters of 'M', 'I', and 'T', each placed at a different distance. (b, c) Captured images in (b) the x-polarization state and (c) the y-polarization state. (d) Inferred object distances (red dots) compared to the ground truth (solid line). (Scale bar: 80 μm).

systems (MEMS)[77, 292] to actively modify their optical responses and the angular magnification. However, all of them require active tuning of their mechanical structures, which restricts their practical applications. Moreover, most of the zoom lens designs are actually varifocal lenses[123, 128, 130, 132], the shifting of the focus while zooming requires additional compensation. A parfocal zoom metalens has been designed by Fu et al. with the same focus at the two zoom states[146]. The zoom lens is composed of polarization dependent meta-atoms so that the zoom switching can be accomplished by changing the polarization state of the incident light. However, it only has a small zoom ratio of 2. To the best of our knowledge, no parfocal zoom metalens has been experimentally demonstrated before, existing only numerical simulations.

In this section, we demonstrate a static zoom metalens design with the large zoom ratio of 10, which has 40° field-of-view (FOV) in the wide-angle regime and 4° FOV in the telephoto regime. The zoom lens is composed of polarization dependent meta-atoms so that the zoom state can be controlled by the polarization state of

the incident light. Also, the parfocal length remains constant in the two states. We fabricated and experimentally investigated the design in the visible band, though the design concept is generically applicable to other wave bands. To show the versatility of the design concept, we also present a zoom metalens in the mid-IR band using the phase change material GSST, which we will elaborate in the next chapter.

The zoom metalens assumes a doublet configuration as illustrated in Figures 5-7a-b. The two metasurfaces can be fabricated either on the opposite sides of a single substrate or on two separate substrates. Each metasurface encodes two different phase maps corresponding to two zoom states. In the wide-angle mode, the center part of the front metasurface serves as a negative lens which expands the incident light beam to a larger width on the back metasurface, and the back metasurface acts as a positive lens to form the image. The lens in this state therefore realizes a small EFL to accommodate a large FOV. In the telephoto mode, the front metasurface functions as a positive lens which focuses the incident light beam to a smaller area on the back metasurface. The back metasurface instead becomes a negative lens to realize a larger EFL than the wide-angle mode while maintaining the same parfocal length. The zoom ratio is defined as the EFL of the telephoto mode divided by that of the wide-angle mode.

A key feature of the design that sets it apart from previous proposals is that the front metasurface not only acts as a tunable lens but also a variable aperture without involving mechanical moving parts. This is essential to achieving a large zoom ratio while suppressing aberrations. In the telephoto mode, the front aperture coincides with the metasurface area. The wide-angle mode, however, reduces the front aperture size by blocking light transmission in the outside ring. This can be accomplished either by imposing a phase profile with a large gradient to deflect and trap light via total internal reflection in the substrate (which is what we opted for in both visible and mid-IR zoom lens demonstrations), or engineering the meta-atoms such that they curtail optical transmission in the wide-angle state.

As an example to illustrate our design, here we consider the polarization-multiplexed zoom lens following the concept discussed in this chapter. The lens is designed for

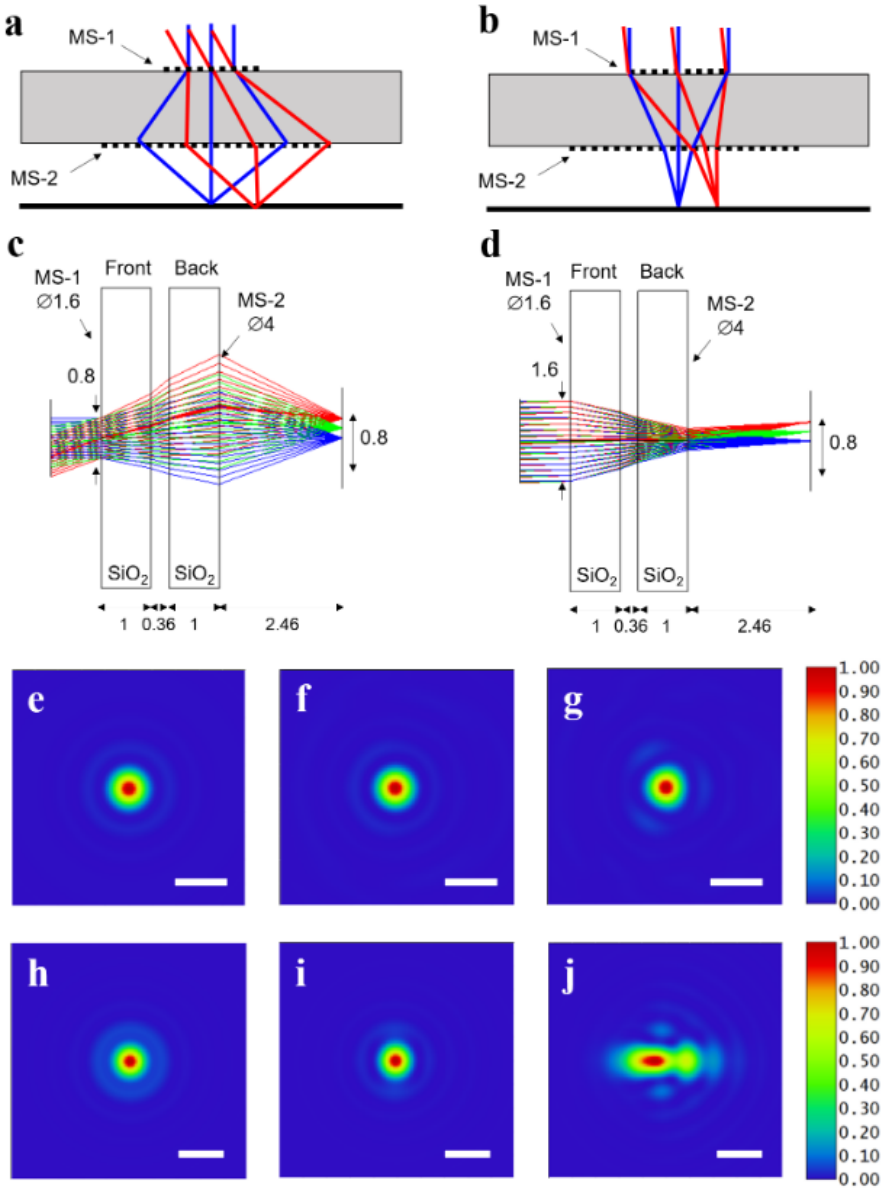

Figure 5-7: (a)-(b) Schematic illustration of the doublet zoom metalens configuration in the (a) wide-angle mode, and (b) telephoto mode. MS-1 and MS-2 labels the front and back metasurfaces, respectively. Note that the optical aperture sizes are different in the two imaging modes and controlled by the metasurfaces via reconfigurable wavefront shaping. (c)-(d) Ray trace simulation of the optimized polarization-multiplexed zoom metalens in the (c) wide-angle mode, and (d) telephoto mode. All the units are in mm. (e)-(g) Simulated focal spot profiles in the wide-angle mode with the AOI of (e) 0°, (f) 10°, and (g) 20°. (scale bars: 2 μm) (h)-(j) Simulated focal spot profiles in the telephoto mode with the AOI of (h) 0°, (i) 1°, and (j) 2°. (scale bars: 10 μm)

a target center wavelength of 670 nm, it comprises two 1 mm thick fused-silica substrates with an air-gap of 0.36 mm in between. The front metasurface has a diameter of 1.6 mm, and the back metasurface has a diameter of 4.0 mm. The back focal length has a fixed value of 2.46 mm with the maximum image height of 0.4 mm in both modes. The total track length of the lens is 4.82 mm. The phase profiles of the metasurfaces were numerically optimized by assuming an even order polynomials form:

$$\phi(r) = \sum_{i=1}^{11} A_i \left(\frac{r}{R}\right)^{2i} \tag{5.7}$$

where $R = 3\ mm$, r is the radial coordinate, and the A_i's are the polynomial coefficients. Figures 5-7c and 5-7d present ray trace simulation results of the optimized lens. The lens exhibits an EFL of 1.1 mm (corresponding to an f-number of 1.4 and a numerical aperture NA = 0.34) in the wide-angle mode and 10.8 mm (f-number 6.8 and NA = 0.07) in the telephoto mode. Figures 5-7e-g and 5-7h-j show the simulated focal spot profiles of the lens, featuring diffraction-limited performance over the entire 40° FOV in the wide-angle mode and over a 3° FOV in the telephoto mode, with near-diffraction-limited performance as the angle-of-incidence (AOI) increases to ±2° for the later case. The distortion is less than 5% in both modes. The lens therefore furnishes high imaging quality and negligible distortion in both zoom modes with a large zoom ratio of 10x. Further performance improvements can be realized by engineering angle-dependent response of meta-atoms or resorting to non-local metasurface designs [293].

In this embodiment, the two zoom states are associated with two orthogonal linear polarizations of the incident light. The polarization-multiplexed meta-atom structure is schematically depicted in Figure 5-8a, which assumes the form of a truncated rectangular waveguide made of amorphous Si (a-Si) sitting on a fused silica substrate. The meta-atoms have a unit-cell period of 0.3 μm with a height of 0.45 μm. The 670 nm wavelength incident light is linearly polarized along the x and y directions, parallel to the edges of the rectangular waveguide.

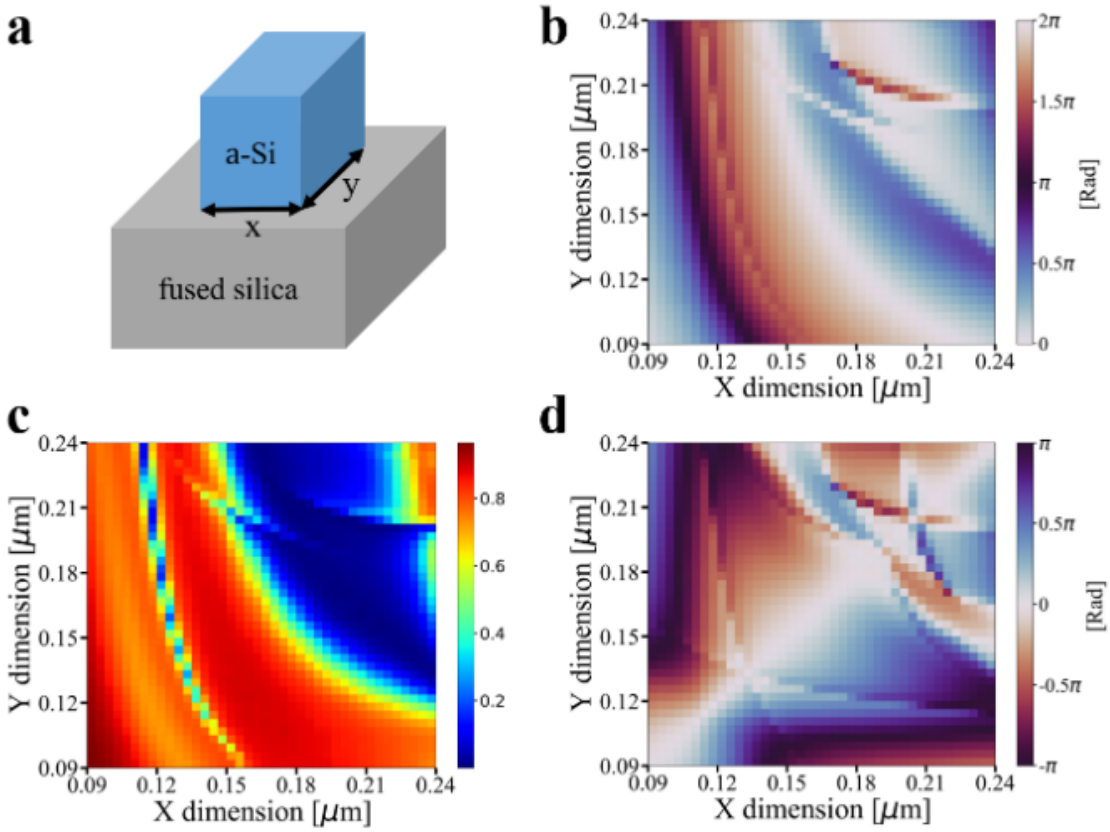

Figure 5-8: Polarization-multiplexed meta-atom design. (a) Schematic illustration of the meta-atom structure. (b) Phase delay and (c) amplitude response of the meta-atoms with the polarization of the incident light along the x direction. (d) Phase delay difference of the meta-atoms between the x and y polarization directions.

Table 5.2: Polarization-multiplexed meta-atoms

Meta-atom index	**1**	**2**	**3**	**4**	**5**	**6**	**7**	**8**
X dimension [nm]	144	132	167	159	190	98	90	90
Y dimension [nm]	144	190	102	113	132	98	125	140
X-pol phase [°]	-2	0	-2	1	86	87	87	97
Y-pol phase [°]	-2	86	182	266	0	87	185	270
X-pol transmittance	0.88	0.87	0.89	0.89	0.70	0.93	0.93	0.91
Y-pol transmittance	0.88	0.70	0.74	0.77	0.87	0.93	0.74	0.77
Meta-atom index	**9**	**10**	**11**	**12**	**13**	**14**	**15**	**16**
X dimension [nm]	102	125	236	109	113	140	128	125
Y dimension [nm]	167	90	240	128	159	90	109	125
X-pol phase [°]	182	185	177	180	266	270	267	278
Y-pol phase [°]	-2	87	184	267	1	97	180	278
X-pol transmittance	0.74	0.74	0.78	0.73	0.77	0.77	0.77	0.78
Y-pol transmittance	0.89	0.93	0.74	0.77	0.89	0.91	0.73	0.78

We simulated the meta-atom response with x-polarized light using the finite-difference time-domain (FDTD) method. Optical phase and amplitude imparted by meta-atoms with different lateral dimensions in the range of 90-240 nm are shown in Figures 5-8b-c. Response of the same meta-atom to y-polarized light can be directly inferred from the same data by swapping the x and y dimensions. The meta-atoms can cover the entire 0-2π phase range for the two polarizations. Birefringence of the truncated waveguide with respect to the two orthogonal linear polarization states controls the optical phase difference in two states. Figure 5-8d plots the phase delay difference between the two polarizations imposed by the meta-atoms, showing that the relative phase delay covers the entire range of $\pm\pi$, sufficient to provide arbitrarily reconfigurable phase profiles for both polarizations.

To construct the zoom lens, we chose 16 meta-atoms (i.e. a 2-bit design[235]) from the simulated meta-atom library to cover four phase levels of 0, $\pi/2$, π, and $3\pi/2$, with each meta-atom providing a distinct combination of two of the four discrete phase values for the two polarization states. As a result, the phase profiles of the metasurface can be independently controlled in response to the two polarizations. The selected meta-atom structures as well as their phase and amplitude responses are listed in Tab. 5.2. All meta-atoms have transmittance larger than 70%.

The metasurfaces were defined using electron beam lithography and plasma etching. A 450 nm thick amorphous Si film was deposited on a 0.5 mm thick fused silica wafer by plasma-enhanced chemical vapor deposition (STS PECVD). The wafer was then diced into square pieces with side length of 12.5 mm as metalens substrates. To fabricate the mask patterns of metalens, a negative tone of electron beam resist (ma-N 2402 from a mixture of ma-N 2401 and ma-N 2403, Micro Resist Technology) and then a conductive polymer (ESpacer 300Z, Showa Denko America, Inc.) were spin-coated on the substrates for electron beam lithography (EBL). The use of a conductive polymer avoids charging effects during EBL writing. The EBL was conducted at a voltage of 50 kV and a beam current of 1 nA (Elionix HS50). Then, the sample was put in the developer (AZ 726 MIF Developer) to produce the mask patterns and gently rinsed with deionized water. To etch amorphous Si, the dry-etching was performed by dual plasma sources and dual gas inlets with a mixture of SF_6 and C_4F_8 (SPTS Rapier DRIE). Residual electron beam resist was stripped by O_2 plasma ashing. Areas on the substrate not occupied by the metasurface were subsequently covered by a metal mask to prevent stray light. To fabricate the metal mask, a negative-tone photoresist (AZ nLOF 2035) was spin-coated on the metalens at 3000 rpm. The resist was soft baked at 115 °C for 1 min, exposed to UV light on a MLA150 Maskless Aligner, and then post-exposure baked at 115 °C for 1 min. The photoresist was developed by immersing the sample into Microposit MF-319 developer for 1 min and gently rinsed with deionized water. Then, a 200 nm thick Cr layer was deposited by electron beam evaporation at a rate of 2.0 Å/sec in a Sharon electron beam evaporator. Finally, the photoresist was removed in solvent stripper (Remover PG, MicroChem) to pattern the metal mask via lift-off.

Figures 5-9a-b show scanning electron microscope (SEM) images of the fabricated metasurfaces. After metasurface fabrication, metal apertures were patterned on the substrates, only exposing areas with the metasurfaces to eliminate unwanted stray light transmission (Figures 5-9c, e).

To characterize the metalens assembled from the two pieces of substrate, we started with evaluating the focal spot profiles of the zoom lens in the two polar-

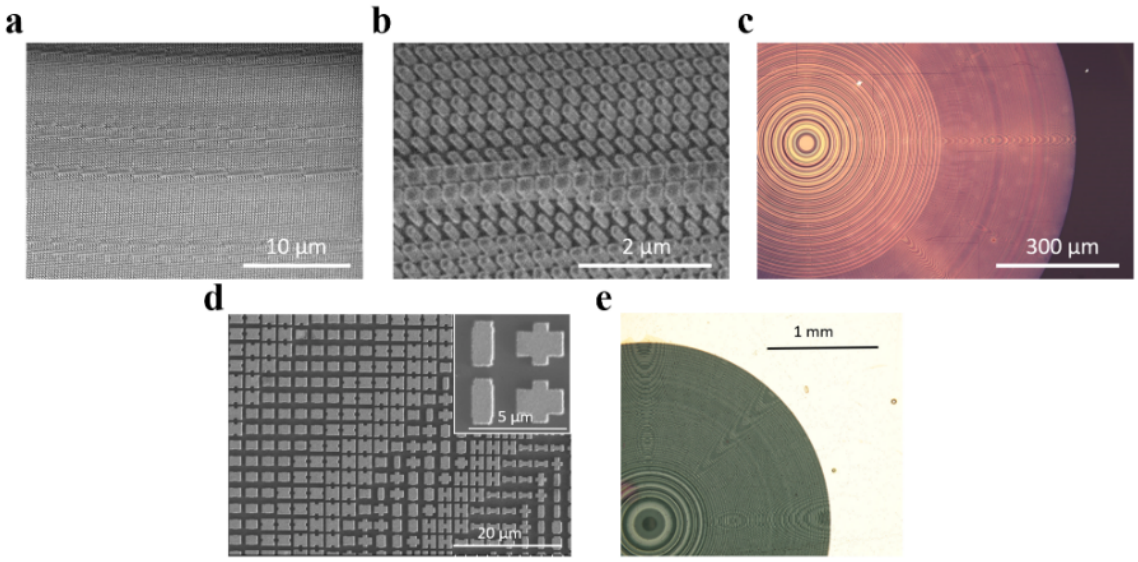

Figure 5-9: Fabricated metalenses. (a)-(b) SEM images and (c) optical microscope (OM) image of the polarization-multiplexed metalens. (d) SEM image and (e) OM image of the phase-change metalens.

ization states. The measurement setup is illustrated in Figure 5-10a. A 670 nm laser along with a collimator were both mounted on a custom-made circular track to adjust the AOI within the range of -20° - 20°. The focal spot was magnified by a pair of lenses forming a telescope assembly and captured by a CMOS image sensor. A polarizer was placed in between the laser and the zoom lens to control the polarization state of the incident light. The focal spot images and the normalized cross-sectional optical intensity profiles at different AOIs and polarization states are presented in Figures 5-10b-m alongside the focal spot profiles of an ideal, aberration-free lens of the same aperture size and effective f-number. The Strehl ratios can be inferred from the peak value of the focal spot profiles. The full-width-at-half-maximum (FWHM) of the focal spots are summarized in Table 5.3, showing agreement between the simulation and experimental results. We further quantified the focusing efficiency of the zoom lens, which is defined as the ratio of optical power at the focal spot to the total power incident on the lens aperture. The focusing efficiency was assessed using a photodetector integrated with a 100 μm diameter pinhole. Our measurement indicated focusing efficiencies of 8% at the wide-angle mode and 14% at the telephoto mode of

Table 5.3: FWHM of the focal spots of the polarization-multiplexed metalens

Mode	Wide-angle (sagittal/tangential)			Telephoto (sagittal/tangential)		
AOI [°]	0	10	20	0	1.0	2.0
FWHM [μm] (simulation)	1.0/1.0	1.0/1.0	1.0/1.0	4.8/4.8	4.7/4.8	3.9/9.5
FWHM [μm] (experiment)	1.1/1.1	0.8/1.0	1.0/1.1	5.3/5.3	4.9/4.9	4.5/4.9

the doublet zoom lens.

We used a similar setup to characterize the imaging performance of the zoom lens in two modes. A printed white board containing standard USAF resolution chart patterns and different sizes of 'MIT' characters was placed 0.5 m away from the zoom lens. An LED light source with 660 nm center wavelength and 20 nm FWHM spectral bandwidth was used to illuminate the object. The image was magnified using the telescope assembly and captured by the image sensor. A polarizer is placed in front of the sensor to control the imaging mode of the zoom lens. The images of the object in the two polarization states are shown in Figures 5-11a-f, indicating excellent image quality in both states with negligible cross-talk, and a measured magnification ratio of 9.6x. The slight deviation from the 10x design target is likely due to the slight deviations of the air-gap thickness and image plane position from the design.

5.4 summary

In this chapter, we demonstrated two applications of reconfigurable metasurfaces using polarization-multiplexing technique. Through the design of rectangular-shaped meta-atoms which exhibit different effective refractive indices in the two orthogonal polarization states, the phase profile of the metasurface can be independently controlled.

We first demonstrated a monocular metalens design capable of perform both depth sensing and scene reconstruction concurrently. The design leverages polarization-multiplexing to encode two phase masks, each generating an optimized DH PSF. Our design ensures that rotation angles of the two contra-rotating PSFs are always complementary, which enables unambiguous depth perception without prior knowledge

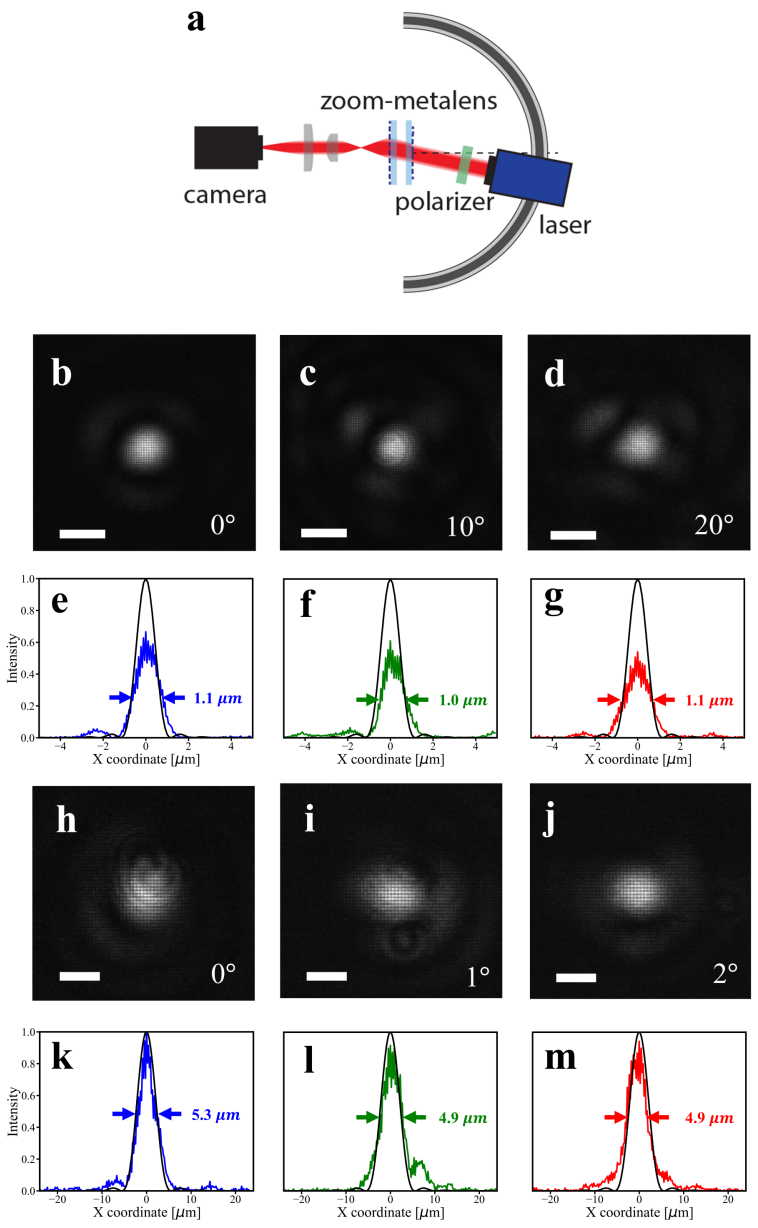

Figure 5-10: Focal spot characterization. (a) Schematic illustration of the measurement setup. (b)-(d) Focal spots at various AOIs in the 40° FOV wide-angle mode. (scale bars: 2 μm) (e)-(g) Normalized intensity distributions of the focal spots on the focal plane at AOIs of (e) 0°, (f) 10°, and (g) 20° in the wide-angle mode. (h)-(j) Focal spots at various AOIs in the 4° FOV telephoto mode. (scale bars: 5 μm) (k)-(m) Normalized intensity distributions of the focal spots on the focal plane at AOIs of (k) 0°, (l) 1°, and (m) 2° in the telephoto mode. The color lines are from the measurement, and the black lines are from an ideal aberration-free lens with the same NA. Their peak intensities are normalized to have the same power within an area of a diameter equaling to 5 times the focal spot FWHM.

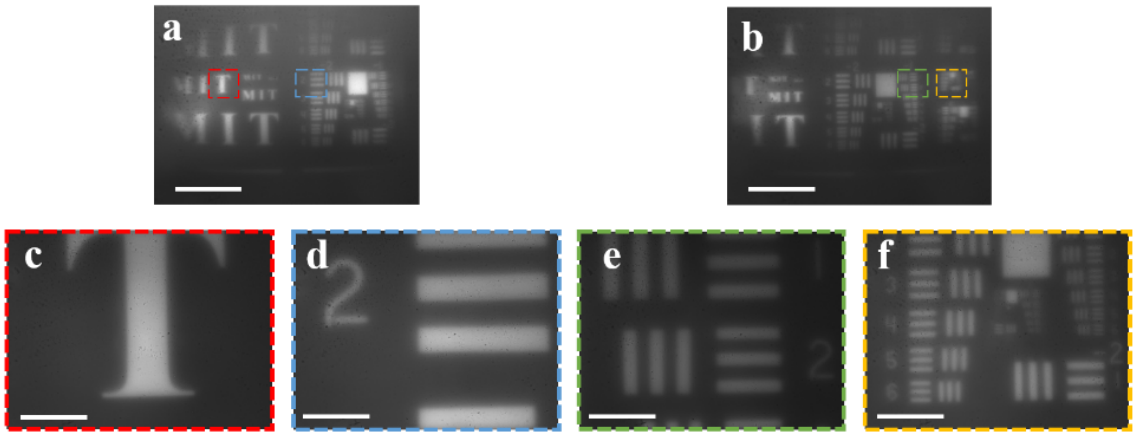

Figure 5-11: Experimental demonstration of zoom imaging. Images captured by the zoom metalens in the (a)-(b) wide-angle mode (scale bars: 10° FOV) and (c)-(f) telephoto mode (scale bars: 1° FOV).

of the scene. Compared to other depth sensing methods, our MDE approach features a single-aperture, compact footprint, high depth and lateral resolution, and passive operation. These advantages foresee vast potential applications of our technology in areas such as microscopy, medical imaging, virtue/augmented reality, automotive/robotic sensing and beyond.

We then proposed a non-mechanical zoom lens architecture offering large zoom ratios, negligible distortion, and diffraction-limited performance. Leveraging this generic architecture, we use polarization-multiplexed metasurfaces to achieve optical zoom at visible wavelengths. While the prototype is monochromatic, dispersion-engineered metasurface designs can potentially be adopted to further empower the zoom lenses with multi-color or even broadband functions[5, 31, 170, 214, 220, 222, 223, 227]. The versatile, multi-functional zoom metalens platform features a compact form factor, excellent image quality, and no mechanical moving parts, thereby foreseeing new applications in microscopy, optical sensing, image projection, and medical imaging.

A variety of different reconfigurable mechanisms can be utilized for tunable metasurface design. While polarization-multiplexing shows independent wavefront control, it requires the integration of the polarizer to control the polarization state of the in-

cident or captured light, and also reduces the focusing efficiency by half. In the next chapter, we will discuss another reconfigurable mechanism through the utilization of phase change materials in the infra-red region, and demonstrate a few application examples.

Chapter 6

Reconfigurable metalens using phase change materials

6.1 Introduction of phase change materials

phase change materials (PCMs) have garnered significant attention in the field of photonics and optoelectronics. They exhibit reversible changes in their optical properties, such as refractive index, absorption, and reflectivity, in response to external stimuli such as temperature, electric field, or light. These materials offer unique capabilities for manipulating light and enabling the development of advanced photonic devices.

One of the most widely studied and promising optical PCMs is $Ge_2Sb_2Te_5$ (GST), a chalcogenide alloy composed of Ge, Sb, and Te. GST undergoes a reversible phase transition between amorphous and crystalline states, leading to changes in its optical properties. In the amorphous phase, GST has a high refractive index and low reflectivity, making it suitable for data storage applications. In contrast, the crystalline phase exhibits a lower refractive index and higher reflectivity, enabling the development of optical switching and modulation devices. It shows applications spanning over photonic memory[294–296], reflective display[297–302], optical switching[303–308], optical computing[309–313], and active matematerials[235, 314–318].

Adjusting the stoichiometry within the GST family is a logical decision for the engineering of novel phase change materials. $Ge_2Se_2Sb_4Te_1$ (GSST) represents the

initial phase change material that has showcased significant differences in refractive index and wide-ranging bi-state transparency[319–321]. The wide transparency window of GSST starts from 1 μm wavelength for the amorphous state and 4 μm wavelength for the crystalline state, and extends to beyond 18.5 μm free from the typical Drude-like free-carrier absorption (FCA) common in PCMs.

The wide-ranging transparency of GSST has been acknowledged as a valuable characteristic that facilitates the development of high-performance photonic devices, including optical switches[322–325], switchable filters[326, 327], tunable gratings and multiplexers[328–331], and active metasurfaces[332, 333]. In addition to its minimal optical loss, GSST also demonstrates enhanced stability in the amorphous phase, allowing for significantly larger reversible thickness switching and improved optical mode confinement compared to GST.

In this chapter, we discuss reconfigurable metasurfaces working in the infrared using PCM GSST. The metasurface in the two states exhibits low absorption and independent phase control due to the low optical loss and large refractive index change of the PCM. We start with discussing the same reconfigurable parfocal zoom metalens architecture as in the last chapter, but instead of functioning in the visible using waveguide-type meta-atoms and polarization-multiplexing, this time we propose a zoom metalens in the mid-infrared in the form of a reconfigurable Huygens' surface made of PCMs. We then propose a phase-gradient modulation design concept coupled with direct search optimization to enable continuous tuning of metasurface optics with a minimal number of tuning elements, and designed a continuous tunable varifocal metalens using optical PCMs.

6.2 Reconfigurable parfocal zoom metalens in the mid-infrared band

To demonstrate that the zoom metalens architecture shown in the last chapter is agnostic to meta-atom type, the design was also implemented with a GSST-based recon-

Table 6.1: FWHM of the focal spots of the phase-change reconfigurable zoom metalens

Mode	Wide-angle (sagittal/tangential)				
AOI [°]	0	5	10	15	20
FWHM [μm] (simulation)	7.3/7.3	7.3/7.4	7.3/7.3	7.1/7.3	7.2/7.6
FWHM [μm] (experiment)	4.8/6.0	5.5/7.3	5.8/6.8	6.3/10.3	7.3/7.3
Mode	Telephoto (sagittal/tangential)				
AOI [°]	0	0.5	1.0	1.5	2.0
FWHM [μm] (simulation)	14.9/14.9	14.9/15.1	14.9/15.1	15.0/15.4	14.4/18.4
FWHM [μm] (experiment)	12.8/9.0	12.5/9.8	14.3/9.5	15.0/12.3	9.5/19.5

figurable Huygens' surface at 5.2 μm wavelength. Figures 6-1a-f illustrate the design and modeled focal spot profiles of the lens. Similar to the polarization-multiplexed counterpart, the lens also comprises two metasurfaces patterned on two mid-IR transparent CaF_2 substrates separated by an air gap. The lens performance is summarized in Table 6.1.

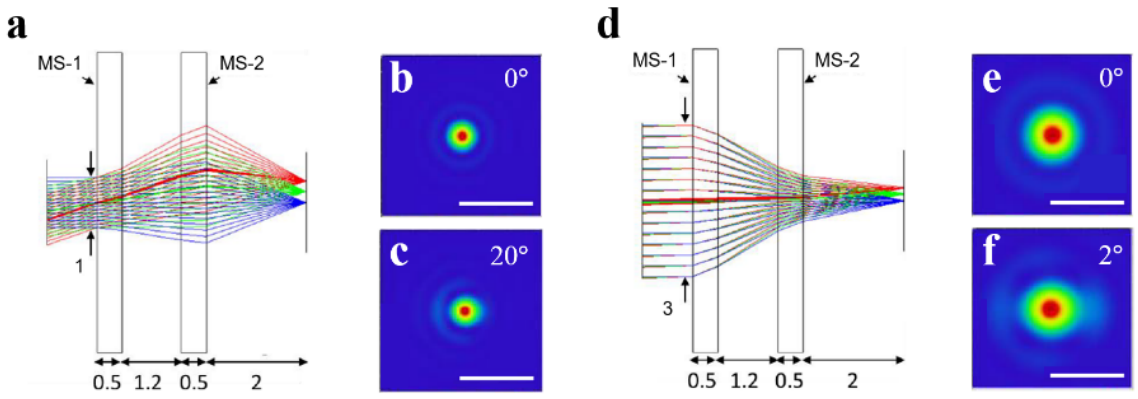

Figure 6-1: (a) Ray trace simulation, and (b)-(c) focal spot profiles of the phase-change reconfigurable zoom metalens in the wide-angle mode. (d) Ray trace simulation and, (e)-(f) focal spot profiles in the telephoto mode. (All the units are in mm, the scale bars are 30 μm.)

The metasurfaces are constructed from a library of pre-selected meta-atoms with 'H', 'I', and '+' shapes, which we have shown to support multiple electric and magnetic resonances, thereby providing broad optical phase coverage[1, 203]. We carefully

engineered the meta-atoms to realize arbitrary phase profiles in both amorphous and crystalline states, in order to achieve the desired functionalities. In ideal cases, the meta-atom designs should have high transmission and individual phase profile tuning ability under both states to fulfil the perfectly accurate phase map targets. However, due to the limited design degrees of freedom, this is impractical. Alternatively, we discretized the full 2π phase coverage (which is essential to most optical functionalities) into four 90-degree intervals for each state, so that every point along an arbitrary phase mask will be mapped to one of these four steps. For arbitrary reconfigurability, it is required that for each step in one state, there must be a structure that can assume each of the four steps in the other state. This requires a total of 16 unique structures, which we refer to as a 4-level or 2-bit design. We found an optimal set of meta-atom structures with a lattice constant of 3 μm, and thickness of 1.1 μm/1.065 μm for the amorphous/crystalline state, so that the full 2π phase coverage can be achieved under both states. We conducted a thorough parameter sweep, considering three types of resonators including H-shaped (Figure 6-2a), I-shaped (Figure 6-2b) and cross-shaped structures (Figure 6-2c). A sidewall angle of 85 degrees and 3.2% thickness shrinkage (when reconfigured from amorphous to crystalline state) were applied to the meta-atom models during simulation to account for the impact of fabrication and annealing processes. As shown in Figures 6-2a-c, each meta-atom was modeled using four distinct parameters. For each single meta-atom, unit cell boundary conditions were employed along both x and y axis for the calculation of transmission amplitude and phase. Open boundaries are applied in both the positive and negative z directions. X-polarized incident waves are illuminated from the substrate side and propagate in the z direction. Simulated transmission amplitudes and phases of meta-atoms with different shapes are plotted in Figures 6-2d-e. Through the combination of these different meta-atom structures, we are able to realize relatively high transmission within the entire 0-2π phase range under both amorphous state and crystalline state.

Sets of 16 meta-atoms (i.e. the 2-bit set shown in Figure 6-2f) that provide full 2π phase coverage in both states are selected from the simulation results plotted in

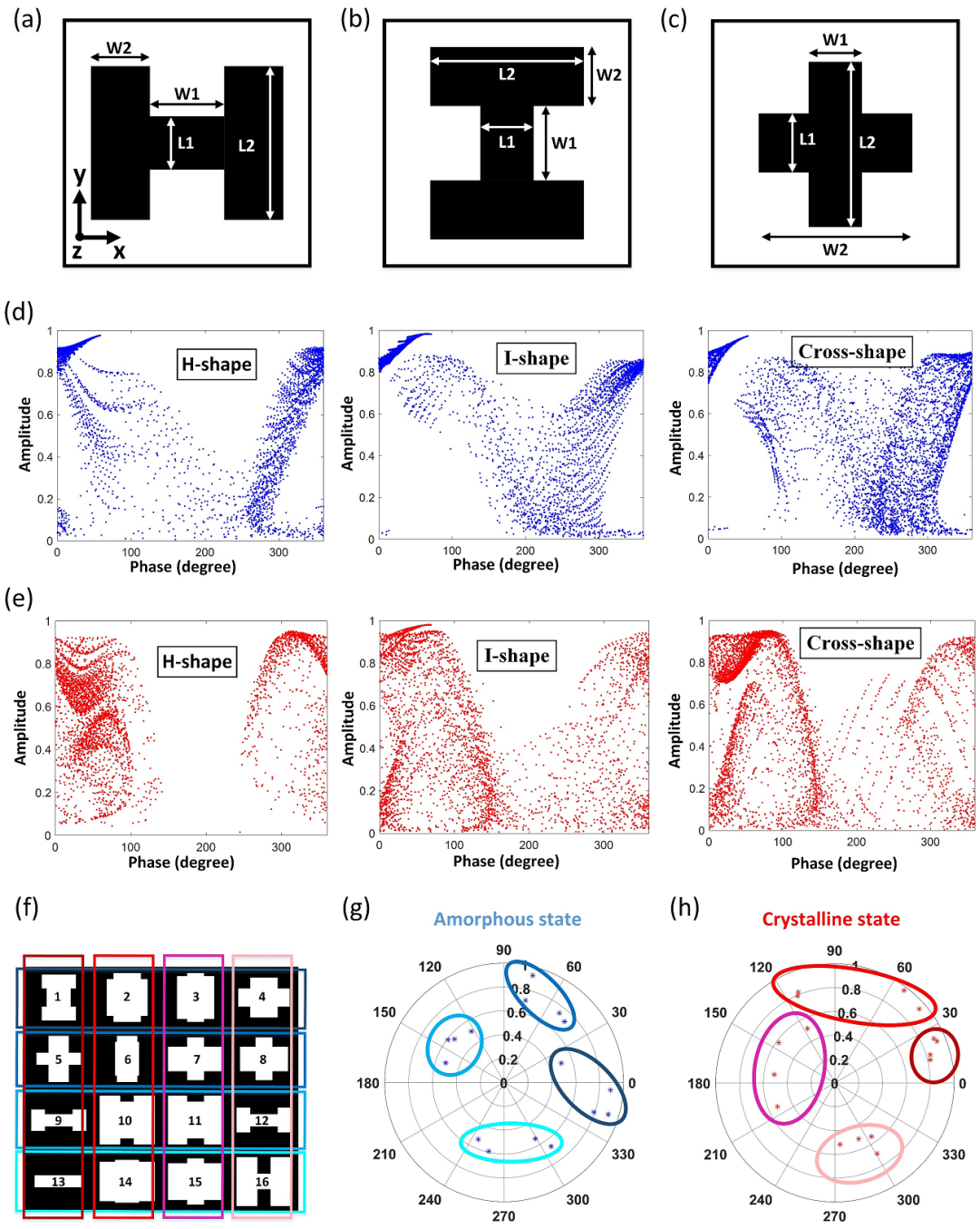

Figure 6-2: Schematic top-view of an (a) H-shaped, (b) I-shaped and (c) Cross-shaped meta-atom design, with x-polarized incidence. (d)-(e) Scatter diagrams of the transmission phase and amplitude derived with the different shaped meta-atoms shown in (a)-(c), under amorphous state (blue dots, figure (d)) and crystalline state (red dots, figure (e)), respectively. (f) Schematic top-view of all selected 2-bit meta-atom designs; (g) simulated phase and amplitude of the 16 meta-atoms under amorphous state; (h) simulated phase and amplitude of the 16 meta-atoms under crystalline state.

Figures 6-2d-e. These sets can be used in designs to generate arbitrary wavefronts under both amorphous and crystalline states. For each discrete phase under one state, four discrete phases covering 2π with about 90° phase intervals could be found at another state. More specifically, in Figure 6-2f, phase responses of meta-atoms that are circled in red (e.g. meta-atoms or cells #1, 5, 9 and 13) are similar under crystalline state, but are distributed in the 2π range with a 90° interval under amorphous state. Meta-atoms that are circled in blue (e.g. meta-atoms #13, 14, 15 and 16) are similar under amorphous states and different under crystalline state.

GSST films were deposited onto a double-side polished CaF_2 (111) substrate (MTI Corp.) by single-source thermal evaporation in a custom-made system (PVD Products Inc.)[334]. The substrate was held near room temperature throughout the film deposition process. Thickness of the film was measured with a stylus profilometer (Bruker DXT) to be 1.09 μm (a-state) and 1.03 μm (c-state), indicating 5% volumetric contraction during crystallization similar to other phase-change materials[335, 336]. The film was patterned via EBL on an Elionix ELS-F125 system followed by reactive ion etching (Plasmatherm, Shuttlelock System VII SLR-770/734). The electron beam writing was carried out on an 800-nm-thick layer of ZEP520A resist, which was spin coated on top of the GSST film at 2000 rpm for 1 min and then baked at 180 $°C$ for 1 min. To avoid the difficulty of ZEP removal after the etching step, we introduced a thin layer (about 200 nm) of 495 PMMA A4 between GSST and ZEP by spin-coating the photoresist at 4000 rpm and then baking it at 180 $°C$ for 1 min. Before resist coating, the GSST surface was mildly treated with standard oxygen plasma cleaning to improve resist adhesion. To prevent charging effects during the electron beam writing process, the resist was covered with a water-soluble conductive polymer (ESpacer 300Z, Showa Denko America, Inc.)[337]. The EBL writing was performed with a voltage of 125 kV, 120 μm aperture, and 10 nA writing current. Proximity error correction was also implemented with a base dose time of 0.03 $\mu s/dot$ (which corresponds to a dosage of 300 $\mu C/cm^2$). The exposed photoresist was developed by subsequently immersing the sample into water, ZED-N50 (ZEP developer), and isopropanol for 1 min each. Reactive ion etching was performed with a gas mixture

of CHF_3:CF_4 (3:1) with respective flow rates of 45 $sccm$ and 15 $sccm$, pressure of 10 $mTorr$, and RF power of 200 W. The etching rate was 80 nm/min. The etching was done in three cycles of 5 $mins$ with cooldown breaks of several minutes in between. After completing the etching step, the sample was soaked in N-methyl-2-pyrrolidone overnight to remove the residual ZEP resist mask. After optical characterization of the metalens in the amorphous (as-deposited) state, the sample was transitioned to the crystalline state by hot-plate annealing at 250 $°C$ for 30 min. The annealing was conducted in a glovebox filled with an ultra-high purity argon atmosphere. By using the lift-off technique described above, we lithographically defined 200-nm-thick gold apertures around the metasurfaces.

Fig. 5-9d-e present top-view SEM and optical micrographs of the GSST metasurface. Quantitative analysis of the SEM images taken on the metasurface revealed excellent pattern fidelity of the meta-atoms, with an average size deviation of only 20 nm from design values. The etched GSST meta-atoms have almost vertical sidewall profiles with a sidewall angle of 86°. The as-fabricated meta-atoms reside in an amorphous structural state. Structural phase transition (amorphous to crystalline) was triggered by annealing the metasurfaces on a hot plate at 250°C and in an inert gas ambient for 30 mins. While here we used thermal annealing to demonstrate switching operation of the prototype, the design concept can also be adapted to reversible electrothermal switching using on-chip micro-heaters to enable compact optics integration[338, 339].

The focusing performance of the lens was measured using a setup similar to that used for the visible zoom metalens. A 5.2 μm collimated laser beam incident at various angles, ranging from -20° to 20° in the amorphous state and -2° to 2° in the crystalline states, served as a far-field light source. Focal spot images were magnified using a telescope assembly and projected onto a liquid nitrogen cooled InSb focal plane array. The recorded focal spots form a crisp image, thereby verifying the change in observed FOVs and the target 10x zoom (Figure 6-3).

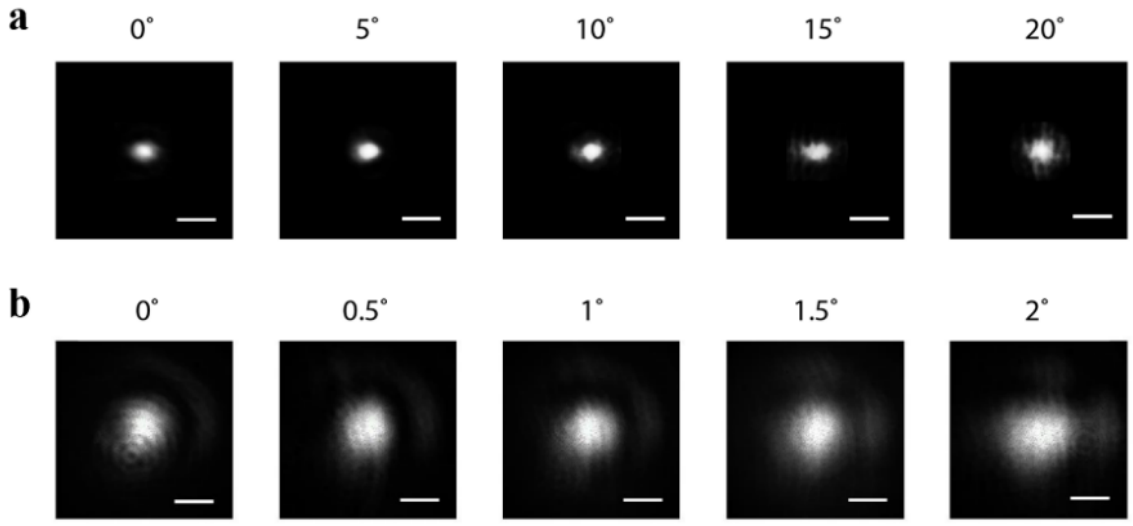

Figure 6-3: Focal spot profiles of the phase-change reconfigurable zoom metalens at different AOIs in the (a) wide-angle mode, and (b) telephoto mode. (The scale bars are 20 μm.)

6.3 Design of continuously tunable varifocal metalenses

Metasurfaces furnish a large collection of electrically-driven non-mechanical reconfiguration mechanisms commensurate with compact on-chip integration. Examples of these tuning schemes applicable to phase-gradient metasurfaces involve liquid crystals[10, 140, 340–343], transparent conducting oxides[344–347], multi-quantum wells[49, 348], phase transition oxides[349], and PCMs.

Most of these demonstrated reconfigurable metasurfaces are only designed to switch between a handful of discrete states. We note that even though most of the aforementioned reconfiguration mechanisms supports continuous refractive index change, this does not readily translate to continuous tuning of phase-gradient metasurfaces—for instance continuously changing the deflection angle of a meta-grating or varying the focal length of a metalens. To illustrate the problem, we consider a varifocal metalens with 1 mm diameter operating at 2.08 μm wavelength. Fig. 6-4a plots the phase profiles (after wrapping modulo 2π) of the metalens with three different focal length f = 4 mm, 6 mm, and 10 mm, assuming classical hyperbolic phase func-

tions. Fig. 6-4b analyzes the corresponding phase variations at three different spatial locations, r = 100 μm, 300 μm, and 500 μm from the lens center, as the focal length is continuously tuned from 4 to 10 mm. We see that the phases at the three locations evolve almost completely independently during the tuning process, evidenced by the appearances of multiple 2π phase discontinuities at largely uncorrelated f values. The conclusion holds true generally for spatial points across a tunable metasurface of a macroscopic size, provided that the points are not immediately adjacent to each other. This example epitomizes the challenge toward realizing continuous tuning: to satisfy the varying phase profile with spatially uncorrelated changes, tuning at the single (or few) meta-atom level is mandated. While tuning with such spatial granularity has been implemented in 1-D linear meta-gratings[49, 245, 341, 347, 350, 351], extending it to 2-D large-scale meta-atom arrays remains challenging due to technical difficulties associated with electrical addressing, cross-talk, and other complications[346, 352].

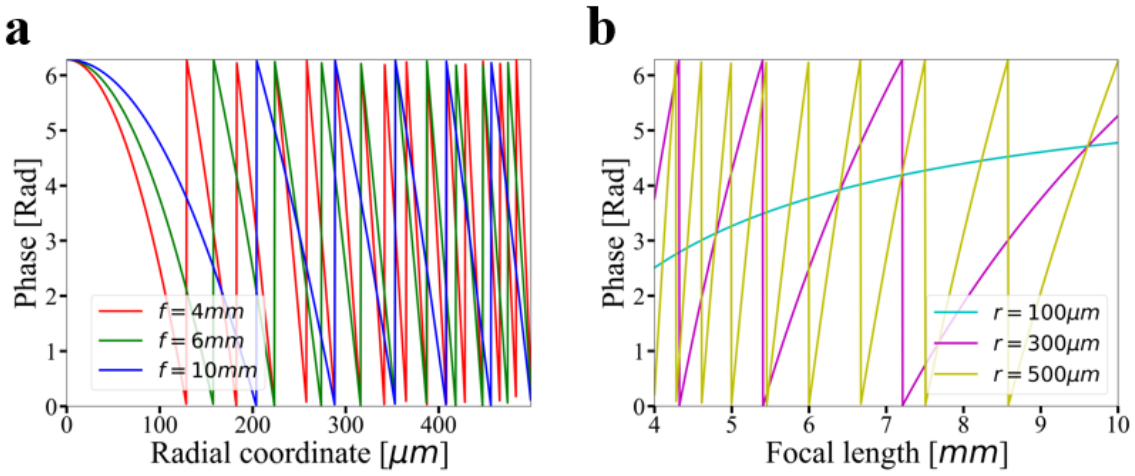

Figure 6-4: Ideal phase profiles of varifocal metalens. (a) Phase profiles of the metalens with focal lengths of 4 mm, 6 mm, and 10 mm. (b) Phase variations at spatial locations of 100 μm, 300 μm, and 500 μm as focal length tuned from 4 to 10 mm.

In this section, we propose a phase-gradient modulation design concept coupled with direct search optimization to enable continuous tuning of metasurface optics with a minimal number of tuning elements, and designed a continuous tunable varifocal metalens based on the concept using optical PCMs. The design concept is generically applicable to different reconfiguration mechanisms.

Unlike traditional active metasurface architectures, the phase-gradient modulation design does not directly tune the phase delay of meta-atom pixels. Instead, electrical contact pairs are used to generate an in-plane refractive index gradient in between each pair, which translates to a tunable phase gradient as is illustrated in Fig. 6-5. A functional meta-optical device is assembled from a multitude of phase-gradient modulation zones defined by the electrode pairs.

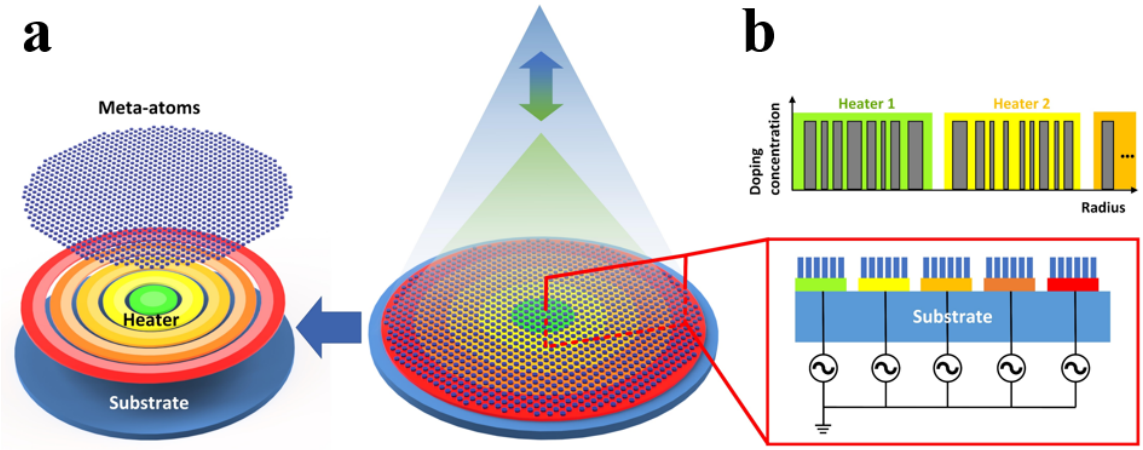

Figure 6-5: Schematic illustration of the varifocal metalens structure. (a) Schematic depiction (explosive view) of a varifocal metalens capable of continuous focal length tuning. The meta-atoms are grouped into a set of phase-gradient modulation zones each assuming a concentric ring shape. Each zone is electrically addressed to tune the optical phase gradient along the radial direction to produce the varifocal effect. (b) Cross-sectional schematic of a varifocal metalens based on electrothermal switching. Each zone contains two heaters at both ends (labeled with different shades). By adjusting the electric currents passing through the two heaters, variable temperature gradients can be established across the zone, which translates to an optical phase gradient.

The entire metalens is divided into several concentric zones, each with variable width (typically $10 - 100\ \mu m$ in our design) depending on the zone position. Isolation trenches are etched into the buried oxide at the boundaries of each zone. Since silicon has a thermal conductivity almost 200 times larger than that of silicon oxide, the isolation trenches serve to effectively block heat transfer between the zones and minimize thermal cross-talk. Two independently-biased doped silicon heaters are embedded within each zone as shown in Fig. 6-5b, where each heater comprises a

number of doped Si conducting channels (shaped as a set of concentric rings) whose widths and spacings are carefully optimized. Within a heater, a uniform voltage bias is applied across all of its doped Si conducting channels. When the two heaters are separately biased, a temperature gradient is established throughout the zone. For a fixed heating pulse duration, the volume fraction of a PCM meta-atom that transforms into a crystalline state directly correlates with the local temperature. The index change, which scales with the crystallization fraction, modifies the optical phase delay imparted by the PCM meta-atom. Therefore, by adjusting the voltages applied to the two heaters on two sides of a zone, a tunable optical phase gradient is established within the zone. Since each zone spans several tens of rows of meta-atoms and we only need two heaters per zone to tune the temperature gradient within the zone rather than local temperatures at every meta-atom, the number of individually controlled elements and hence complexity of the system is drastically reduced compared to individual meta-atom tuning.

Based on the design concept, the key requirement for the PCM meta-atom is that as the PCM is transformed from amorphous to crystalline state, the phase delay imparted by the meta-atom must be tuned over 2π range while maintaining high optical transmittance. We again choose GSST as the PCM, taking advantage of its large refractive index contrast and low optical attenuation in the near-infrared wavelength range. Moreover, the relatively slow crystallization kinetics of GSST allows a large reversible switching thickness critical to reaching 2π phase tuning[353]. We have also experimentally characterized GSST's optical constant evolution as a function of crystallization temperature on micro-heaters[2], and here we invoke the relationship measured at 2.08 μm wavelength (Fig. 6-6a) to quantify the dependence of meta-atom phase tuning on local temperature.

The meta-atom structure is schematically depicted in Fig. 6-6a inset, consisting of a GSST cylinder with a thickness of 380 nm and a diameter of 580 nm sitting on an SOI substrate. The SOI layer has a thickness of 40 nm and the buried oxide thickness is 3 μm. The meta-atoms are arrayed in a square lattice with a pitch of 1.3 μm. RCWA method is used to analyze the meta-atom response[354–356]. The

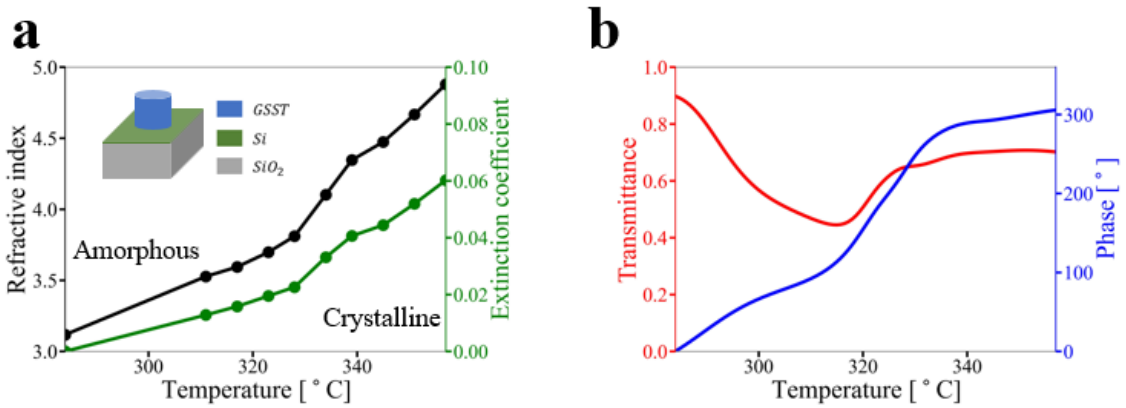

Figure 6-6: GSST meta-atom design. (a) Refractive index and extinction coefficient of GSST at different crystallization temperatures. Inset shows a schematic illustration of the meta-atom structure. (b) Transmittance and phase delay of the meta-atom as a function of crystallization temperatures. Figure a is reproduced from ref.[2], AIP Publishing AG.

transmittance and phase delay of the meta-atom at 2.08 μm wavelength are presented in Fig. 6-6b, showing near 2π phase tuning range as the meta-atoms are progressively transformed from amorphous to crystalline state[204].

As we discussed before, the two heaters within each zone are designed to generate a variable temperature differential when biased at different voltages. Since the crystallization temperatures of GSST fall in the window of 280 °C to 360 °C according to Fig. 6-6, the two heaters should be designed to produce arbitrary and spatially uniform temperature gradients within the temperature range. Intuitively, the voltages applied to two heaters define the extremum temperatures at the edges of the zone, and a smooth temperature gradient in between is established via optimization of the doped Si channel widths and spacings, which we address in the following.

The heater layout is schematically illustrated in Fig. 6-7. The entire metalens is divided into 23 zones with decreasing widths from the center to the edge. The positions of the zones are listed in Tab. 6.2, which correspond to the Fresnel zones of a lens with same size and 2.5 mm focal length. As one example, Figs. 6-7b-c show the heater design in zone 12, which covers a radial range of 16 μm around r = 348 μm. Fig. 6-8a plots the doping profile along the radial direction in the zone. There are a total of 10 doped conductive channels divided into two groups of 5 heaters, each group

connected in parallel to the same voltage bias forming one heater. It is also possible to use more than one doping concentration to further improve the temperature control although it is outside the present scope of this chapter. By applying different voltages of V_1 and V_2 at the two heaters, steady-state temperature profiles between 280 °C - 360 °C with varying gradients can be attained, with three examples shown in Fig. 6-8b. In this design, we used only one doping concentration, and thus the heaters can be formed within a single lithographic patterning and ion implantation step. The widths of the doped channels were optimized such that the temperature profiles closely follow linear trends. In Fig. 6-8c, the temperature deviations from the ideal linear profiles are quantified for the three voltage V_1 and V_2 combinations shown in Fig. 6-8b. The root-mean-square (RMS) deviation of 1.2 K translates to an average optical phase error of 6°, which has a minimal impact on the lens performance. The doped regions are listed in Tab. 6.3

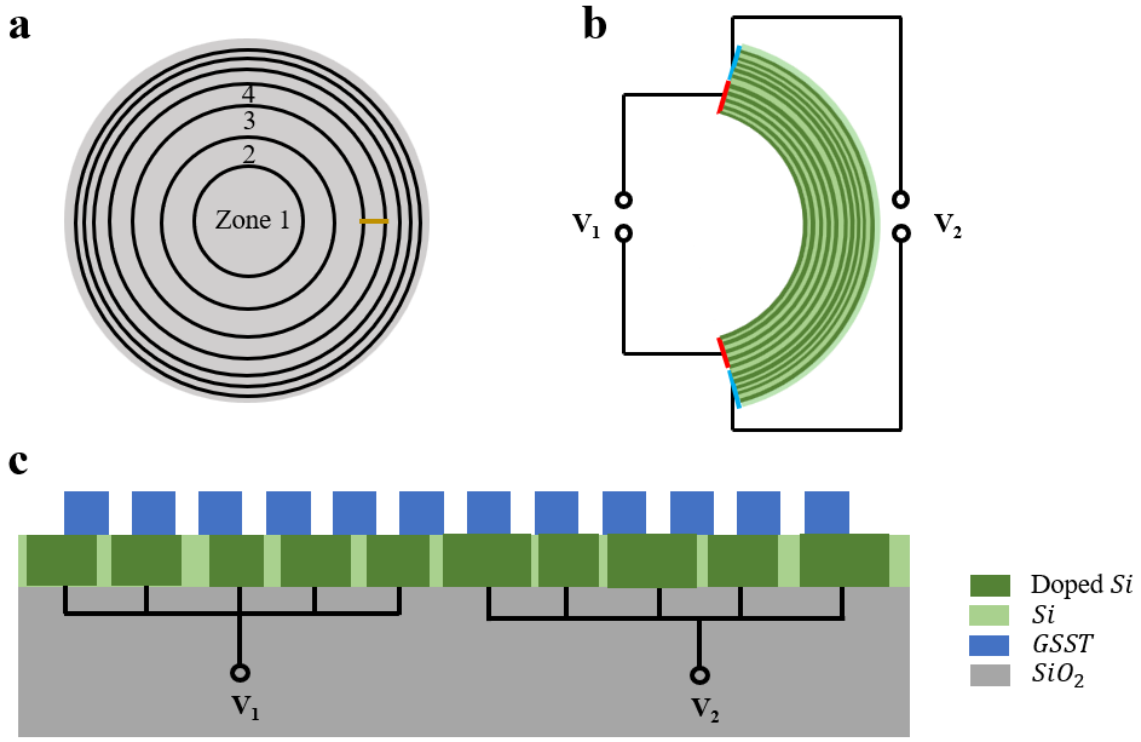

Figure 6-7: (a) Schematic illustration of the varifocal metalens with different zone areas. (The orange line represents the zone shown in Figures (b)-(c)). (b) Top and (c) cross-sectional view of the heater design in one zone area.

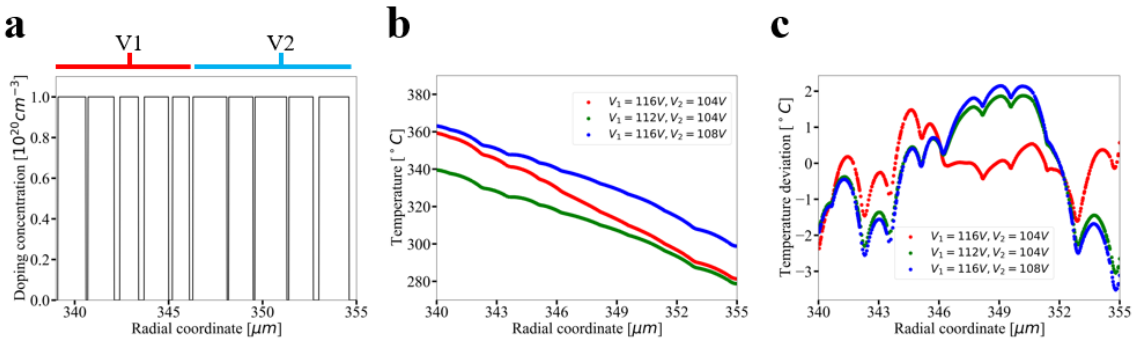

Figure 6-8: (a) Doping profile of the heaters. (b)-(c) (b)Temperature profiles and (c)temperature deviation from the ideal linear profiles across the zone with three different pairs of voltages applied to the two electrodes.

Table 6.2: Position of the zone edges

Zone number	1	2	3	4	5	6
Inner radius [μm]	0	103	144	177	205	229
Outer radius [μm]	103	144	177	205	229	251
Zone number	7	8	9	10	11	12
Inner radius [μm]	251	270	290	307	324	339
Outer radius [μm]	270	290	307	324	339	355
Zone number	13	14	15	16	17	18
Inner radius [μm]	355	369	384	396	410	422
Outer radius [μm]	369	384	396	410	422	436
Zone number	19	20	21	22	23	
Inner radius [μm]	436	447	459	471	481	
Outer radius [μm]	447	459	471	481	493	

Table 6.3: Doping profile of the optimized heaters

Doped region number	1	2	3	4	5
Start radius [μm]	339.1	340.7	342.4	343.7	345.2
End radius [μm]	340.6	342.1	343.4	345.0	346.1
Doped region number	6	7	8	9	10
Start radius [μm]	346.3	348.2	349.6	351.4	353.0
End radius [μm]	348.1	349.5	351.3	352.7	354.6

The optical phase profile of the varifocal metalens does not assume the classical hyperbolic function; instead, it is numerically optimized at each focal length by adjusting the applied voltage on each heater (and hence the optical phase gradient in each zone). Temperature distribution of the metalens is determined by the 23 temperature pairs $T_{i,j}$, where i denotes the index of the zone, j=1,2 denotes the temperature at the inner (j=1) and outer (j=2) edges of the zone. A linear temperature gradient is assumed within the zone area, which is fulfilled by the heater design with varying doped channel widths. Therefore, the temperature distribution in zone i is expressed as follow.

$$T_i(r) = \frac{T_{i,1} \cdot (r_{i,2} - r) + T_{i,2} \cdot (r - r_{i,1})}{r_{i,2} - r_{i,1}} \tag{6.1}$$

The temperature distribution is mapped to phase delay and transmittance utilizing the phase response of GSST meta-atom shown in Fig. 6-6b in the main text. Finally, Kirchhoff diffraction integral is used to calculate the FOM, which is defined as the on-axis intensity at the focal plane.

DS algorithm is used to optimize the temperature pairs $T_{i,j}$ to obtain the optimum focusing performance of a certain focal length. To start with, temperatures in the 280 °C - 360 °C range are divided into 40 discrete values with 2 °C resolution. All pairs $T_{i,j}$ have the temperature randomly selected from these values as the initial distribution. The algorithm then iterates through all the pairs, every time randomly selects one pair i that has not been optimized before, searches through all the 40×40 possible candidates of $T_{i,j=1,2}$, and keeps the ones that yields maximum FOM. This process is repeated several times until the improvement per iteration falls below 0.1%.

By controlling the voltages applied to each heater, the focal length f of the active metalens can be continuously tuned in the range of 4 – 10 mm. Fig. 6-9 uses $f = 6mm$ as an example to illustrate the design. The optimized radial temperature distribution and corresponding phase profile of the metalens are plotted in Figs. 6-9a-b, where the phase profile is inferred from the temperature distribution using data from Fig. 6-6b. The Kirchhoff diffraction integral is used to simulate the transverse intensity profile

on the image plane and along the optical axis, as shown in Figs. 6-9c-d, respectively. The focal spot has a full-width-at-half maximum (FWHM) of 13.2 μm. The focusing efficiency, defined as the encircled power of the focal spot within a diameter equaling to 5 times the focal spot FWHM, is 50.4%. In the efficiency calculation, we take into account the transmittance of the GSST meta-atoms according to their crystallization fraction following Fig. 6-9b. The Strehl ratio, defined as the ratio of the peak intensity on the focal plane to that of an ideal aberration-free lens with the same f-number and total bulk transmission power, is 0.79.

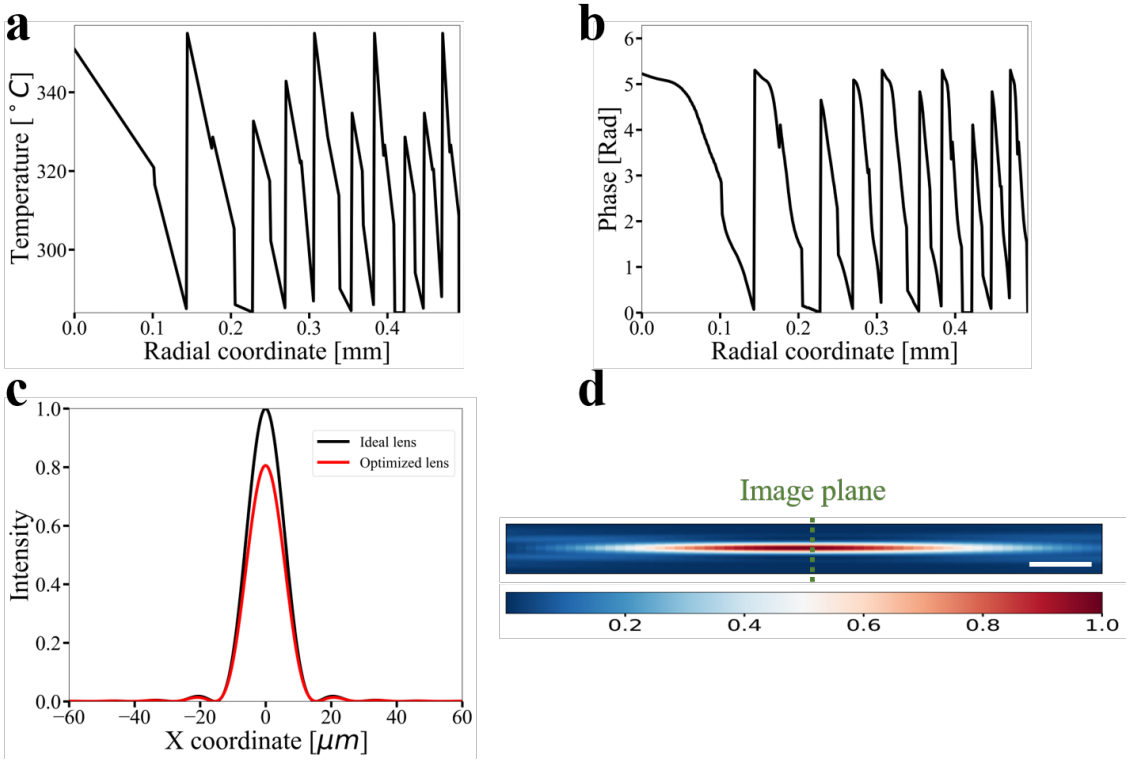

Figure 6-9: (a, b) Optimized (a) temperature and (b) phase delay profiles of the varifocal metalens when tuning to a focal length of 6 mm. Linear temperature gradient is assumed within the zone area. (c, d) Intensity profiles of the focal spot along the (c) transverse and (d) longitudinal directions. The focal spot profile of ideal aberration-free lens with same size and focal length is also shown for comparison. (Scale bar: 100 μm).

Using similar procedures, we further characterize the focusing performance of the varifocal metalens across the entire 4 – 10 mm focal length range. The FWHM, focusing efficiency, and Strehl ratio are plotted in Fig. 6-10 as red dots, which confirms near

diffraction-limited performance of the lens across the varifocal tuning range. Several examples of transverse and longitudinal intensity profiles of the focal spots at different focal lengths in the 4 – 10 mm range are shown in Fig. 6-11. To understand the possible pathways for further performance enhancement, the plots also include the focusing performance of an 'ideal' varifocal metalens (blue dots) with 100% meta-atom transmittance and linear optical phase profiles within each zone but an otherwise identical design. The comparison indicates that considerable performance improvement is expected with streamlined meta-atom designs tapping into more geometric degrees of freedom[202], reduced material absorption, and larger optical thickness, as well as more sophisticated heater architectures to better approximate the linear phase profiles.

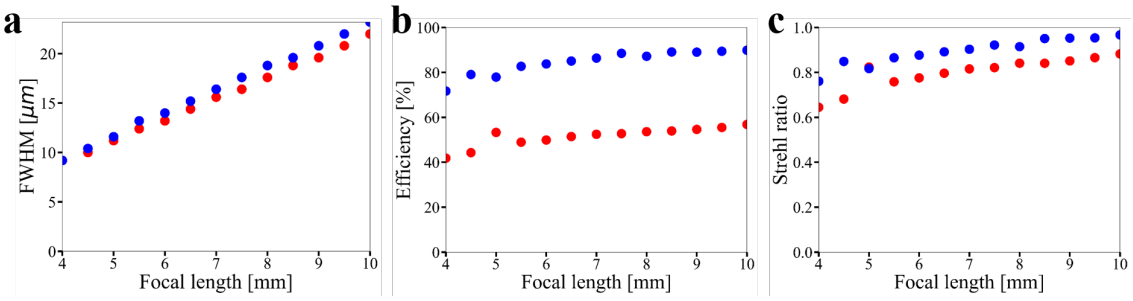

Figure 6-10: Focusing performance characterization of the varifocal metalens. (a) FWHM, (b) focusing efficiency, and (c) Strehl ratio of the metalens as a function of the focal length. (Red dots: actual meta-atom design; blue dots: perfect meta-atom design with unity transmittance and linear phase delay gradient in the zone area.)

The design in general exhibit a trade-off between the number of phase-gradient modulation zones and the focusing performance. Understandably, more zones allow more degrees of freedom in phase profile tuning to attain better performance, albeit at the expense of more complicated metasurface switching architectures. We also notice that the varifocal lens tends to perform better at longer focal length (i.e., larger f-numbers). This is because lenses with smaller f-number require Fourier components with a wider range of spatial frequencies to synthesize, which become more difficult with a fixed number of phase-gradient modulation zones.

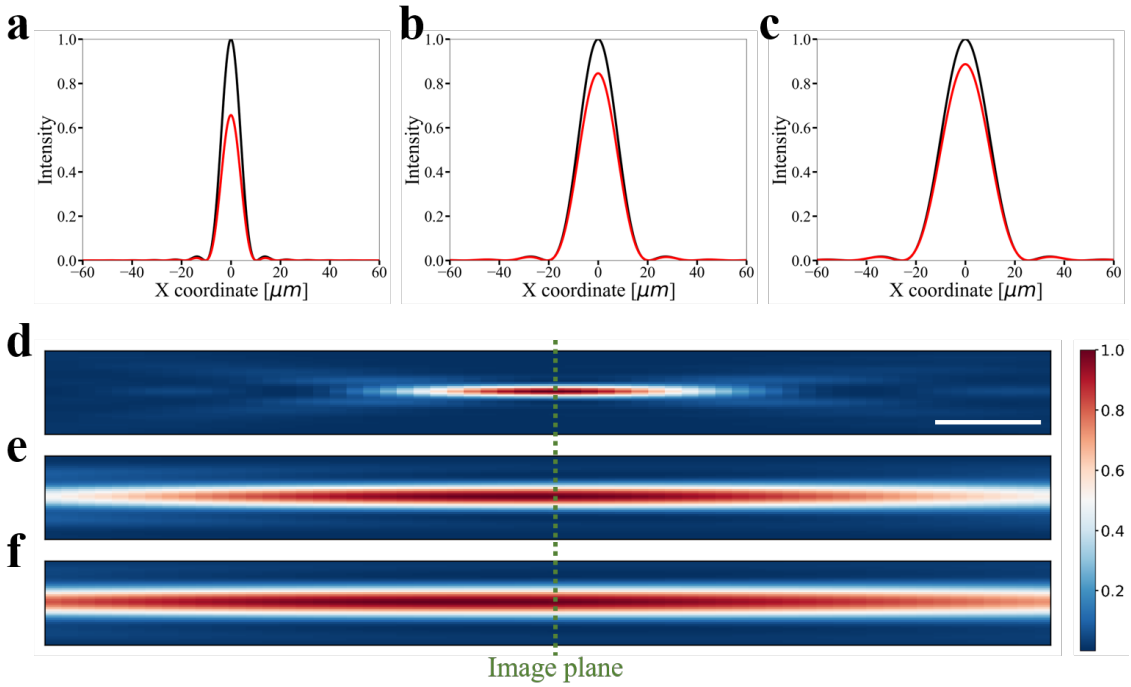

Figure 6-11: (a-c) Transverse intensity profiles of the focal spots with focal length of (a) 4 mm, (b) 8 mm, and (c) 10 mm. (Red lines: optimized lens; black lines: ideal aberration-free lens of same size and focal length). (d-f) Longitudinal intensity profiles of the focal spots with focal length of (d) 4 mm, (e) 8 mm, and (f) 10 mm. (Scale bar: 100 μm).

6.4 summary

This chapter has explored the potential of utilizing PCMs to design reconfigurable metasurfaces. By leveraging the unique properties of PCMs, such as their reversible phase transitions and tunable optical properties, it has been possible to achieve dynamic control over the electromagnetic response of metasurfaces.

Leveraging the proposed non-mechanical zoom lens architecture in the last chapter, we further developed and experimentally realized phase-change metasurfaces to achieve optical zoom at mid-IR wavelength. The same 10x zoom ratio can be realized through the switching of GSST between amorphous and crystalline states.

We then challenge the conventional wisdom that continuous tuning of metasurfaces necessitates individual tuning of meta-atoms by demonstrating a new tuning scheme modulating the phase gradient rather than single-point phase values. The paradigm was numerically validated with a continuous tunable varifocal metalens design based on optical PCMs. The design leverages doped silicon heater pairs to generate desired temperature differentials in a set of concentric zones, which translates to variable optical phase gradients within the zones. The design further leverages only 23 phase-gradient modulation zones to achieve continuous varifocal tuning in a metalens containing almost half a million individual meta-atoms and 385 rows of meta-atoms along the radial direction. The phase-gradient modulation concept therefore opens up a new route to realize active reconfigurable metasurface devices with vastly simplified control architectures for their robust practical deployment.

The findings and insights obtained through this work contribute to the growing body of knowledge in the field of metasurface engineering and provide a solid foundation for future advancements and applications. The ability to dynamically control electromagnetic wave manipulation opens up exciting possibilities for the development of advanced devices and systems that can adapt and respond to changing conditions, paving the way for innovative solutions in areas ranging from communication and sensing to imaging and beyond.

Chapter 7

Summary and future work

7.1 Summary

In this thesis, we describe our work on the design and optimization of flat optic architectures for imaging and sensing applications. The design process involves building up metalens configurations and the optimization of metasurface phase profiles, which can be performed through analytical analysis or direct search algorithm. Based on the design concept and the optimization platform, we proposed a variety of metalens architectures for imaging and sensing applications, aiming to improve image quality, depth sensitivity, and better integration capability.

7.1.1 Wide field-of-view metalens

In Chapter 3, we describe the design technique for WFOV metalenses. We start with proposing an analytical solution to optimize the phase profile of the WFOV metasurface, we then mathematically prove that telecentric configuration reduces image aberration, and relates image quality to the configurational parameters of the structure.

Based on the analytical optimization platform, we experimentally demonstrate a WFOV metalens working in the 10.6 μm wavelength LWIR band using all-Si meta-atoms fabricated with photolithography and DRIE. The metalens shows diffraction-

limited performance across the designed FOV of 140°. We further prove that the metalens shows broadband imaging performance through ambient thermal heating.

We then demonstrate a metalens that features both WFOV and broad bandwidth imaging capability in the near-infrared. The phase profile of the metasurface was optimized through the DS algorithm. The proposed metalens shows near-180° FOV in the 1 - 1.2 μm wavelength range with minimal longitudinal and transverse focal shifts.

Finally, we replace the front aperture of the WFOV metalens with a metasurface of cubic phase to improve the DOF of the imaging system. The EDOF WFOV metalens doublet shows near-180° FOV and EDOF in the object distance of 3 - 10 mm.

7.1.2 Metalens for 3-D depth sensing

Chapter 4 summarizes metalenses for 3-D depth sensing. Both passive and active depth sensing techniques have been discussed, which are suitable for different scenarios. For passive depth sensing, we start with designing two identical WFOV metalenses working in the visible following the design concept in Chapter 3, we then mount the two metalenses along the horizontal direction to construct stereo camera. We built up the custom algorithm to calibrate the distorted image from the fisheye lens, and the WFOV object depth can be inferred from the lateral shift between the two captured images. We then show a single element DH metalens for monocular passive depth sensing using polarization-multiplexing, which we elaborate in Chapter 5.

For active depth sensing, we propose both single-layer metasurface and metasurface doublet dot projectors optimized through analytical solutions. We mathematically prove that the optimum phase profile of the single-layer metasurface dot projector in the small light source divergence angle limit adopts a quadratic phase profile. We then use both diffraction integral and ray-tracing techniques to analyze the quality of the projected beams. Assuming the divergence angle of VCSEL to be 20° and wavelength of 940 nm, the projected beam shows diffraction-limited performance across the 140° FOV. However, the projection angle with the VCSEL position

adopts a sine relationship, and therefore the projected pattern shows large distortion at the edge of the projected pattern.

We then prove that the relationship between projection angle and VCSEL position can be customized through the utilization of metasurface doublet. We optimize the phase profiles of the two metasurfaces through an analytical solution, and characterize the quality of the projected beams through a similar approach. In the same condition as the single-layer metasurface, the projected beam of metasurface doublet shows near diffraction-limited performance across the 120° FOV. The projection angle adopts a linear relationship as the VCSEL position, and therefore the projected pattern shows vanished distortion.

7.1.3 Reconfigurable metalens

In Chapter 5 and Chapter 6, we detail our reconfigurable metasurface design for imaging and sensing in both visible and near IR. Chapter 5 elaborates on the tuning mechanism of polarization-multiplexing, where polarization-dependent phase delay response is achieved through tailoring the dimensions of rectangular meta-atoms. Based on the design concept, we first show a metalens with DH PSF, the phase profile of the metalens was optimized using DS algorithm. Through polarization-multiplexing, two independent DH features can be integrated into a single metasurface with DH PSFs rotating in the opposite direction under orthogonal polarized incident light. Through image deconvolution, depth information can be inferred by comparing the rotation angle of the PSFs in two polarization states. The DH metalens design serves as another type of passive depth sensing technique, and we experimentally implement it at 635 nm wavelength with the depth sensing range of 45 - 212 mm and rotation angles of up to 80°.

We then demonstrate a reconfigurable parfocal zoom metalens using metasurface doublet. Two independent phase profiles of each of the metasurface with converging and diverging focusing power in different polarization states can be realized through polarization-multiplexing in the visible. The design concept was experimentally confirmed through the implement of a zoom lens working at 670 nm wavelength, the

zoom lens shows 10x zoom ratio with 4° FOV in telephoto mode and 40° FOV in wide-angle mode, both of them have near diffraction-limited performance across the entire FOV.

In Chapter 6, we introduce another reconfiguration mechanism through utilization of phase change materials GSST. Large refractive index difference and low absorption are featured when switching between amorphous and crystalline states, the GSST meta-atoms therefore exhibit entire 0 - 2π phase tuning range with high transmittance, and the phase profile of the metasurface can be controlled through the heating of meta-atoms. We demonstrate two metasurface architectures for different applications in the mid IR. The first design is a reconfigurable parfocal zoom metalens based on the same concept as in Chapter 5, but the tuning mechanism and working spectrum range are different. As a proof of concept, we show a GSST zoom lens with 5.2 μm incident beam and 10x zoom ratio. Effectiveness of the concept was validated through the focal spot characterization in both states.

Finally, we present a varifocal zoom lens with continuously tunable focal length in the 4 - 10 mm range. The entire metasurface is divided into 23 zones, each zone has silicon heater beneath with optimized doping profiles. By controlling the voltage applied to the two electrodes connected to each of the heater, arbitrary linear temperature gradient can be established within each zone area, which can be used to control the optical phase gradient of the GSST metasurface within the zone. The phase profile of the metasurface in each focal length states can be optimized through a revised version of DS algorithm by optimizing the voltage applied to each electrode. The varifocal metalens shows diffraction-limited focusing performance and continuous tunability in the entire tuning range.

7.2 Future work

7.2.1 Metasurfaces for two photon polymerization

Apart from imaging and sensing, the arbitrary wavefront control of the metasurface can be utilized to substitute the conventional refractive lens in various technologies. For example, metasurfaces can be used as the objective lens in the two photon polymerization (TPP) system, and therefore dramatically reduces the size and cost of the TPP setup. Moreover, DS algorithm can be utilized to tailor the shape of the PSF, and therefore arbitrary-shaped structures can be written in a single shot instead of scanning back and forth in the in-plane direction, which improves the speed of the TPP writing process.

In general, the raising of metasurface technology can be used to substitute conventional optical system in many aspects, the integration of multiple functions into a single-layer metasurface can reduce the element count and complexity of the system. Arbitrary wavefront control also foresees non-intuitive designs not possible previously, which widens the applicable scenarios of the optical systems.

7.2.2 Free-form metasurface and inverse design algorithm

Metasurfaces are well-known to be restricted by the narrow bandwidth. Different from refractive lens where phase delay is accumulated from the propagation inside high index material, conventional metasurfaces have abrupt phase change in a thin layer, and the phase profile is controlled by the 'zone' area where meta-atom size goes from the largest to the smallest. Since the zone position only depends on the geometry configuration, the phase profile of the metasurface is mostly determined by the meta-atom distribution, the phase variation within the zone area at different wavelengths contribute to the aberration and the transverse/lateral focal shift.

Free-form metasurface can be utilized to increase the operational bandwidth compared to the conventional metasurface design. Instead of using regular meta-atoms and constant period, free-form metasurface sets no limit on the meta-atom shape

and their 2-D distribution. Therefore, the phase profile of the entire metasurface can be varied continuously across a large wavelength range to increase the operational bandwidth. Due to the extremely large DoF, special algorithms are implemented to design the metasurface, instead of searching meta-atoms in the predefined library for each of the unit cell as in the traditional metasurface design process. The design concept can be used in various metalens structures proposed in the thesis to improve the bandwidth coverage. Recently, inverse design algorithms have been implemented to optimize the shape of the free-form metasurface based on calculating the gradient of a few optical parameters. However, free-form metasurfaces only have tens of micro-meters size restricted by the current computational resources. Improvement of algorithms or computational technology is required to implement the design of millimeter scale metasurfaces.

7.2.3 Meta-atom coupling effect analysis

All meta-atom designs in the thesis use the unit-cell approach, where the cylindrical, rectangular, or free-form meta-atoms have a fixed period, and the lateral dimensions of the meta-atoms are used to control the optical phase delay. In the approach, periodic boundary condition is assumed in the RCWA/FDTD simulations to obtain the phase delay of the single meta-atom. This assumption, however, deviates from the actual case where the neighboring meta-atoms are usually of different sizes.

The deviation of the periodic boundary condition depends on the strength of the coupling effect. Therefore, the fill-factor of the meta-atom is usually set away from unity to reduce the coupling effect. It becomes more significant when comes to large NA metalens, as the phase gradient and the meta-atom size gradient increases with diffraction angle. This coupling effect can be taken into account by analyze the local distribution of the meta-atoms, where the phase delay of the meta-atom not only depends on its shape and period, but also depends on its nearest or even second-nearest neighbors. However, considering the extremely large number of meta-atoms on the metasurface, this analysis is restricted by the computational resources, and cannot be performed over the entire metasurface. Some approximations can

be implemented though, for example, Arbabi *et al*[357] proposed a grating average method to take into account the coupling effect and increase the efficiency of high NA metalenses. Similar procedure can be applied to the metalens architectures introduced in the thesis when efficiency is considered a critical factor.

7.2.4 Angular response of meta-atoms

In the thesis, the amplitude and phase delay of the meta-atoms are simulated under normal incidence. While the phase variation as a function of incident angle is weak for most applications, the incident angle in air for WFOV metalens configurations can be as large as 90°, where the angular response of meta-atoms is non-negligible and contributes to phase deviation. Fortunately, light with different incident angles is separated by the aperture and incident onto different proportions of the metasurface. Therefore, for a specific metasurface position, the meta-atoms only cover a small incident angle range, and can be optimized accordingly.

Apart from incident angle, diffraction angle also plays the role of varying the amplitude and phase delay response of the meta-atoms. Since periodic boundary condition is applied in the simulation, the obtained optical response corresponds to the zeros order with normal diffraction angle. This again deviates from the actual situation where the first order diffraction is critical if regarding the metasurface as the stitching of group of gratings. In this sense, the angular response of metasurface is another aspect of the coupling effect, and similar procedures as in the last section can be utilized to improve the diffraction efficiency.

Bibliography

[1] Mikhail Y Shalaginov, Sensong An, Fan Yang, Peter Su, Dominika Lyzwa, Anuradha M Agarwal, Hualiang Zhang, Juejun Hu, and Tian Gu. Single-element diffraction-limited fisheye metalens. *Nano Letters*, 20(10):7429–7437, 2020.

[2] Yifei Zhang, Carlos Ríos, Mikhail Y Shalaginov, Mo Li, Arka Majumdar, Tian Gu, and Juejun Hu. Myths and truths about optical phase change materials: A perspective. *Applied Physics Letters*, 118(21):210501, 2021.

[3] Meiyan Pan, Yifei Fu, Mengjie Zheng, Hao Chen, Yujia Zang, Huigao Duan, Qiang Li, Min Qiu, and Yueqiang Hu. Dielectric metalens for miniaturized imaging systems: progress and challenges. *Light: Science & Applications*, 11 (1):195, 2022.

[4] Xiujuan Zou, Gaige Zheng, Quan Yuan, Wenbo Zang, Run Chen, Tianyue Li, Lin Li, Shuming Wang, Zhenlin Wang, and Shining Zhu. Imaging based on metalenses. *PhotoniX*, 1(1):1–24, 2020.

[5] Shuming Wang, Pin Chieh Wu, Vin-Cent Su, Yi-Chieh Lai, Mu-Ku Chen, Hsin Yu Kuo, Bo Han Chen, Yu Han Chen, Tzu-Ting Huang, Jung-Hsi Wang, Ray-Ming Lin, Chieh-Hsiung Kuan, Tao Li, Zhenlin Wang, Shining Zhu, and Din Ping Tsai. A broadband achromatic metalens in the visible. *Nature nanotechnology*, 13(3):227–232, 2018.

[6] Beibei Xu, Hanmeng Li, Shenglun Gao, Xia Hua, Cheng Yang, Chen Chen, Feng Yan, Shining Zhu, and Tao Li. Metalens-integrated compact imaging devices for wide-field microscopy. *Advanced Photonics*, 2(6):066004–066004, 2020.

[7] Gun-Yeal Lee, Jong-Young Hong, SoonHyoung Hwang, Seokil Moon, Hyeokjung Kang, Sohee Jeon, Hwi Kim, Jun-Ho Jeong, and Byoungho Lee. Metasurface eyepiece for augmented reality. *Nature communications*, 9(1):4562, 2018.

[8] Won-Jae Joo, Jisoo Kyoung, Majid Esfandyarpour, Sung-Hoon Lee, Hyun Koo, Sunjin Song, Young-Nam Kwon, Seok Ho Song, Jun Cheol Bae, Ara Jo, et al. Metasurface-driven oled displays beyond 10,000 pixels per inch. *Science*, 370 (6515):459–463, 2020.

[9] Inki Kim, Gwanho Yoon, Jaehyuck Jang, Patrice Genevet, Ki Tae Nam, and Junsuk Rho. Outfitting next generation displays with optical metasurfaces. *ACS photonics*, 5(10):3876–3895, 2018.

[10] Jianxiong Li, Ping Yu, Shuang Zhang, and Na Liu. Electrically-controlled digital metasurface device for light projection displays. *Nature communications*, 11 (1):3574, 2020.

[11] Chunqi Jin, Mina Afsharnia, René Berlich, Stefan Fasold, Chengjun Zou, Dennis Arslan, Isabelle Staude, Thomas Pertsch, and Frank Setzpfandt. Dielectric metasurfaces for distance measurements and three-dimensional imaging. *Advanced Photonics*, 1(3):036001, 2019.

[12] Yibo Ni, Sai Chen, Yujie Wang, Qiaofeng Tan, Shumin Xiao, and Yuanmu Yang. Metasurface for structured light projection over 120 field of view. *Nano Letters*, 20(9):6719–6724, 2020.

[13] Sun Il Kim, Junghyun Park, Byung Gil Jeong, Duhyun Lee, Jungwoo Kim, Changgyun Shin, Chang Bum Lee, Tatsuhiro Otsuka, Sangwook Kim, Ki-Yeon Yang, et al. Electrically reconfigurable active metasurface for 3d distance ranging. In *2020 IEEE International Electron Devices Meeting (IEDM)*, pages 7–1. IEEE, 2020.

[14] Shane Colburn and Arka Majumdar. Single-shot three-dimensional imaging with a metasurface depth camera. *arXiv preprint arXiv:1910.12111*, 2019.

[15] Chih-Zong Deng, Ya-Lun Ho, J Kenji Clark, Takashi Yatsui, and Jean-Jacques Delaunay. Light switching with a metal-free chiral-sensitive metasurface at telecommunication wavelengths. *ACS Photonics*, 7(10):2915–2922, 2020.

[16] Mohammadreza Khorasaninejad, Francesco Aieta, Pritpal Kanhaiya, Mikhail A Kats, Patrice Genevet, David Rousso, and Federico Capasso. Achromatic metasurface lens at telecommunication wavelengths. *Nano letters*, 15(8):5358–5362, 2015.

[17] Rashmi Kumari, Shubhanshi Sharma, Shailendra Kumar Varshney, and Basudev Lahiri. Dual-channel graphene-based optical metasurface switch at telecommunication wavelengths. *JOSA B*, 40(4):753–762, 2023.

[18] Xin Chang, Mike Pivnenko, Pawan Shrestha, Weijie Wu, Wenhan Zhang, and Daping Chu. Phase shift of liquid crystal-induced resonance tuning in dielectric metasurface at telecommunication wavelength. In *High Contrast Metastructures XII*, volume 12432, pages 50–54. SPIE, 2023.

[19] Abdulrahman Ahmed Ghaleb Amer, Syarfa Zahirah Sapuan, Nasimuddin Nasimuddin, Arokiaswami Alphones, and Nabiah Binti Zinal. A comprehensive review of metasurface structures suitable for rf energy harvesting. *IEEE Access*, 8:76433–76452, 2020.

[20] Jacopo M De Ponti, Andrea Colombi, Raffaele Ardito, Francesco Braghin, Alberto Corigliano, and Richard V Craster. Graded elastic metasurface for enhanced energy harvesting. *New Journal of Physics*, 22(1):013013, 2020.

[21] Mohamed El Badawe and Omar M Ramahi. Efficient metasurface rectenna for electromagnetic wireless power transfer and energy harvesting. *Progress In Electromagnetics Research*, 161:35–40, 2018.

[22] Shuibao Qi and Badreddine Assouar. Acoustic energy harvesting based on multilateral metasurfaces. *Applied Physics Letters*, 111(24):243506, 2017.

[23] Ali Momeni, Hamid Rajabalipanah, Mahdi Rahmanzadeh, Ali Abdolali, Karim Achouri, Viktar S Asadchy, and Romain Fleury. Reciprocal metasurfaces for on-axis reflective optical computing. *IEEE Transactions on Antennas and Propagation*, 69(11):7709–7719, 2021.

[24] Hossein Babashah, Zahra Kavehvash, Somayyeh Koohi, and Amin Khavasi. Integration in analog optical computing using metasurfaces revisited: toward ideal optical integration. *JOSA B*, 34(6):1270–1279, 2017.

[25] Lei Wan, Danping Pan, Shuaifeng Yang, Wei Zhang, Alexander A Potapov, Xia Wu, Weiping Liu, Tianhua Feng, and Zhaohui Li. Optical analog computing of spatial differentiation and edge detection with dielectric metasurfaces. *Optics Letters*, 45(7):2070–2073, 2020.

[26] Yi Zhou, Wenhui Wu, Rui Chen, Wenjie Chen, Ruipin Chen, and Yungui Ma. Analog optical spatial differentiators based on dielectric metasurfaces. *Advanced Optical Materials*, 8(4):1901523, 2020.

[27] Benedikt Groever, Wei Ting Chen, and Federico Capasso. Meta-lens doublet in the visible region. *Nano letters*, 17(8):4902–4907, 2017.

[28] Amir Arbabi, Ehsan Arbabi, Seyedeh Mahsa Kamali, Yu Horie, Seunghoon Han, and Andrei Faraon. Miniature optical planar camera based on a wide-angle metasurface doublet corrected for monochromatic aberrations. *Nature communications*, 7(1):13682, 2016.

[29] Dongliang Tang, Long Chen, Jia Liu, and Xiaohu Zhang. Achromatic metasurface doublet with a wide incident angle for light focusing. *Optics Express*, 28 (8):12209–12218, 2020.

[30] Zhu Li, Changtao Wang, Yanqin Wang, Xinjian Lu, Yinghui Guo, Xiong Li, Xiaoliang Ma, Mingbo Pu, and Xiangang Luo. Super-oscillatory metasurface doublet for sub-diffraction focusing with a large incident angle. *Optics Express*, 29(7):9991–9999, 2021.

[31] Zhenyu Huang, Maosen Qin, Xiaowei Guo, Cheng Yang, and Shaorong Li. Achromatic and wide-field metalens in the visible region. *Optics Express*, 29 (9):13542–13551, 2021.

[32] Yan Liu, Qing-Yun Yu, Ze-Ming Chen, Hao-Yang Qiu, Rui Chen, Shao-Ji Jiang, Xin-Tao He, Fu-Li Zhao, and Jian-Wen Dong. Meta-objective with sub-micrometer resolution for microendoscopes. *Photonics Research*, 9(2):106–115, 2021.

[33] Dale A Buralli and G Michael Morris. Design of a wide field diffractive landscape lens. *Applied optics*, 28(18):3950–3959, 1989.

[34] Mikhail Y Shalaginov, Sensong An, Fan Yang, Peter Su, Dominika Lyzwa, Anuradha Agarwal, Hualiang Zhang, Juejun Hu, and Tian Gu. A single-layer panoramic metalens with> 170 {\deg} diffraction-limited field of view. *arXiv preprint arXiv:1908.03626*, 2019.

[35] Jacob Engelberg, Chen Zhou, Noa Mazurski, Jonathan Bar-David, Anders Kristensen, and Uriel Levy. Near-ir wide-field-of-view huygens metalens for outdoor imaging applications. *Nanophotonics*, 9(2):361–370, 2020.

[36] Augusto Martins, Kezheng Li, Juntao Li, Haowen Liang, Donato Conteduca, Ben-Hur V Borges, Thomas F Krauss, and Emiliano R Martins. On metalenses with arbitrarily wide field of view. *ACS Photonics*, 7(8):2073–2079, 2020.

[37] Fei Zhang, Mingbo Pu, Xiong Li, Xiaoliang Ma, Yinghui Guo, Ping Gao, Honglin Yu, Min Gu, and Xiangang Luo. Extreme-angle silicon infrared optics enabled by streamlined surfaces. *Advanced Materials*, 33(11):2008157, 2021.

[38] Chun-Yuan Fan, Chia-Ping Lin, and Guo-Dung J Su. Ultrawide-angle and high-efficiency metalens in hexagonal arrangement. *Scientific Reports*, 10(1):15677, 2020.

[39] Arnold Kalvach and Zsolt Szabó. Aberration-free flat lens design for a wide range of incident angles. *JOSA B*, 33(2):A66–A71, 2016.

[40] Tatiana Grulois, Guillaume Druart, Nicolas Guérineau, Arnaud Crastes, Hervé Sauer, and Pierre Chavel. Extra-thin infrared camera for low-cost surveillance applications. *Optics letters*, 39(11):3169–3172, 2014.

[41] Mingbo Pu, Xiong Li, Yinghui Guo, Xiaoliang Ma, and Xiangang Luo. Nanoapertures with ordered rotations: symmetry transformation and wide-angle flat lensing. *Optics Express*, 25(25):31471–31477, 2017.

[42] Cong Chen, Panpan Chen, Jianxin Xi, Wanxia Huang, Kuanguo Li, Li Liang, Fenghua Shi, and Jianping Shi. On-chip monolithic wide-angle field-of-view metalens based on quadratic phase profile. *AIP Advances*, 10(11):115213, 2020.

[43] Wen-peng Zhang, Fei Liang, Ya-rong Su, Ke Liu, Ming-jun Tang, Ling Li, Zheng-wei Xie, and Wu-ming Liu. Numerical simulation research of wide-angle beam steering based on catenary shaped ultrathin metalens. *Optics Communications*, 474:126085, 2020.

[44] Yang Liu, Jianhao Zhang, Xavier Le Roux, Eric Cassan, Delphine Marris-Morini, Laurent Vivien, Carlos Alonso-Ramos, and Daniele Melati. Broadband behavior of quadratic metalenses with a wide field of view. *arXiv preprint arXiv:2206.03750*, 2022.

[45] Inki Kim, Renato Juliano Martins, Jaehyuck Jang, Trevon Badloe, Samira Khadir, Ho-Youl Jung, Hyeongdo Kim, Jongun Kim, Patrice Genevet, and Junsuk Rho. Nanophotonics for light detection and ranging technology. *Nature nanotechnology*, 16(5):508–524, 2021.

[46] Babak Mirzapourbeinekalaye, Mahdad Mansouree, Andrew McClung, and Amir Arbabi. Fast and wide-angle integrated laser beam scanner enabled by a metalens. In *High Contrast Metastructures XII*, page PC124320Q. SPIE, 2023.

[47] You-Chia Chang, Min Chul Shin, Christopher T Phare, Steven A Miller, Eujae Shim, and Michal Lipson. 2d beam steerer based on metalens on silicon photonics. *Optics Express*, 29(2):854–864, 2021.

[48] Yinghui Guo, Xiaoliang Ma, Mingbo Pu, Xiong Li, Zeyu Zhao, and Xiangang Luo. High-efficiency and wide-angle beam steering based on catenary optical fields in ultrathin metalens. *Advanced Optical Materials*, 6(19):1800592, 2018.

[49] Pin Chieh Wu, Ragip A Pala, Ghazaleh Kafaie Shirmanesh, Wen-Hui Cheng, Ruzan Sokhoyan, Meir Grajower, Muhammad Z Alam, Duhyun Lee, and Harry A Atwater. Dynamic beam steering with all-dielectric electro-optic iii–v multiple-quantum-well metasurfaces. *Nature communications*, 10(1):3654, 2019.

[50] Zhizhang Wang, Jitao Ji, Xin Ye, Yuxin Chen, Xueyun Li, Wange Song, Bin Fang, Ji Chen, Shining Zhu, and Tao Li. On-chip integration of metasurface-doublet for optical phased array with enhanced beam steering. *Nanophotonics*, 2023.

[51] Hongliang Li, Changyi Zhou, Woo-Bin Lee, Duk-Yong Choi, and Sang-Shin Lee. Flat telescope based on an all-dielectric metasurface doublet enabling polarization-controllable enhanced beam steering. *Nanophotonics*, 11(2):405–413, 2021.

[52] Giuseppe Emanuele Lio and Antonio Ferraro. Lidar and beam steering tailored by neuromorphic metasurfaces dipped in a tunable surrounding medium. In *Photonics*, volume 8, page 65. MDPI, 2021.

[53] Gyeongtae Kim, Yeseul Kim, Jooyeong Yun, Seong-Won Moon, Seokwoo Kim, Jaekyung Kim, Junkyeong Park, Trevon Badloe, Inki Kim, and Junsuk Rho. Metasurface-driven full-space structured light for three-dimensional imaging. *Nature Communications*, 13(1):5920, 2022.

[54] Qiu-Hua Wang, Pei-Nan Ni, Yi-Yang Xie, Qiang Kan, Pei-Pei Chen, Pan Fu, Jun Deng, Tai-Lai Jin, Hong-Da Chen, Ho Wai Howard Lee, et al. On-chip

generation of structured light based on metasurface optoelectronic integration. *Laser & Photonics Reviews*, 15(3):2000385, 2021.

[55] Ahmed H Dorrah and Federico Capasso. Tunable structured light with flat optics. *Science*, 376(6591):eabi6860, 2022.

[56] Yuning Wu, Zhiwei Shi, Huan Jiang, and Yaohua Deng. Multi-wavelength spot-array beams based on tunable dammann grating metasurface. In *Photonics*, volume 10, page 141. MDPI, 2023.

[57] Yifan Zhao, Jing Du, Jinrun Zhang, Li Shen, and Jian Wang. Generating structured light with phase helix and intensity helix using reflection-enhanced plasmonic metasurface at 2 μ m. *Applied Physics Letters*, 112(17):171103, 2018.

[58] Elyas Bayati, Andrew Wolfram, Shane Colburn, Luocheng Huang, and Arka Majumdar. Design of achromatic augmented reality visors based on composite metasurfaces. *Applied Optics*, 60(4):844–850, 2021.

[59] Weitao Song, Xinan Liang, Shiqiang Li, Parikshit Moitra, Xuewu Xu, Emmanuel Lassalle, Yuanjin Zheng, Yongtian Wang, Ramón Paniagua-Domínguez, and Arseniy I Kuznetsov. Retinal projection near-eye displays with huygens' metasurfaces. *Advanced Optical Materials*, 11(5):2202348, 2023.

[60] Wen-Qing Chen, Da-Sen Zhang, Shang-Yu Long, Zhen-Zhen Liu, and Jun-Jun Xiao. Nearly dispersionless multicolor metasurface beam deflector for near eye display designed by a physics-driven deep neural network. *Applied Optics*, 60 (13):3947–3953, 2021.

[61] Weitao Song, Xinan Liang, Shiqiang Li, Dongdong Li, Ramón Paniagua-Domínguez, Keng Heng Lai, Qunying Lin, Yuanjin Zheng, and Arseniy I Kuznetsov. Large-scale huygens' metasurfaces for holographic 3d near-eye displays. *Laser & Photonics Reviews*, 15(9):2000538, 2021.

[62] Shoufeng Lan, Xueyue Zhang, Mohammad Taghinejad, Sean Rodrigues, Kyu-Tae Lee, Zhaocheng Liu, and Wenshan Cai. Metasurfaces for near-eye augmented reality. *ACS Photonics*, 6(4):864–870, 2019.

[63] Shang-Yu Long, Ding-Yue Zhang, Zhen-Zhen Liu, and Jun-Jun Xiao. Colorful see-through near-eye display based on all-dielectric metasurface. In *Optics Frontier Online 2020: Optics Imaging and Display*, volume 11571, pages 32–39. SPIE, 2020.

[64] Xinan Liang, Weitao Song, Shiqiang Li, Dongdong Li, Ramoòn Paniagua-Domínguez, Yefeng Yu, Keng Heng Lai, Qunying Lin, Xuewu Xu, Yuanjin Zheng, et al. Dielectric huygens' metasurfaces for holographic projection and 3d near-eye displays applications. In *Digital Holography and Three-Dimensional Imaging*, pages DF2C–2. Optica Publishing Group, 2021.

[65] Mikhail Y Shalaginov, Sensong An, Yifei Zhang, Fan Yang, Peter Su, Vladimir Liberman, Jeffrey B Chou, Christopher M Roberts, Myungkoo Kang, Carlos Rios, et al. Reconfigurable all-dielectric metalens with diffraction-limited performance. *Nature communications*, 12(1):1225, 2021.

[66] Fan Yang, Hung-I Lin, Mikhail Y Shalaginov, Katherine Stoll, Sensong An, Clara Rivero-Baleine, Myungkoo Kang, Anuradha Agarwal, Kathleen Richardson, Hualiang Zhang, et al. Reconfigurable parfocal zoom metalens. *Advanced Optical Materials*, 10(17):2200721, 2022.

[67] Ramon Paniagua-Dominguez, Ye Feng Yu, Egor Khaidarov, Sumin Choi, Victor Leong, Reuben M Bakker, Xinan Liang, Yuan Hsing Fu, Vytautas Valuckas, Leonid A Krivitsky, et al. A metalens with a near-unity numerical aperture. *Nano Letters*, 18(3):2124–2132, 2018.

[68] Haowen Liang, Qiaoling Lin, Xiangsheng Xie, Qian Sun, Yin Wang, Lidan Zhou, Lin Liu, Xiangyang Yu, Jianying Zhou, Thomas F Krauss, et al. Ultrahigh numerical aperture metalens at visible wavelengths. *Nano Letters*, 18(7):4460–4466, 2018.

[69] David Sell, Jianji Yang, Sage Doshay, Rui Yang, and Jonathan A Fan. Large-angle, multifunctional metagratings based on freeform multimode geometries. *Nano letters*, 17(6):3752–3757, 2017.

[70] Fan Yang, Mikhail Y. Shalaginov, Hung-I Lin, Sensong An, Anu M. Agarwal, Hualiang Zhang, Clara Rivero-Baleine, Tian Gu, and Juejun Hu. Wide field-of-view metalens: a tutorial. *Advanced Photonics*, 5(3):033001, 2023. doi: 10.1117/1.AP.5.3.033001. URL `https://doi.org/10.1117/1.AP.5.3.033001`.

[71] Fan Yang, Sensong An, Mikhail Y Shalaginov, Hualiang Zhang, Juejun Hu, and Tian Gu. Understanding wide field-of-view flat lenses: an analytical solution [Invited]. *Chinese Optics Letters*, 21(2):023601, 2023.

[72] Joon-Suh Park, Shuyan Zhang, Alan She, Wei Ting Chen, Peng Lin, Kerolos MA Yousef, Ji-Xin Cheng, and Federico Capasso. All-glass, large metalens at visible wavelength using deep-ultraviolet projection lithography. *Nano Letters*, 19(12):8673–8682, 2019.

[73] Ting Hu, Qize Zhong, Nanxi Li, Yuan Dong, Zhengji Xu, Yuan Hsing Fu, Dongdong Li, Vladimir Bliznetsov, Yanyan Zhou, Keng Heng Lai, et al. Cmos-compatible a-si metalenses on a 12-inch glass wafer for fingerprint imaging. *Nanophotonics*, 9(4):823–830, 2020.

[74] Zhengji Xu, Nanxi Li, Yuan Dong, Yuan Hsing Fu, Ting Hu, Qize Zhong, Yanyan Zhou, Dongdong Li, Shiyang Zhu, and Navab Singh. Metasurface-based subtractive color filter fabricated on a 12-inch glass wafer using a cmos platform. *Photonics Research*, 9(1):13–20, 2021.

[75] Seyedeh Mahsa Kamali, Ehsan Arbabi, Amir Arbabi, Yu Horie, and Andrei Faraon. Highly tunable elastic dielectric metasurface lenses. *Laser & Photonics Reviews*, 10(6):1002–1008, 2016.

[76] Alan She, Shuyan Zhang, Samuel Shian, David R Clarke, and Federico Capasso. Adaptive metalenses with simultaneous electrical control of focal length, astigmatism, and shift. *Science advances*, 4(2):eaap9957, 2018.

[77] Ehsan Arbabi, Amir Arbabi, Seyedeh Mahsa Kamali, Yu Horie, Mohammad-Sadegh Faraji-Dana, and Andrei Faraon. Mems-tunable dielectric metasurface lens. *Nature communications*, 9(1):812, 2018.

[78] Shaowei He, Huimin Yang, Yunhui Jiang, Wenjun Deng, and Weiming Zhu. Recent advances in mems metasurfaces and their applications on tunable lens. *Micromachines*, 10(8):505, 2019.

[79] Zang Guanxing, Ziji Liu, Wenjun Deng, and Weiming Zhu. Reconfigurable metasurfaces with mechanical actuations: towards flexible and tunable photonic devices. *Journal of Optics*, 23(1):013001, 2020.

[80] Paul CV Thrane, Chao Meng, Fei Ding, and Sergey I Bozhevolnyi. Mems tunable metasurfaces based on gap plasmon or fabry–pérot resonances. *Nano Letters*, 22(17):6951–6957, 2022.

[81] Christopher A Dirdal, Paul CV Thrane, Firehun T Dullo, Jo Gjessing, Anand Summanwar, and Jon Tschudi. Mems-tunable dielectric metasurface lens using thin-film pzt for large displacements at low voltages. *Optics Letters*, 47(5): 1049–1052, 2022.

[82] Manuel Decker, Christian Kremers, Alexander Minovich, Isabelle Staude, Andrey E Miroshnichenko, Dmitry Chigrin, Dragomir N Neshev, Chennupati Jagadish, and Yuri S Kivshar. Electro-optical switching by liquid-crystal controlled metasurfaces. *Optics express*, 21(7):8879–8885, 2013.

[83] Aharon Weiss, Christian Frydendahl, Jonathan Bar-David, Roy Zektzer, Eitan Edrei, Jacob Engelberg, Noa Mazurski, Boris Desiatov, and Uriel Levy. Tunable metasurface using thin-film lithium niobate in the telecom regime. *ACS Photonics*, 9(2):605–612, 2022.

[84] Robin Kaissner, Jianxiong Li, Wenzheng Lu, Xin Li, Frank Neubrech, Jianfang Wang, and Na Liu. Electrochemically controlled metasurfaces with high-contrast switching at visible frequencies. *Science Advances*, 7(19):eabd9450, 2021.

[85] Mohsen Rahmani, Lei Xu, Andrey E Miroshnichenko, Andrei Komar, Rocio Camacho-Morales, Haitao Chen, Yair Zárate, Sergey Kruk, Guoquan Zhang, Dragomir N Neshev, et al. Reversible thermal tuning of all-dielectric metasurfaces. *Advanced Functional Materials*, 27(31):1700580, 2017.

[86] M Bosch, MR Shcherbakov, Z Fan, and G Shvets. Polarization states synthesizer based on a thermo-optic dielectric metasurface. *Journal of Applied Physics*, 126 (7):073102, 2019.

[87] Tomer Lewi, Nikita A Butakov, and Jon A Schuller. Thermal tuning capabilities of semiconductor metasurface resonators. *Nanophotonics*, 8(2):331–338, 2018.

[88] Tomer Lewi, Nikita A Butakov, Hayden A Evans, Mark W Knight, Prasad P Iyer, David Higgs, Hamid Chorsi, Juan Trastoy, Javier Del Valle Granda, Ilya Valmianski, et al. Thermally reconfigurable meta-optics. *IEEE Photonics Journal*, 11(2):1–16, 2019.

[89] Maxim R Shcherbakov, Sheng Liu, Varvara V Zubyuk, Aleksandr Vaskin, Polina P Vabishchevich, Gordon Keeler, Thomas Pertsch, Tatyana V Dolgova, Isabelle Staude, Igal Brener, et al. Ultrafast all-optical tuning of direct-gap semiconductor metasurfaces. *Nature communications*, 8(1):1–6, 2017.

[90] Honglei Cai, Qiuping Huang, Xiang Hu, Yu Liu, Zhengping Fu, Yi Zhao, Hongchuan He, and Yalin Lu. All-optical and ultrafast tuning of terahertz plasmonic metasurfaces. *Advanced Optical Materials*, 6(14):1800143, 2018.

[91] Yuze Hu, Tian Jiang, Junhu Zhou, Hao Hao, Hao Sun, Hao Ouyang, Mingyu Tong, Yuxiang Tang, Han Li, Jie You, et al. Ultrafast terahertz frequency and phase tuning by all-optical molecularization of metasurfaces. *Advanced Optical Materials*, 7(22):1901050, 2019.

[92] Murali Subbarao and T-C Wei. Depth from defocus and rapid autofocusing: A practical approach. In *Proceedings 1992 IEEE Computer Society Conference on Computer Vision and Pattern Recognition*, pages 773–774. IEEE Computer Society, 1992.

[93] Murali Subbarao and Gopal Surya. Depth from defocus: A spatial domain approach. *International Journal of Computer Vision*, 13(3):271–294, 1994.

[94] Subhasis Chaudhuri and Ambasamudram N Rajagopalan. *Depth from defocus: a real aperture imaging approach*. Springer Science & Business Media, 1999.

[95] Yoav Y Schechner and Nahum Kiryati. Depth from defocus vs. stereo: How different really are they? *International Journal of Computer Vision*, 39(2): 141–162, 2000.

[96] Changyin Zhou, Stephen Lin, and Shree K Nayar. Coded aperture pairs for depth from defocus and defocus deblurring. *International journal of computer vision*, 93(1):53–72, 2011.

[97] Qi Guo, Zhujun Shi, Yao-Wei Huang, Emma Alexander, Cheng-Wei Qiu, Federico Capasso, and Todd Zickler. Compact single-shot metalens depth sensors inspired by eyes of jumping spiders. *Proceedings of the National Academy of Sciences*, 116(46):22959–22965, 2019.

[98] Mikhail Y Shalaginov, Hung-I Lin, Fan Yang, Drew M Weninger, Crystal Li, Anuradha M Agarwal, Juejun Hu, and Tian Gu. Metasurface-enabled wide-angle stereoscopic imaging. In *Frontiers in Optics*, pages JTu7B–2. Optica Publishing Group, 2022.

[99] Shiyu Tan, Frank Yang, Vivek Boominathan, Ashok Veeraraghavan, and Guru-raj V Naik. 3d imaging using extreme dispersion in optical metasurfaces. *ACS Photonics*, 8(5):1421–1429, 2021.

[100] Bo Huang, Wenqin Wang, Mark Bates, and Xiaowei Zhuang. Three-dimensional super-resolution imaging by stochastic optical reconstruction microscopy. *Science*, 319(5864):810–813, 2008.

[101] Manuel F Juette, Travis J Gould, Mark D Lessard, Michael J Mlodzianoski, Bhupendra S Nagpure, Brian T Bennett, Samuel T Hess, and Joerg Bewersdorf. Three-dimensional sub–100 nm resolution fluorescence microscopy of thick samples. *Nature methods*, 5(6):527–529, 2008.

[102] Yoav Shechtman, Steffen J Sahl, Adam S Backer, and William E Moerner. Optimal point spread function design for 3d imaging. *Physical review letters*, 113(13):133902, 2014.

[103] Yoav Shechtman, Lucien E Weiss, Adam S Backer, Steffen J Sahl, and WE Moerner. Precise three-dimensional scan-free multiple-particle tracking over large axial ranges with tetrapod point spread functions. *Nano letters*, 15(6):4194–4199, 2015.

[104] Yoav Shechtman, Anna-Karin Gustavsson, Petar N Petrov, Elisa Dultz, Maurice Y Lee, Karsten Weis, and WE Moerner. Observation of live chromatin dynamics in cells via 3d localization microscopy using tetrapod point spread functions. *Biomedical optics express*, 8(12):5735–5748, 2017.

[105] Sri Rama Prasanna Pavani, Michael A Thompson, Julie S Biteen, Samuel J Lord, Na Liu, Robert J Twieg, Rafael Piestun, and William E Moerner. Three-dimensional, single-molecule fluorescence imaging beyond the diffraction limit by using a double-helix point spread function. *Proceedings of the National Academy of Sciences*, 106(9):2995–2999, 2009.

[106] Michael A Thompson, Jason M Casolari, Majid Badieirostami, Patrick O Brown, and WE Moerner. Three-dimensional tracking of single mrna particles in saccharomyces cerevisiae using a double-helix point spread function. *Proceedings of the National Academy of Sciences*, 107(42):17864–17871, 2010.

[107] Mikael P Backlund, Ryan Joyner, Karsten Weis, and WE Moerner. Correlations of three-dimensional motion of chromosomal loci in yeast revealed by the double-helix point spread function microscope. *Molecular biology of the cell*, 25(22): 3619–3629, 2014.

[108] Bin Yu, Jie Yu, Weihai Li, Bo Cao, Heng Li, Danni Chen, and Hanben Niu. Nanoscale three-dimensional single particle tracking by light-sheet-based double-helix point spread function microscopy. *Applied Optics*, 55(3):449–453, 2016.

[109] Zhaojun Wang, Yanan Cai, Yansheng Liang, Xing Zhou, Shaohui Yan, Dan Dan, Piero R Bianco, Ming Lei, and Baoli Yao. Single shot, three-dimensional fluorescence microscopy with a spatially rotating point spread function. *Biomedical optics express*, 8(12):5493–5506, 2017.

[110] Bhargav Ghanekar, Vishwanath Saragadam, Dushyant Mehra, Anna-Karin Gustavsson, Aswin C Sankaranarayanan, and Ashok Veeraraghavan. Ps^2f: Polarized spiral point spread function for single-shot 3d sensing. *IEEE Transactions on Pattern Analysis and Machine Intelligence*, 2022.

[111] Chunqi Jin, Jihua Zhang, and Chunlei Guo. Metasurface integrated with double-helix point spread function and metalens for three-dimensional imaging. *Nanophotonics*, 8(3):451–458, 2019.

[112] Shane Colburn and Arka Majumdar. Metasurface generation of paired accelerating and rotating optical beams for passive ranging and scene reconstruction. *ACS Photonics*, 7(6):1529–1536, 2020.

[113] Zhiyuan Ma, Siyu Dong, Xiong Dun, Zeyong Wei, Zhanshan Wang, and Xinbin Cheng. Reconfigurable metalens with phase-change switching between beam acceleration and rotation for 3d depth imaging. *Micromachines*, 13(4):607, 2022.

[114] Zicheng Shen, Feng Zhao, Chunqi Jin, Shuai Wang, Liangcai Cao, and Yuanmu Yang. Monocular metasurface camera for passive single-shot 4d imaging. *Nature Communications*, 14(1):1035, 2023.

[115] Kazuo Tanaka. Paraxial analysis of mechanically compensated zoom lenses. 1: Four-component type. *Applied optics*, 21(12):2174–2183, 1982.

[116] R Barry Johnson and Chen Feng. Mechanically compensated zoom lenses with a single moving element. *Applied optics*, 31(13):2274–2278, 1992.

[117] Mads Demenikov, Ewan Findlay, and Andrew R Harvey. Miniaturization of zoom lenses with a single moving element. *Optics Express*, 17(8):6118–6127, 2009.

[118] Samuel Shian, Roger M Diebold, and David R Clarke. Tunable lenses using transparent dielectric elastomer actuators. *Optics express*, 21(7):8669–8676, 2013.

[119] Norio Sugiura and Shinzo Morita. Variable-focus liquid-filled optical lens. *Applied Optics*, 32(22):4181–4186, 1993.

[120] Nikolas Chronis, Gang L Liu, Ki-Hun Jeong, and Luke P Lee. Tunable liquid-filled microlens array integrated with microfluidic network. *Optics express*, 11 (19):2370–2378, 2003.

[121] Seungwan Lee, Minseog Choi, Eunsung Lee, Kyu-Dong Jung, Jong-hyeon Chang, and Woonbae Kim. Zoom lens design using liquid lens for laparoscope. *Optics Express*, 21(2):1751–1761, 2013.

[122] M Ye, M Noguchi, B Wang, and S Sato. Zoom lens system without moving elements realised using liquid crystal lenses. *Electronics letters*, 45(12):646–648, 2009.

[123] Shibiao Wei, Guiyuan Cao, Han Lin, Xiaocong Yuan, Michael Somekh, and Baohua Jia. A varifocal graphene metalens for broadband zoom imaging covering the entire visible region. *ACS nano*, 15(3):4769–4776, 2021.

[124] Yunxuan Wei, Yuxi Wang, Xing Feng, Shunyuan Xiao, Zhaokun Wang, Tie Hu, Manchen Hu, Jinwen Song, Martin Wegener, Ming Zhao, et al. Compact optical polarization-insensitive zoom metalens doublet. *Advanced Optical Materials*, 8 (13):2000142, 2020.

[125] Yuan Cui, Guoxing Zheng, Ming Chen, Yilun Zhang, Yan Yang, Jin Tao, Taotao He, and Zile Li. Reconfigurable continuous-zoom metalens in visible band. *Chinese Optics Letters*, 17(11):111603, 2019.

[126] Ning Xu, Yuan Hao, Kaiqian Jie, Shuai Qin, Hui Huang, Li Chen, Hongzhan Liu, Jianping Guo, Hongyun Meng, Faqiang Wang, et al. Electrically-driven zoom metalens based on dynamically controlling the phase of barium titanate (bto) column antennas. *Nanomaterials*, 11(3):729, 2021.

[127] Chang Wang, Yan Sun, Qiangbo Zhang, Zeqing Yu, Chenning Tao, Jinlei Zhang, Fei Wu, Rengmao Wu, and Zhenrong Zheng. Continuous-zoom bifocal metalens by mutual motion of cascaded bilayer metasurfaces in the visible. *Optics Express*, 29(17):26569–26585, 2021.

[128] Shane Colburn, Alan Zhan, and Arka Majumdar. Varifocal zoom imaging with large area focal length adjustable metalenses. *Optica*, 5(7):825–831, 2018.

[129] Zheng Liu, Zhiyuan Du, Bin Hu, Weiguang Liu, Juan Liu, and Yongtian Wang. Wide-angle moiré metalens with continuous zooming. *JOSA B*, 36(10):2810–2816, 2019.

[130] Maxwell D Aiello, Adam S Backer, Aryeh J Sapon, Janis Smits, John D Perreault, Patrick Llull, and Victor M Acosta. Achromatic varifocal metalens for the visible spectrum. *ACS Photonics*, 6(10):2432–2440, 2019.

[131] Adeel Afridi, Josep Canet-Ferrer, Laurent Philippet, Johann Osmond, Pascal Berto, and Romain Quidant. Electrically driven varifocal silicon metalens. *ACS Photonics*, 5(11):4497–4503, 2018.

[132] Yinghui Guo, Mingbo Pu, Xiaoliang Ma, Xiong Li, Ruoyu Shi, and Xiangang Luo. Experimental demonstration of a continuous varifocal metalens with large zoom range and high imaging resolution. *Applied Physics Letters*, 115(16): 163103, 2019.

[133] Yuan Luo, Cheng Hung Chu, Sunil Vyas, Hsin Yu Kuo, Yu Hsin Chia, Mu Ku Chen, Xu Shi, Takuo Tanaka, Hiroaki Misawa, Yi-You Huang, et al. Varifocal metalens for optical sectioning fluorescence microscopy. *Nano Letters*, 21(12): 5133–5142, 2021.

[134] Chun-Yuan Fan, Tsung-Jung Chuang, Kuo-Hao Wu, and Guo-Dung J Su. Electrically modulated varifocal metalens combined with twisted nematic liquid crystals. *Optics Express*, 28(7):10609–10617, 2020.

[135] Shuai Qin, Ning Xu, Hui Huang, Kaiqian Jie, Hongzhan Liu, Jianping Guo, Hongyun Meng, Faqiang Wang, Xiangbo Yang, and Zhongchao Wei. Near-infrared thermally modulated varifocal metalens based on the phase change material sb 2 s 3. *Optics Express*, 29(5):7925–7934, 2021.

[136] Sanaz Zarei and Amin Khavasi. Inverse design of on-chip thermally tunable varifocal metalens based on silicon metalines. *IEEE Access*, 9:73453–73466, 2021.

[137] Yanqun Wang, Li Chen, Shiwei Tang, Peipeng Xu, Fei Ding, Zhuoran Fang, and Arka Majumdar. Helicity-dependent continuous varifocal metalens based on bilayer dielectric metasurfaces. *Optics Express*, 29(24):39461–39472, 2021.

[138] Kentaro Iwami, Chikara Ogawa, Tomoyasu Nagase, and Satoshi Ikezawa. Demonstration of focal length tuning by rotational varifocal moiré metalens in an ir-a wavelength. *Optics Express*, 28(24):35602–35614, 2020.

[139] Fatih Balli, Mansoor A Sultan, and J Todd Hastings. Rotationally tunable varifocal 3d metalens. *Optics Letters*, 46(15):3548–3551, 2021.

[140] Melissa Bosch, Maxim R Shcherbakov, Kanghee Won, Hong-Seok Lee, Young Kim, and Gennady Shvets. Electrically actuated varifocal lens based on liquid-crystal-embedded dielectric metasurfaces. *Nano Letters*, 21(9):3849–3856, 2021.

[141] Yikun Chen, Shiliang Pu, Chongzhi Wang, and Fei Yi. Voltage tunable mid-wave infrared reflective varifocal metalens via an optomechanic cavity. *Optics Letters*, 46(8):1930–1933, 2021.

[142] Shane Colburn and Arka Majumdar. Simultaneous achromatic and varifocal imaging with quartic metasurfaces in the visible. *ACS Photonics*, 7(1):120–127, 2019.

[143] Chikara Ogawa, Sotaro Nakamura, Takumi Aso, Satoshi Ikezawa, and Kentaro Iwami. Rotational varifocal moiré metalens made of single-crystal silicon meta-atoms for visible wavelengths. *Nanophotonics*, 2022.

[144] Anna Archetti, Ren-Jie Lin, Ted V Tsoulos, Fatemeh Kiani, Nathanael Restori, and Giulia Tagliabue. Thermally reconfigurable varifocal silicon metalens. In *Current Developments in Lens Design and Optical Engineering XXII*, volume 11814, page 1181407. International Society for Optics and Photonics, 2021.

[145] Guoxing Zheng, Weibiao Wu, Zile Li, Shuang Zhang, Muhammad Qasim Mehmood, Song Li, et al. Dual field-of-view step-zoom metalens. *Optics Letters*, 42(7):1261–1264, 2017.

[146] Rao Fu, Zile Li, Guoxing Zheng, Ming Chen, Yan Yang, Jin Tao, Lin Wu, and Qiling Deng. Reconfigurable step-zoom metalens without optical and mechanical compensations. *Optics express*, 27(9):12221–12230, 2019.

[147] Francesco Aieta, Patrice Genevet, Mikhail A Kats, Nanfang Yu, Romain Blanchard, Zeno Gaburro, and Federico Capasso. Aberration-free ultrathin flat lenses and axicons at telecom wavelengths based on plasmonic metasurfaces. *Nano letters*, 12(9):4932–4936, 2012.

[148] Guangzhu Zhou, Shi-Wei Qu, Baojie Chen, Yuansong Zeng, and Chi Hou Chan. Metasurface-based fourier lens fed by compact plasmonic optical antennas for wide-angle beam steering. *Optics Express*, 30(12):21918–21930, 2022.

[149] Ning Zhang, Qingzhi Li, Jun Chen, Feng Tang, Jingjun Wu, Xin Ye, and Liming Yang. Design of an all-dielectric long-wave infrared wide-angle metalens. *Chinese Physics B*, 31(7):074212, 2022.

[150] Emmanuel Lassalle, Tobias WW Mass, Damien Eschimese, Anton V Baranikov, Egor Khaidarov, Shiqiang Li, Ramon Paniagua-Dominguez, and Arseniy I Kuznetsov. Imaging properties of large field-of-view quadratic metalenses and their applications to fingerprint detection. *Acs Photonics*, 8(5):1457–1468, 2021.

[151] Hoyeong Kwon, Dimitrios Sounas, Andrea Cordaro, Albert Polman, and Andrea Alù. Nonlocal metasurfaces for optical signal processing. *Physical review letters*, 121(17):173004, 2018.

[152] Jakob Søndergaard Jensen and Ole Sigmund. Topology optimization for nano-photonics. *Laser & Photonics Reviews*, 5(2):308–321, 2011.

[153] Rasmus E Christiansen and Ole Sigmund. Inverse design in photonics by topology optimization: tutorial. *JOSA B*, 38(2):496–509, 2021.

[154] Mahmoud MR Elsawy, Stéphane Lanteri, Régis Duvigneau, Jonathan A Fan, and Patrice Genevet. Numerical optimization methods for metasurfaces. *Laser & Photonics Reviews*, 14(10):1900445, 2020.

[155] Weibai Li, Fei Meng, Yafeng Chen, Yang fan Li, and Xiaodong Huang. Topology optimization of photonic and phononic crystals and metamaterials: a review. *Advanced Theory and Simulations*, 2(7):1900017, 2019.

[156] Sean Molesky, Zin Lin, Alexander Y Piggott, Weiliang Jin, Jelena Vucković, and Alejandro W Rodriguez. Inverse design in nanophotonics. *Nature Photonics*, 12(11):659–670, 2018.

[157] Evan W Wang, David Sell, Thaibao Phan, and Jonathan A Fan. Robust design of topology-optimized metasurfaces. *Optical Materials Express*, 9(2):469–482, 2019.

[158] Thaibao Phan, David Sell, Evan W Wang, Sage Doshay, Kofi Edee, Jianji Yang, and Jonathan A Fan. High-efficiency, large-area, topology-optimized metasurfaces. *Light: Science & Applications*, 8(1):48, 2019.

[159] Mingfeng Xu, Mingbo Pu, Di Sang, Yuhan Zheng, Xiong Li, Xiaoliang Ma, Yinghui Guo, Renyan Zhang, and Xiangang Luo. Topology-optimized catenary-like metasurface for wide-angle and high-efficiency deflection: from a discrete to continuous geometric phase. *Optics Express*, 29(7):10181–10191, 2021.

[160] Zin Lin and Steven G Johnson. Overlapping domains for topology optimization of large-area metasurfaces. *Optics express*, 27(22):32445–32453, 2019.

[161] Zin Lin, Victor Liu, Raphaël Pestourie, and Steven G Johnson. Topology optimization of freeform large-area metasurfaces. *Optics express*, 27(11):15765–15775, 2019.

[162] Peter Ingo Borel, Anders Harpøth, Lars Hagedorn Frandsen, Martin Kristensen, Peixiong Shi, Jakob Søndergaard Jensen, and Ole Sigmund. Topology optimization and fabrication of photonic crystal structures. *Optics express*, 12(9): 1996–2001, 2004.

[163] Jakob S Jensen and Ole Sigmund. Topology optimization of photonic crystal structures: a high-bandwidth low-loss t-junction waveguide. *JOSA B*, 22(6): 1191–1198, 2005.

[164] Alec M Hammond, Ardavan Oskooi, Steven G Johnson, and Stephen E Ralph. Photonic topology optimization with semiconductor-foundry design-rule constraints. *Optics Express*, 29(15):23916–23938, 2021.

[165] Louise F Frellsen, Yunhong Ding, Ole Sigmund, and Lars H Frandsen. Topology optimized mode multiplexing in silicon-on-insulator photonic wire waveguides. *Optics express*, 24(15):16866–16873, 2016.

[166] Rasmus E Christiansen, Jérôme Michon, Mohammed Benzaouia, Ole Sigmund, and Steven G Johnson. Inverse design of nanoparticles for enhanced raman scattering. *Optics Express*, 28(4):4444–4462, 2020.

[167] Ying Pan, Rasmus E Christiansen, Jérôme Michon, Juejun Hu, and Steven G Johnson. Topology optimization of surface-enhanced raman scattering substrates. *Applied Physics Letters*, 119(6):061601, 2021.

[168] Hasan Yılmaz, Matthias Kühmayer, Chia Wei Hsu, Stefan Rotter, and Hui Cao. Customizing the angular memory effect for scattering media. *Physical Review X*, 11(3):031010, 2021.

[169] Shiyu Li and Chia Wei Hsu. Thickness bound for nonlocal wide-field-of-view metalenses. *Light: Science & Applications*, 11(1):338, 2022.

[170] Zin Lin, Charles Roques-Carmes, Rasmus E Christiansen, Marin Soljačić, and Steven G Johnson. Computational inverse design for ultra-compact single-piece metalenses free of chromatic and angular aberration. *Applied Physics Letters*, 118(4):041104, 2021.

[171] Sourangsu Banerji, Monjurul Meem, Apratim Majumder, Fernando Guevara Vasquez, Berardi Sensale-Rodriguez, and Rajesh Menon. Ultra-thin near infrared camera enabled by a flat multi-level diffractive lens. *Optics letters*, 44 (22):5450–5452, 2019.

[172] Chenglong Hao, Shecheng Gao, Qifeng Ruan, Yuanhua Feng, Ying Li, Joel KW Yang, Zhaohui Li, and Cheng-Wei Qiu. Single-layer aberration-compensated flat lens for robust wide-angle imaging. *Laser & Photonics Reviews*, 14(6):2000017, 2020.

[173] Young Min Song, Yizhu Xie, Viktor Malyarchuk, Jianliang Xiao, Inhwa Jung, Ki-Joong Choi, Zhuangjian Liu, Hyunsung Park, Chaofeng Lu, Rak-Hwan Kim, et al. Digital cameras with designs inspired by the arthropod eye. *Nature*, 497 (7447):95–99, 2013.

[174] Dongmin Keum, Kyung-Won Jang, Daniel S Jeon, Charles SH Hwang, Elke K Buschbeck, Min H Kim, and Ki-Hun Jeong. Xenos peckii vision inspires an ultrathin digital camera. *Light: Science & Applications*, 7(1):80, 2018.

[175] Kisoo Kim, Kyung-Won Jang, Jae-Kwan Ryu, and Ki-Hun Jeong. Biologically inspired ultrathin arrayed camera for high-contrast and high-resolution imaging. *Light: Science & Applications*, 9(1):28, 2020.

[176] Andreas Brückner, Robert Leitel, Alexander Oberdörster, Peter Dannberg, Frank Wippermann, and Andreas Bräuer. Multi-aperture optics for wafer-level cameras. *Journal of Micro/Nanolithography, MEMS and MOEMS*, 10 (4):043010–043010, 2011.

[177] Andrea Toulouse, Johannes Drozella, Pascal Motzfeld, Nils Fahrbach, Valese Aslani, Simon Thiele, Harald Giessen, and Alois M Herkommer. Ultra-compact 3d-printed wide-angle cameras realized by multi-aperture freeform optical design. *Optics Express*, 30(2):707–720, 2022.

[178] Ji Chen, Xin Ye, Shenglun Gao, Yuxin Chen, Yunwei Zhao, Chunyu Huang, Kai Qiu, Shining Zhu, and Tao Li. Planar wide-angle-imaging camera enabled by metalens array. *Optica*, 9(4):431–437, 2022.

[179] Daniela Radtke and Uwe D Zeitner. Laser-lithography on non-planar surfaces. *Optics express*, 15(3):1167–1174, 2007.

[180] Jiyoung Chang, Qin Zhou, and Alex Zettl. Facile electron-beam lithography technique for irregular and fragile substrates. *Applied Physics Letters*, 105(17): 173109, 2014.

[181] Daniel K Nikolov, Aaron Bauer, Fei Cheng, Hitoshi Kato, A Nick Vamivakas, and Jannick P Rolland. Metaform optics: bridging nanophotonics and freeform optics. *Science Advances*, 7(18):eabe5112, 2021.

[182] Seyedeh Mahsa Kamali, Amir Arbabi, Ehsan Arbabi, Yu Horie, and Andrei Faraon. Decoupling optical function and geometrical form using conformal flexible dielectric metasurfaces. *Nature communications*, 7(1):11618, 2016.

[183] Sarah Geiger, Jerome Michon, Siyi Liu, Jun Qin, Jimmy Ni, Juejun Hu, Tian Gu, and Nanshu Lu. Flexible and stretchable photonics: the next stretch of opportunities. *ACS Photonics*, 7(10):2618–2635, 2020.

[184] Juejun Hu, Lan Li, Hongtao Lin, Ping Zhang, Weidong Zhou, and Zhenqiang Ma. Flexible integrated photonics: where materials, mechanics and optics meet. *Optical Materials Express*, 3(9):1313–1331, 2013.

[185] James Burch, Dandan Wen, Xianzhong Chen, and Andrea Di Falco. Conformable holographic metasurfaces. *Scientific Reports*, 7(1):4520, 2017.

[186] Francesco Aieta, Patrice Genevet, Mikhail Kats, and Federico Capasso. Aberrations of flat lenses and aplanatic metasurfaces. *Optics express*, 21(25):31530–31539, 2013.

[187] Nandor Bokor and Nir Davidson. Aberration-free imaging with an aplanatic curved diffractive element. *Applied Optics*, 40(32):5825–5829, 2001.

[188] Max Born and Emil Wolf. *Principles of optics: electromagnetic theory of propagation, interference and diffraction of light*. Elsevier, 2013.

[189] Eric J Tremblay, Daniel L Marks, David J Brady, and Joseph E Ford. Design and scaling of monocentric multiscale imagers. *Applied Optics*, 51(20):4691–4702, 2012.

[190] Igor Stamenov, Ilya P Agurok, and Joseph E Ford. Optimization of two-glass monocentric lenses for compact panoramic imagers: general aberration analysis and specific designs. *Applied optics*, 51(31):7648–7661, 2012.

[191] Wei-Lun Liang and Guo-Dung J Su. Wide-angle and ultrathin camera module using a curved hexagonal microlens array and all spherical surfaces. *Applied optics*, 53(29):H121–H128, 2014.

[192] Thomas Zentgraf, Yongmin Liu, Maiken H Mikkelsen, Jason Valentine, and Xiang Zhang. Plasmonic luneburg and eaton lenses. *Nature nanotechnology*, 6 (3):151–155, 2011.

[193] John Hunt, Talmage Tyler, Sulochana Dhar, Yu-Ju Tsai, Patrick Bowen, Stéphane Larouche, Nan M Jokerst, and David R Smith. Planar, flattened luneburg lens at infrared wavelengths. *Optics express*, 20(2):1706–1713, 2012.

[194] Yuan-Yuan Zhao, Yong-Liang Zhang, Mei-Ling Zheng, Xian-Zi Dong, Xuan-Ming Duan, and Zhen-Sheng Zhao. Three-dimensional luneburg lens at optical frequencies. *Laser & Photonics Reviews*, 10(4):665–672, 2016.

[195] Seung-Bum Rim, Peter B Catrysse, Rostam Dinyari, Kevin Huang, and Peter Peumans. The optical advantages of curved focal plane arrays. *Optics Express*, 16(7):4965–4971, 2008.

[196] Peng Wang, Nabil Mohammad, and Rajesh Menon. Chromatic-aberration-corrected diffractive lenses for ultra-broadband focusing. *Scientific reports*, 6 (1):21545, 2016.

[197] Peng Wang, Jose A Dominguez-Caballero, Daniel J Friedman, and Rajesh Menon. A new class of multi-bandgap high-efficiency photovoltaics enabled by broadband diffractive optics. *Progress in Photovoltaics: Research and Applications*, 23(9):1073–1079, 2015.

[198] Ganghun Kim, José A Domínguez-Caballero, and Rajesh Menon. Design and analysis of multi-wavelength diffractive optics. *Optics express*, 20(3):2814–2823, 2012.

[199] Peng Wang and Rajesh Menon. Optical microlithography on oblique and multi-plane surfaces using diffractive phase masks. *Journal of Micro/Nanolithography, MEMS, and MOEMS*, 14(2):023507, 2015.

[200] Peng Wang and Rajesh Menon. Computational spectrometer based on a broadband diffractive optic. *Optics express*, 22(12):14575–14587, 2014.

[201] M Born and E Wolf. Principle of optics, 1991.

[202] Sensong An, Bowen Zheng, Mikhail Y Shalaginov, Hong Tang, Hang Li, Li Zhou, Jun Ding, Anuradha Murthy Agarwal, Clara Rivero-Baleine, Myungkoo Kang, et al. Deep learning modeling approach for metasurfaces with high degrees of freedom. *Optics Express*, 28(21):31932–31942, 2020.

[203] Li Zhang, Jun Ding, Hanyu Zheng, Sensong An, Hongtao Lin, Bowen Zheng, Qingyang Du, Gufan Yin, Jerome Michon, Yifei Zhang, et al. Ultra-thin high-efficiency mid-infrared transmissive huygens meta-optics. *Nature communications*, 9(1):1481, 2018.

[204] Sensong An, Clayton Fowler, Bowen Zheng, Mikhail Y Shalaginov, Hong Tang, Hang Li, Li Zhou, Jun Ding, Anuradha Murthy Agarwal, Clara Rivero-Baleine, et al. A deep learning approach for objective-driven all-dielectric metasurface design. *ACS Photonics*, 6(12):3196–3207, 2019.

[205] Shimon Aburmad. Panoramic thermal imaging: challenges and tradeoffs. In *Infrared Technology and Applications XL*, volume 9070, pages 115–123. SPIE, 2014.

[206] Qingbin Fan, Mingze Liu, Cheng Yang, Le Yu, Feng Yan, and Ting Xu. A high numerical aperture, polarization-insensitive metalens for long-wavelength infrared imaging. *Applied Physics Letters*, 113(20):201104, 2018.

[207] Luocheng Huang, Zachary Coppens, Kent Hallman, Zheyi Han, Karl F Böhringer, Neset Akozbek, Ashok Raman, and Arka Majumdar. Long wavelength infrared imaging under ambient thermal radiation via an all-silicon metalens. *Optical Materials Express*, 11(9):2907–2914, 2021.

[208] Junwei Li, Yilin Wang, Shengjie Liu, Ting Xu, Kai Wei, Yudong Zhang, and Hao Cui. Largest aperture metalens of high numerical aperture and polarization independence for long-wavelength infrared imaging. *Optics Express*, 30(16): 28882–28891, 2022.

[209] Mingming Hou, Yan Chen, and Fei Yi. Lightweight long-wave infrared camera via a single 5-centimeter-aperture metalens. In *CLEO: QELS_ Fundamental Science*, page FM4F.4. Optica Publishing Group, 2022.

[210] Dongzhi Shan, Nianxi Xu, Jinsong Gao, Naitao Song, Hai Liu, Yang Tang, Xiaoguo Feng, Yansong Wang, Yi Zhao, Xin Chen, et al. Design of the all-silicon long-wavelength infrared achromatic metalens based on deep silicon etching. *Optics Express*, 30(8):13616–13629, 2022.

[211] Esther M Conwell. Properties of silicon and germanium. *Proceedings of the IRE*, 40(11):1327–1337, 1952.

[212] Halil Can Nalbant, Fatih Balli, Tolga Yelboğa, Arda Eren, and Ahmet Sözak. Transmission optimized lwir metalens. *Applied Optics*, 61(33):9946–9950, 2022.

[213] Chenglong Zhao, Ziqi Liu, and Wei Huang. Wide field-of-view metalens array for the long-wavelength infrared. In *Conference on Infrared, Millimeter, Terahertz Waves and Applications (IMT2022)*, volume 12565, pages 746–749. SPIE, 2023.

[214] Fan Yang, Sensong An, Mikhail Y Shalaginov, Hualiang Zhang, Clara Rivero-Baleine, Juejun Hu, and Tian Gu. Design of broadband and wide-field-of-view metalenses. *Optics Letters*, 46(22):5735–5738, 2021.

[215] Federico Presutti and Francesco Monticone. Focusing on bandwidth: achromatic metalens limits. *Optica*, 7(6):624–631, 2020.

[216] Wei Ting Chen, Alexander Y Zhu, Vyshakh Sanjeev, Mohammadreza Khorasaninejad, Zhujun Shi, Eric Lee, and Federico Capasso. A broadband achromatic metalens for focusing and imaging in the visible. *Nature nanotechnology*, 13(3): 220–226, 2018.

[217] Sajan Shrestha, Adam C Overvig, Ming Lu, Aaron Stein, and Nanfang Yu. Broadband achromatic dielectric metalenses. *Light: Science & Applications*, 7 (1):85, 2018.

[218] Mohammadreza Khorasaninejad, Zhujun Shi, Alexander Y Zhu, Wei-Ting Chen, Vyshakh Sanjeev, Aun Zaidi, and Federico Capasso. Achromatic metalens over 60 nm bandwidth in the visible and metalens with reverse chromatic dispersion. *Nano letters*, 17(3):1819–1824, 2017.

[219] Ehsan Arbabi, Amir Arbabi, Seyedeh Mahsa Kamali, Yu Horie, and Andrei Faraon. Controlling the sign of chromatic dispersion in diffractive optics with dielectric metasurfaces. *Optica*, 4(6):625–632, 2017.

[220] Qingqing Cheng, Meilin Ma, Dong Yu, Zhixiong Shen, Jingya Xie, Juncheng Wang, Nianxi Xu, Hanming Guo, Wei Hu, Shuming Wang, Tao Li, and Songlin Zhuang. Broadband achromatic metalens in terahertz regime. *Science Bulletin*, 64(20):1525–1531, 2019.

[221] Shuming Wang, Pin Chieh Wu, Vin-Cent Su, Yi-Chieh Lai, Cheng Hung Chu, Jia-Wern Chen, Shen-Hung Lu, Ji Chen, Beibei Xu, Chieh-Hsiung Kuan, Tao Li, Shining Zhu, and Din Ping Tsai. Broadband achromatic optical metasurface devices. *Nature communications*, 8(1):187, 2017.

[222] Abdoulaye Ndao, Liyi Hsu, Jeongho Ha, Jun-Hee Park, Connie Chang-Hasnain, and Boubacar Kanté. Octave bandwidth photonic fishnet-achromatic-metalens. *Nature communications*, 11(1):3205, 2020.

[223] Zhaoyi Li, Peng Lin, Yao-Wei Huang, Joon-Suh Park, Wei Ting Chen, Zhujun Shi, Cheng-Wei Qiu, Ji-Xin Cheng, and Federico Capasso. Meta-optics achieves rgb-achromatic focusing for virtual reality. *Science Advances*, 7(5):eabe4458, 2021.

[224] Haejun Chung and Owen D Miller. High-na achromatic metalenses by inverse design. *Optics express*, 28(5):6945–6965, 2020.

[225] Rasmus E Christiansen, Zin Lin, Charles Roques-Carmes, Yannick Salamin, Steven E Kooi, John D Joannopoulos, Marin Soljačić, and Steven G Johnson. Fullwave maxwell inverse design of axisymmetric, tunable, and multi-scale multi-wavelength metalenses. *Optics Express*, 28(23):33854–33868, 2020.

[226] Zin Lin, Charles Roques-Carmes, Raphaël Pestourie, Marin Soljačić, Arka Majumdar, and Steven G Johnson. End-to-end nanophotonic inverse design for imaging and polarimetry. *Nanophotonics*, 10(ahead-of-print):1177–1187, 2020.

[227] Ethan Tseng, Shane Colburn, James Whitehead, Luocheng Huang, Seung-Hwan Baek, Arka Majumdar, and Felix Heide. Neural nano-optics for high-quality thin lens imaging. *arXiv preprint arXiv:2102.11579*, 2021.

[228] Peter R Wiecha and Otto L Muskens. Deep learning meets nanophotonics: a generalized accurate predictor for near fields and far fields of arbitrary 3d nanostructures. *Nano letters*, 20(1):329–338, 2019.

[229] Maksym V Zhelyeznyakov, Steve Brunton, and Arka Majumdar. Deep learning to accelerate scatterer-to-field mapping for inverse design of dielectric metasurfaces. *ACS Photonics*, 8(2):481–488, 2021.

[230] Sensong An, Bowen Zheng, Mikhail Y Shalaginov, Hong Tang, Hang Li, Li Zhou, Yunxi Dong, Mohammad Haerinia, Anuradha Murthy Agarwal, Clara Rivero-Baleine, et al. Deep convolutional neural networks to predict mutual coupling effects in metasurfaces. *arXiv preprint arXiv:2102.01761*, 2021.

[231] Jacob Engelberg and Uriel Levy. Achromatic flat lens performance limits. *Optica*, 8(6):834–845, 2021.

[232] Sourangsu Banerji, Monjurul Meem, Apratim Majumder, Fernando Guevara Vasquez, Berardi Sensale-Rodriguez, and Rajesh Menon. Imaging with flat optics: metalenses or diffractive lenses? *Optica*, 6(6):805–810, 2019.

[233] Jacob Engelberg and Uriel Levy. The advantages of metalenses over diffractive lenses. *Nature communications*, 11(1):1991, 2020.

[234] Sensong An, Bowen Zheng, Hong Tang, Mikhail Y Shalaginov, Li Zhou, Hang Li, Myungkoo Kang, Kathleen A Richardson, Tian Gu, Juejun Hu, Clayton Fowler, and Hualiang Zhang. Multifunctional metasurface design with a generative adversarial network. *Advanced Optical Materials*, 9(5):2001433, 2021.

[235] Mikhail Y Shalaginov, Sawyer D Campbell, Sensong An, Yifei Zhang, Carlos Ríos, Eric B Whiting, Yuhao Wu, Lei Kang, Bowen Zheng, Clayton Fowler, Hualiang Zhang, Douglas H Werner, Juejun Hu, and Tian Gu. Design for quality: reconfigurable flat optics based on active metasurfaces. *Nanophotonics*, 9(ahead-of-print):3505–3534, 2020.

[236] Sean Quirin and Rafael Piestun. Depth estimation and image recovery using broadband, incoherent illumination with engineered point spread functions. *Applied optics*, 52(1):A367–A376, 2013.

[237] Shane Colburn, Alan Zhan, and Arka Majumdar. Metasurface optics for full-color computational imaging. *Science advances*, 4(2):eaar2114, 2018.

[238] Shane Colburn and Arka Majumdar. Simultaneous varifocal and broadband achromatic computational imaging using quartic. *Science*, 345:298–302, 2014.

[239] Edward R Dowski and W Thomas Cathey. Extended depth of field through wave-front coding. *Applied optics*, 34(11):1859–1866, 1995.

[240] W Thomas Cathey and Edward R Dowski. New paradigm for imaging systems. *Applied optics*, 41(29):6080–6092, 2002.

[241] Alan Zhan, Shane Colburn, Christopher M Dodson, and Arka Majumdar. Metasurface freeform nanophotonics. *Scientific reports*, 7(1):1–9, 2017.

[242] Jian Wang. Metasurfaces enabling structured light manipulation: advances and perspectives. *Chinese Optics Letters*, 16(5):050006, 2018.

[243] Chao He, Yijie Shen, and Andrew Forbes. Towards higher-dimensional structured light. *Light: Science & Applications*, 11(1):205, 2022.

[244] Nanxi Li, Chong Pei Ho, Jin Xue, Leh Woon Lim, Guanyu Chen, Yuan Hsing Fu, and Lennon Yao Ting Lee. A progress review on solid-state lidar and nanophotonics-based lidar sensors. *Laser & Photonics Reviews*, 16(11):2100511, 2022.

[245] Junghyun Park, Byung Gil Jeong, Sun Il Kim, Duhyun Lee, Jungwoo Kim, Changgyun Shin, Chang Bum Lee, Tatsuhiro Otsuka, Jisoo Kyoung, Sangwook Kim, et al. All-solid-state spatial light modulator with independent phase and amplitude control for three-dimensional lidar applications. *Nature nanotechnology*, 16(1):69–76, 2021.

[246] Renato Juliano Martins, Emil Marinov, M Aziz Ben Youssef, Christina Kyrou, Mathilde Joubert, Constance Colmagro, Valentin Gâté, Colette Turbil, Pierre-Marie Coulon, Daniel Turover, et al. Metasurface-enhanced light detection and ranging technology. *Nature Communications*, 13(1):5724, 2022.

[247] Yinxiao Miao, Yongshun Zhao, Huiping Ma, Minwei Jiang, Jie Lin, and Peng Jin. Design of diffractive optical element projector for a pseudorandom dot array by an improved encoding method. *Applied Optics*, 58(34):G169–G176, 2019.

[248] Omri Barlev and Michael A Golub. Multifunctional binary diffractive optical elements for structured light projectors. *Optics Express*, 26(16):21092–21107, 2018.

[249] Ralf Vandenhouten, Andreas Hermerschmidt, and Richard Fiebelkorn. Design and quality metrics of point patterns for coded structured light illumination with diffractive optical elements in optical 3d sensors. In *Digital Optical Technologies 2017*, volume 10335, pages 264–276. SPIE, 2017.

[250] P Twardowski, B Serio, V Raulot, and M Guilhem. Three-dimensional shape measurement based on light patterns projection using diffractive optical elements. In *Micro-Optics 2010*, volume 7716, pages 704–711. SPIE, 2010.

[251] Nanfang Yu, Patrice Genevet, Mikhail A Kats, Francesco Aieta, Jean-Philippe Tetienne, Federico Capasso, and Zeno Gaburro. Light propagation with phase discontinuities: generalized laws of reflection and refraction. *science*, 334(6054): 333–337, 2011.

[252] Alexander V Kildishev, Alexandra Boltasseva, and Vladimir M Shalaev. Planar photonics with metasurfaces. *Science*, 339(6125):1232009, 2013.

[253] Stanislav B Glybovski, Sergei A Tretyakov, Pavel A Belov, Yuri S Kivshar, and Constantin R Simovski. Metasurfaces: From microwaves to visible. *Physics reports*, 634:1–72, 2016.

[254] Philippe Lalanne and Pierre Chavel. Metalenses at visible wavelengths: past, present, perspectives. *Laser & Photonics Reviews*, 11(3):1600295, 2017.

[255] Federico Capasso. The future and promise of flat optics: a personal perspective. *Nanophotonics*, 7(6):953–957, 2018.

[256] Seyedeh Mahsa Kamali, Ehsan Arbabi, Amir Arbabi, and Andrei Faraon. A review of dielectric optical metasurfaces for wavefront control. *Nanophotonics*, 7(6):1041–1068, 2018.

[257] Ming Lun Tseng, Hui-Hsin Hsiao, Cheng Hung Chu, Mu Ku Chen, Greg Sun, Ai-Qun Liu, and Din Ping Tsai. Metalenses: advances and applications. *Advanced Optical Materials*, 6(18):1800554, 2018.

[258] Tian Gu, Hyun Jung Kim, Clara Rivero-Baleine, and Juejun Hu. Reconfigurable metasurfaces towards commercial success. *Nature Photonics*, 17(1):48–58, 2023.

[259] Fan Yang, Hung-I Lin, Peng Chen, Juejun Hu, and Tian Gu. Monocular depth sensing using metalens. *Nanophotonics*, (0), 2023.

[260] Bohan Lyu, Meng-Ko Tsai, and Chih-Sheng Chang. Infrared structure light projector design for 3d sensing. In *Optical Design and Engineering VII*, volume 10690, pages 541–548. SPIE, 2018.

[261] Hao Zhou, Qingzhou Mao, Yufei Song, Anlei Wu, and Xueqing Hu. Analysis of internal angle error of uav lidar based on rotating mirror scanning. *Remote Sensing*, 14(20):5260, 2022.

[262] Hui Zuo and Siyuan He. Extra large aperture fpcb mirror based scanning lidar. *IEEE/ASME Transactions on Mechatronics*, 27(1):93–102, 2021.

[263] Cristiano Niclass, Kota Ito, Mineki Soga, Hiroyuki Matsubara, Isao Aoyagi, Satoru Kato, and Manabu Kagami. Design and characterization of a 256x64-pixel single-photon imager in cmos for a mems-based laser scanning time-of-flight sensor. *Optics Express*, 20(11):11863–11881, 2012.

[264] Dingkang Wang, Connor Watkins, and Huikai Xie. Mems mirrors for lidar: A review. *Micromachines*, 11(5):456, 2020.

[265] Ulrich Hofmann, Frank Senger, Frerk Soerensen, Vanessa Stenchly, Bjoern Jensen, and Joachim Janes. Biaxial resonant 7mm-mems mirror for automotive lidar application. In *2012 International Conference on optical MEMS and nanophotonics*, pages 150–151. IEEE, 2012.

[266] Yuzuru Takashima, Brandon Hellman, Joshua Rodriguez, Guanghao Chen, Braden Smith, Adley Gin, Alonzo Espinoza, Paul Winkler, Cameron Perl, Chuan Luo, et al. Mems-based imaging lidar. In *Optics and Photonics for Energy and the Environment*, pages ET4A–1. Optica Publishing Group, 2018.

[267] Sung-Woo Lee, Haesoo Jeong, Seoung-Ki Lee, Young-Kweon Kim, and Jae-Hyoung Park. Lidar system using indirect time of flight method and mems scanner for distance measurement. In *2016 International Conference on Optical MEMS and Nanophotonics (OMN)*, pages 1–2. IEEE, 2016.

[268] Abhishek Kasturi, Veljko Milanović, Daniel Lovell, Frank Hu, Derek Ho, Yu Su, and Lj Ristic. Comparison of mems mirror lidar architectures. In *MOEMS and Miniaturized Systems XIX*, volume 11293, pages 63–79. SPIE, 2020.

[269] Norbert Druml, Ievgeniia Maksymova, Thomas Thurner, Diederik van Lierop, Marcus Hennecke, and Andreas Foroutan. 1d mems micro-scanning lidar. In *Conference on Sensor Device Technologies and Applications (SENSORDEVICES)*, volume 9, 2018.

[270] Thinal Raj, Fazida Hanim Hashim, Aqilah Baseri Huddin, Mohd Faisal Ibrahim, and Aini Hussain. A survey on lidar scanning mechanisms. *Electronics*, 9(5): 741, 2020.

[271] Josué J López, Scott A Skirlo, Dave Kharas, Jamison Sloan, Jeffrey Herd, Paul Juodawlkis, Marin Soljačić, and Cheryl Sorace-Agaskar. Planar-lens enabled beam steering for chip-scale lidar. In *2018 Conference on Lasers and Electro-Optics (CLEO)*, pages 1–2. IEEE, 2018.

[272] Daisuke Inoue, Tadashi Ichikawa, Akari Kawasaki, and Tatsuya Yamashita. Demonstration of a new optical scanner using silicon photonics integrated circuit. *Optics express*, 27(3):2499–2508, 2019.

[273] Samuel Kim, Jamison Sloan, Josué J López, Dave Kharas, Jeffrey Herd, Suraj Bramhavar, Paul Juodawlkis, George Barbastathis, Steven Johnson, Cheryl Sorace-Agaskar, et al. Luneburg lens for wide-angle chip-scale optical beam steering. In *CLEO: Science and Innovations*, pages SF3N–7. Optica Publishing Group, 2019.

[274] Yang Liu, Xavier Le Roux, Eric Cassan, Delphine Marris-Morini, Laurent Vivien, Carlos Alonso-Ramos, and Daniele Melati. Silicon-based broadband

metalens for wide-angle optical beam steering. In *2021 IEEE 17th International Conference on Group IV Photonics (GFP)*, pages 1–2. IEEE, 2021.

[275] Steven J Spector. Review of lens-assisted beam steering methods. *Journal of Optical Microsystems*, 2(1):011003–011003, 2022.

[276] Woo-Bin Lee, Chul-Soon Im, Changyi Zhou, Bishal Bhandari, Duk-Yong Choi, and Sang-Shin Lee. Metasurface doublet-integrated bidirectional grating antenna enabling enhanced wavelength-tuned beam steering. *Photonics Research*, 10(1):248–255, 2022.

[277] Yi-Yang Xie, Pei-Nan Ni, Qiu-Hua Wang, Qiang Kan, Gauthier Briere, Pei-Pei Chen, Zhuang-Zhuang Zhao, Alexandre Delga, Hao-Ran Ren, Hong-Da Chen, et al. Metasurface-integrated vertical cavity surface-emitting lasers for programmable directional lasing emissions. *Nature nanotechnology*, 15(2):125–130, 2020.

[278] Wei Ting Chen, Alexander Y Zhu, and Federico Capasso. Flat optics with dispersion-engineered metasurfaces. *Nature Reviews Materials*, 5(8):604–620, 2020.

[279] Xiong Li, Mingbo Pu, Xiaoliang Ma, Yinghui Guo, Ping Gao, and Xiangang Luo. Dispersion engineering in metamaterials and metasurfaces. *Journal of Physics D: Applied Physics*, 51(5):054002, 2018.

[280] Augusto Martins, Kezheng Li, Guilherme S Arruda, Donato Conteduca, Haowen Liang, Juntao Li, Ben-Hur V Borges, Thomas F Krauss, and Emiliano R Martins. Correction of aberrations via polarization in single layer metalenses. *Advanced Optical Materials*, 10(9):2102555, 2022.

[281] Zicheng Shen, Feng Zhao, Chunqi Jin, and Yuanmu Yang. Single-shot passive 3d and polarization vision using a monocular metasurface camera. In *2022 Conference on Lasers and Electro-Optics (CLEO)*, pages 1–2. IEEE, 2022.

[282] Yoav Y Schechner, Rafael Piestun, and Joseph Shamir. Wave propagation with rotating intensity distributions. *Physical Review E*, 54(1):R50, 1996.

[283] SN Khonina, VV Kotlyar, VA Soifer, M Honkanen, J Lautanen, and J Turunen. Generation of rotating gauss—laguerre modes with binary-phase diffractive optics. *Journal of Modern Optics*, 46(2):227–238, 1999.

[284] Sri Rama Prasanna Pavani and Rafael Piestun. High-efficiency rotating point spread functions. *Optics express*, 16(5):3484–3489, 2008.

[285] Rafael Piestun and Joseph Shamir. Control of wave-front propagation with diffractive elements. *Optics letters*, 19(11):771–773, 1994.

[286] Peng Wang and Rajesh Menon. Optimization of periodic nanostructures for enhanced light-trapping in ultra-thin photovoltaics. *Optics express*, 21(5):6274–6285, 2013.

[287] Gaurav Arya, William F Li, Charles Roques-Carmes, Marin Soljačić, Steven G Johnson, and Zin Lin. End-to-end optimization of metasurfaces for imaging with compressed sensing. *arXiv preprint arXiv:2201.12348*, 2022.

[288] Zin Lin, Raphaël Pestourie, Charles Roques-Carmes, Zhaoyi Li, Federico Capasso, Marin Soljačić, and Steven G Johnson. End-to-end metasurface inverse design for single-shot multi-channel imaging. *Optics Express*, 30(16):28358–28370, 2022.

[289] Ho-Seok Ee and Ritesh Agarwal. Tunable metasurface and flat optical zoom lens on a stretchable substrate. *Nano letters*, 16(4):2818–2823, 2016.

[290] Stephanie C Malek, Ho-Seok Ee, and Ritesh Agarwal. Strain multiplexed metasurface holograms on a stretchable substrate. *Nano letters*, 17(6):3641–3645, 2017.

[291] Fei Cheng, Liangyu Qiu, Daniel Nikolov, Aaron Bauer, Jannick P Rolland, and A Nick Vamivakas. Mechanically tunable focusing metamirror in the visible. *Optics express*, 27(11):15194–15204, 2019.

[292] Aaron L Holsteen, Ahmet Fatih Cihan, and Mark L Brongersma. Temporal color mixing and dynamic beam shaping with silicon metasurfaces. *Science*, 365(6450):257–260, 2019.

[293] Kunal Shastri and Francesco Monticone. Bandwidth bounds for wide-field-of-view dispersion-engineered achromatic metalenses. *arXiv preprint arXiv:2204.09154*, 2022.

[294] Carlos Ríos, Matthias Stegmaier, Peiman Hosseini, Di Wang, Torsten Scherer, C David Wright, Harish Bhaskaran, and Wolfram HP Pernice. Integrated all-photonic non-volatile multi-level memory. *Nature photonics*, 9(11):725–732, 2015.

[295] Carlos Rios, Peiman Hosseini, C David Wright, Harish Bhaskaran, and Wolfram HP Pernice. On-chip photonic memory elements employing phase-change materials. *Advanced Materials*, 26(9):1372–1377, 2014.

[296] Zengguang Cheng, Carlos Ríos, Nathan Youngblood, C David Wright, Wolfram HP Pernice, and Harish Bhaskaran. Device-level photonic memories and logic applications using phase-change materials. *Advanced Materials*, 30(32): 1802435, 2018.

[297] Peiman Hosseini, C David Wright, and Harish Bhaskaran. An optoelectronic framework enabled by low-dimensional phase-change films. *Nature*, 511(7508): 206–211, 2014.

[298] Carlos Ríos, Peiman Hosseini, Robert A Taylor, and Harish Bhaskaran. Color depth modulation and resolution in phase-change material nanodisplays. *Advanced Materials*, 28(23):4720–4726, 2016.

[299] Hong-Kai Ji, Hao Tong, Hang Qian, Ya-Juan Hui, Nian Liu, Peng Yan, and Xiang-Shui Miao. Non-binary colour modulation for display device based on phase change materials. *Scientific Reports*, 6(1):1–7, 2016.

[300] Zhigang Ni, Shenghong Mou, Tong Zhou, and Zhiyuan Cheng. Broader color gamut of color-modulating optical coating display based on indium tin oxide and phase change materials. *Applied optics*, 57(13):3385–3389, 2018.

[301] Jianbo Wang, Qian Li, Shuaipeng Tao, Zhoubo Xia, Yuankai Li, Yan Liu, Zhiqing Gu, and Chaoquan Hu. Improving the reflectance and color contrasts of phase-change materials by vacancy reduction for optical-storage and display applications. *Optics Letters*, 45(1):244–247, 2020.

[302] Mohsen Jafari, L Jay Guo, and Mina Rais-Zadeh. A reconfigurable color reflector by selective phase change of gete in a multilayer structure. *Advanced Optical Materials*, 7(5):1801214, 2019.

[303] Matthias Stegmaier, Carlos Ríos, Harish Bhaskaran, C David Wright, and Wolfram HP Pernice. Nonvolatile all-optical 1× 2 switch for chipscale photonic networks. *Advanced Optical Materials*, 5(1):1600346, 2017.

[304] Hanyu Zhang, Linjie Zhou, Jian Xu, Ningning Wang, Hao Hu, Liangjun Lu, BMA Rahman, and Jianping Chen. Nonvolatile waveguide transmission tuning with electrically-driven ultra-small gst phase-change material. *Science Bulletin*, 64(11):782–789, 2019.

[305] Takumi Moriyama, Daiki Tanaka, Paridhi Jain, Hitoshi Kawashima, Masashi Kuwahara, Xiaomin Wang, and Hiroyuki Tsuda. Ultra-compact, self-holding asymmetric mach-zehnder interferometer switch using ge2sb2te5 phase-change material. *IEICE Electronics Express*, 11(15):20140538–20140538, 2014.

[306] Daiki Tanaka, Yuya Shoji, Masashi Kuwahara, Xiaomin Wang, Kenji Kintaka, Hitoshi Kawashima, Tatsuya Toyosaki, Yuichiro Ikuma, and Hiroyuki Tsuda. Ultra-small, self-holding, optical gate switch using ge 2 sb 2 te 5 with a multimode si waveguide. *Optics express*, 20(9):10283–10294, 2012.

[307] Jiajiu Zheng, Amey Khanolkar, Peipeng Xu, Shane Colburn, Sanchit Deshmukh, Jason Myers, Jesse Frantz, Eric Pop, Joshua Hendrickson, Jonathan Doylend, et al. Gst-on-silicon hybrid nanophotonic integrated circuits: a non-volatile quasi-continuously reprogrammable platform. *Optical Materials Express*, 8(6):1551–1561, 2018.

[308] Changping Zhang, Ming Zhang, Yiwei Xie, Yaocheng Shi, Rajesh Kumar, Roberto R Panepucci, and Daoxin Dai. Wavelength-selective 2× 2 optical

switch based on a ge 2 sb 2 te 5-assisted microring. *Photonics Research*, 8 (7):1171–1176, 2020.

[309] Johannes Feldmann, Nathan Youngblood, Maxim Karpov, Helge Gehring, Xuan Li, Maik Stappers, Manuel Le Gallo, Xin Fu, Anton Lukashchuk, Arslan Sajid Raja, et al. Parallel convolutional processing using an integrated photonic tensor core. *Nature*, 589(7840):52–58, 2021.

[310] J Feldmann, M Stegmaier, N Gruhler, C Ríos, H Bhaskaran, CD Wright, and WHP Pernice. Calculating with light using a chip-scale all-optical abacus. *Nature communications*, 8(1):1256, 2017.

[311] Indranil Chakraborty, Gobinda Saha, and Kaushik Roy. Photonic in-memory computing primitive for spiking neural networks using phase-change materials. *Physical Review Applied*, 11(1):014063, 2019.

[312] Johannes Feldmann, Nathan Youngblood, C David Wright, Harish Bhaskaran, and Wolfram HP Pernice. All-optical spiking neurosynaptic networks with self-learning capabilities. *Nature*, 569(7755):208–214, 2019.

[313] Jianmin Wang, Lei Wang, and Jun Liu. Overview of phase-change materials based photonic devices. *IEEE Access*, 8:121211–121245, 2020.

[314] Fei Ding, Yuanqing Yang, and Sergey I Bozhevolnyi. Dynamic metasurfaces using phase-change chalcogenides. *Advanced Optical Materials*, 7(14):1801709, 2019.

[315] Libang Mao, Yang Li, Guixin Li, Shuang Zhang, and Tun Cao. Reversible switching of electromagnetically induced transparency in phase change metasurfaces. *Advanced Photonics*, 2(5):056004–056004, 2020.

[316] Xinghui Yin, Tobias Steinle, Lingling Huang, Thomas Taubner, Matthias Wuttig, Thomas Zentgraf, and Harald Giessen. Beam switching and bifocal zoom lensing using active plasmonic metasurfaces. *Light: Science & Applications*, 6 (7):e17016–e17016, 2017.

[317] Weiling Dong, Yimei Qiu, Xilin Zhou, Agnieszka Banas, Krzysztof Banas, Mark BH Breese, Tun Cao, and Robert E Simpson. Tunable mid-infrared phase-change metasurface. *Advanced Optical Materials*, 6(14):1701346, 2018.

[318] Andreas Tittl, Ann-Katrin U Michel, Martin Schäferling, Xinghui Yin, Behrad Gholipour, Long Cui, Matthias Wuttig, Thomas Taubner, Frank Neubrech, and Harald Giessen. A switchable mid-infrared plasmonic perfect absorber with multispectral thermal imaging capability. *Advanced Materials*, 27(31): 4597–4603, 2015.

[319] Yifei Zhang, Jeffrey B Chou, Junying Li, Huashan Li, Qingyang Du, Anupama Yadav, Si Zhou, Mikhail Y Shalaginov, Zhuoran Fang, Huikai Zhong, et al.

Broadband transparent optical phase change materials for high-performance nonvolatile photonics. *Nature communications*, 10(1):4279, 2019.

[320] Qihang Zhang, Yifei Zhang, Junying Li, Richard Soref, Tian Gu, and Juejun Hu. Broadband nonvolatile photonic switching based on optical phase change materials: beyond the classical figure-of-merit. *Optics letters*, 43(1):94–97, 2018.

[321] Yifei Zhang, Junying Li, Jeffrey Chou, Zhuoran Fang, Anupama Yadav, Hongtao Lin, Qingyang Du, Jerome Michon, Zhaohong Han, Yizhong Huang, et al. Broadband transparent optical phase change materials. In *CLEO: Science and Innovations*, pages JTh5C–4. Optica Publishing Group, 2017.

[322] Francesco De Leonardis, Richard Soref, Vittorio MN Passaro, Yifei Zhang, and Juejun Hu. Broadband electro-optical crossbar switches using low-loss ge 2 sb 2 se 4 te 1 phase change material. *Journal of Lightwave Technology*, 37(13): 3183–3191, 2019.

[323] Weifeng Jiang and BM Azizur Rahman. Compact and nonvolatile mode-selective switch with nano-heater. *IEEE Journal of Selected Topics in Quantum Electronics*, 26(5):1–10, 2019.

[324] Haoxiang Chen, Hao Jia, Tao Wang, Yonghui Tian, and Jianhong Yang. Broadband nonvolatile tunable mode-order converter based on silicon and optical phase change materials hybrid meta-structure. *Journal of Lightwave Technology*, 38(7):1874–1879, 2020.

[325] Junchao Song, Souvik Ghosh, Hanyu Zhang, Linjie Zhou, and BMA Rahman. Design, optimization, and performance evaluation of gsst clad low-loss nonvolatile switches. *Applied Optics*, 58(31):8687–8694, 2019.

[326] V Liberman, Y Zhang, M Shalaginov, C Rios, P Robinson, C Roberts, K Tibbetts, M Kang, K Richardson, J Hu, et al. Reconfigurable infrared flat optics with novel phase change materials. In *Novel Optical Materials and Applications*, pages NoW3B–2. Optica Publishing Group, 2019.

[327] Roseanna G Lawandi, Remona Heenkenda, and Andrew M Sarangan. Silicon photodetectors integrated with gsst phase change material for switchable color filter pixels. In *Laser Science*, pages JW3A–124. Optica Publishing Group, 2019.

[328] Joaquin Faneca, Liam Trimby, Ioannis Zeimpekis, Matthew Delaney, Daniel W Hewak, Frederic Y Gardes, C David Wright, and Anna Baldycheva. On-chip sub-wavelength bragg grating design based on novel low loss phase-change materials. *Optics Express*, 28(11):16394–16406, 2020.

[329] Weifeng Jiang. Reconfigurable mode (de) multiplexer via 3-d triple-waveguide directional coupler with optical phase change material. *Journal of Lightwave Technology*, 37(3):1000–1007, 2018.

[330] Weifeng Jiang. Nonvolatile and ultra-low-loss reconfigurable mode (de) multiplexer/switch using triple-waveguide coupler with ge2sb2se4te1 phase change material. *Scientific Reports*, 8(1):15946, 2018.

[331] Yihui Wei, Ming Zhang, and Daoxin Dai. Multichannel mode-selective silicon photonic add/drop multiplexer with phase change material. *JOSA B*, 37(11): 3341–3350, 2020.

[332] Pavel Trofimov, Andrey Bogdanov, and Ivan Sinev. Hybrid silicon-phase change nanoantenna for surface plasmon polariton routing. In *AIP Conference Proceedings*, volume 2300, page 020129. AIP Publishing LLC, 2020.

[333] I Sinev, C Ruiz de Galarreta, P Trofimov, A Alexeev, J Bertolotti, and CD Wright. Hybrid silicon/phase-change metasurfaces and nanoantennas for active nanophotonics. In *Journal of Physics: Conference Series*, volume 1461, page 012164. IOP Publishing, 2020.

[334] Juejun Hu, Vladimir Tarasov, Anu Agarwal, Lionel Kimerling, Nathan Carlie, Laeticia Petit, and Kathleen Richardson. Fabrication and testing of planar chalcogenide waveguide integrated microfluidic sensor. *Optics Express*, 15(5): 2307–2314, 2007.

[335] Hammad Nazeer, Harish Bhaskaran, Leon A Woldering, and Leon Abelmann. Young's modulus and residual stress of gesbte phase-change thin films. *Thin solid films*, 592:69–75, 2015.

[336] TP Leervad Pedersen, J Kalb, WK Njoroge, D Wamwangi, M Wuttig, and F Spaepen. Mechanical stresses upon crystallization in phase change materials. *Applied physics letters*, 79(22):3597–3599, 2001.

[337] Hongtao Lin, Lan Li, Fei Deng, Chaoying Ni, Sylvain Danto, J David Musgraves, Kathleen Richardson, and Juejun Hu. Demonstration of mid-infrared waveguide photonic crystal cavities. *Optics letters*, 38(15):2779–2782, 2013.

[338] Yifei Zhang, Clayton Fowler, Junhao Liang, Bilal Azhar, Mikhail Y Shalaginov, Skylar Deckoff-Jones, Sensong An, Jeffrey B Chou, Christopher M Roberts, Vladimir Liberman, et al. Electrically reconfigurable non-volatile metasurface using low-loss optical phase-change material. *Nature Nanotechnology*, 16(6): 661–666, 2021.

[339] Carlos Ríos, Yifei Zhang, Mikhail Y Shalaginov, Skylar Deckoff-Jones, Haozhe Wang, Sensong An, Hualiang Zhang, Myungkoo Kang, Kathleen A Richardson, Christopher Roberts, et al. Multi-level electro-thermal switching of optical phase-change materials using graphene. *Advanced Photonics Research*, 2(1): 2000034, 2021.

[340] Borislav Vasić, Goran Isić, Romeo Beccherelli, and Dimitrios C Zografopoulos. Tunable beam steering at terahertz frequencies using reconfigurable metasurfaces coupled with liquid crystals. *IEEE Journal of Selected Topics in Quantum Electronics*, 26(5):1–9, 2019.

[341] Shi-Qiang Li, Xuewu Xu, Rasna Maruthiyodan Veetil, Vytautas Valuckas, Ramón Paniagua-Domínguez, and Arseniy I Kuznetsov. Phase-only transmissive spatial light modulator based on tunable dielectric metasurface. *Science*, 364(6445):1087–1090, 2019.

[342] Oleksandr Buchnev, Nina Podoliak, Malgosia Kaczmarek, Nikolay I Zheludev, and Vassili A Fedotov. Electrically controlled nanostructured metasurface loaded with liquid crystal: toward multifunctional photonic switch. *Advanced Optical Materials*, 3(5):674–679, 2015.

[343] Rafał Kowerdziej, Jerzy Wróbel, and Przemysław Kula. Ultrafast electrical switching of nanostructured metadevice with dual-frequency liquid crystal. *Scientific Reports*, 9(1):20367, 2019.

[344] Rashid G Bikbaev, Dmitrii N Maksimov, Kuo-Ping Chen, and Ivan V Timofeev. Double-resolved beam steering by metagrating-based tamm plasmon polariton. *Materials*, 15(17):6014, 2022.

[345] Yao-Wei Huang, Ho Wai Howard Lee, Ruzan Sokhoyan, Ragip A Pala, Krishnan Thyagarajan, Seunghoon Han, Din Ping Tsai, and Harry A Atwater. Gate-tunable conducting oxide metasurfaces. *Nano letters*, 16(9):5319–5325, 2016.

[346] Sun Il Kim, Junghyun Park, Byung Gil Jeong, Duhyun Lee, Ki-Yeon Yang, Yong-Young Park, Kyoungho Ha, and Hyuck Choo. Two-dimensional beam steering with tunable metasurface in infrared regime. *Nanophotonics*, 11(11): 2719–2726, 2022.

[347] Ghazaleh Kafaie Shirmanesh, Ruzan Sokhoyan, Pin Chieh Wu, and Harry A Atwater. Electro-optically tunable multifunctional metasurfaces. *ACS nano*, 14 (6):6912–6920, 2020.

[348] Jongwon Lee, Seungyong Jung, Pai-Yen Chen, Feng Lu, Frederic Demmerle, Gerhard Boehm, Markus-Christian Amann, Andrea Alù, and Mikhail A Belkin. Ultrafast electrically tunable polaritonic metasurfaces. *Advanced Optical Materials*, 2(11):1057–1063, 2014.

[349] Yonghwi Kim, Pin Chieh Wu, Ruzan Sokhoyan, Kelly Mauser, Rebecca Glaudell, Ghazaleh Kafaie Shirmanesh, and Harry A Atwater. Phase modulation with electrically tunable vanadium dioxide phase-change metasurfaces. *Nano letters*, 19(6):3961–3968, 2019.

[350] Prasad P Iyer, Mihir Pendharkar, Chris J Palmstrøm, and Jon A Schuller. Iii–v heterojunction platform for electrically reconfigurable dielectric metasurfaces. *ACS Photonics*, 6(6):1345–1350, 2019.

[351] Prachi Thureja, Ghazaleh Kafaie Shirmanesh, Katherine T Fountaine, Ruzan Sokhoyan, Meir Grajower, and Harry A Atwater. Array-level inverse design of beam steering active metasurfaces. *ACS nano*, 14(11):15042–15055, 2020.

[352] Prachi Thureja, Ruzan Sokhoyan, Claudio U Hail, Jared Sisler, Morgan Foley, Meir Y Grajower, and Harry A Atwater. Toward a universal metasurface for optical imaging, communication, and computation. *Nanophotonics*, 11(17): 3745–3768, 2022.

[353] Steven A Vitale, Paul Miller, Paul Robinson, Christopher Roberts, Vlad Liberman, Qingyang Du, Yifei Zhang, Cosmin-Constantin Popescu, Mikhail Y Shalaginov, Myungkoo Kang, et al. Phase transformation and switching behavior of magnetron plasma sputtered ge2sb2se4te. *Advanced Photonics Research*, 3 (10):2200202, 2022.

[354] MG Moharam, Eric B Grann, Drew A Pommet, and TK Gaylord. Formulation for stable and efficient implementation of the rigorous coupled-wave analysis of binary gratings. *JOSA a*, 12(5):1068–1076, 1995.

[355] Philippe Lalanne and G Michael Morris. Highly improved convergence of the coupled-wave method for tm polarization. *JOSA A*, 13(4):779–784, 1996.

[356] Philippe Lalanne and Marie Paule Jurek. Computation of the near-field pattern with the coupled-wave method for transverse magnetic polarization. *Journal of modern optics*, 45(7):1357–1374, 1998.

[357] Amir Arbabi, Ehsan Arbabi, Mahdad Mansouree, Seunghoon Han, Seyedeh Mahsa Kamali, Yu Horie, and Andrei Faraon. Increasing efficiency of high numerical aperture metasurfaces using the grating averaging technique. *Scientific reports*, 10(1):1–10, 2020.